INTER FARM INTERACTIONS AND HUB HEIGHT OPTIMIZATION FOR
ONSHORE WIND FARMS

A THESIS SUBMITTED TO
THE GRADUATE SCHOOL OF NATURAL AND APPLIED SCIENCES
OF
MIDDLE EAST TECHNICAL UNIVERSITY

BY

GÖKAY KÜTÜKCÜ

IN PARTIAL FULFILLMENT OF THE REQUIREMENTS
FOR
THE DEGREE OF MASTER OF SCIENCE
IN
AEROSPACE ENGINEERING

SEPTEMBER 2022

Approval of the thesis:

INTER FARM INTERACTIONS AND HUB HEIGHT OPTIMIZATION FOR ONSHORE WIND FARMS

submitted by **GÖKAY KÜTÜKCÜ** in partial fulfillment of the requirements for the degree of **Master of Science** in **Aerospace Engineering, Middle East Technical University** by,

Prof. Dr. Halil Kalıpçılar
Dean, Graduate School of **Natural and Applied Sciences**   _____

Prof. Dr. Serkan Özgen
Head of the Department, **Aerospace Engineering Department**   _____

Prof. Dr. Oğuz Uzol
Supervisor, **Aerospace Engineering, METU**   _____

Examining Committee Members:

Asst. Prof. Dr. A. Türker Kutay
Aerospace Engineering Department, METU   _____

Prof. Dr. Oğuz Uzol
Aerospace Engineering Department, METU   _____

Assoc. Prof. Dr. Munir Elfarra
Aerospace Engineering Department, Ankara Yıldırım Beyazıt University   _____

Assoc. Prof. Dr. Elif Oğuz
Civil Engineering Department, METU   _____

Asst. Prof. Dr. Mustafa Perçin
Aerospace Engineering Department, METU   _____

Date: 02.09.2022

I hereby declare that all information in this document has been obtained and presented in accordance with academic rules and ethical conduct. I also declare that, as required by these rules and conduct, I have fully cited and referenced all material and results that are not original to this work.

Name Last name : Gökay Kütükcü

Signature :

ABSTRACT

INTER FARM INTERACTIONS AND HUB HEIGHT OPTIMIZATION FOR ONSHORE WIND FARMS

Kütükcü, Gökay
Master of Science, Aerospace Engineering
Supervisor : Prof. Dr. Oğuz Uzol

September 2022, 114 pages

This thesis presents the results of an investigation that focuses on finding the optimum tower height distributions for two interacting on-shore wind farms that are located on a complex terrain. Four different optimization scenarios are studied based on two different definitions of objective functions, which take into account both the power production capacity and the relevant cost variations due to changing hub heights. The study is based on simulations using the FLORIS framework, which is modified such that existing significant variations in hub height levels due to elevation differences for the studied on-shore wind farms, hence partial wake interactions that are occurring as a consequence, are more realistically represented. Results show that when both wind farms are included in the optimization process and if the cost parameters are not included in the objective function definition, the optimization process tends towards increasing the hub height levels of the turbines in the upstream wind farm to benefit from increased wind speeds at higher hub heights. However, when the cost parameters are included, the optimization both tries to reduce wake interaction effects while increasing hub heights of the turbines that are not interacting with the downstream wind farm. When only the downstream wind farm is included in the optimization process but if the cost cost parameters are not included, the

optimized results show that hub heights of all of the most influential turbines get increased. However when the cost parameters are included, the optimized results show that the hub heights of the partially interacting turbines get decreased and those that are operating under stronger cluster-wake effects get increased.

ÖZ

KARASAL RÜZGAR SANTRALLERİ İÇİN SANTRALLER ARASI ETKİLEŞİM VE KULE YÜKSEKLİĞİ OPTİMİZASYONU

Kütükcü, Gökay
Yüksek Lisans, Havacılık ve Uzay Mühendisliği
Tez Yöneticisi: Prof. Dr. Oğuz Uzol

Eylül 2022, 114 sayfa

Bu tez, karmaşık arazi yapısında yer alan, etkileşim halindeki iki karasal rüzgar çiftliği için optimum kule yüksekliği dağılımlarını bulmaya odaklanan bir araştırmanın sonuçlarını sunmaktadır. Hem enerji üretim kapasitesini hem de değişen kule yüksekliklerinden kaynaklanan ilgili maliyet değişikliklerini hesaba katan iki farklı amaç fonksiyonu tanımına dayalı olarak dört farklı optimizasyon senaryosu incelenmiştir. Çalışma, incelenen karasal rüzgar santralleri için rakım farkları nedeniyle kule yükseklik seviyelerinde oluşan önemli yükseklik farklarının, dolayısıyla bu farklar sonucunda meydana gelen kısmi iz bölgesi etkileşimlerinin görece gerçekçi şekilde modellenmesiyle FLORIS'te gerçekleştirilen simülasyonlara dayanmaktadır. Bununla birlikte maliyet etkilerini içeren maliyet parametreleri amaç fonkiyonuna eklendiğinde, iz bölgesi etkileşimi olmayan türbinlerin kule yüksekliklerinin arttığı görüldü. Eğer sadece iz bölgesi etkisinde olan rüzgar santrali, santral üretimini artırmaya yönelik amaç fonksiyonu ile optimize edilirse, amaç fonksiyonunu en fazla etkileyen bütün türbinlerin kule yüksekliğinin arttığı görüldü. Bununla birlikte, amaç fonksiyonuna kule yüksekliğini içeren maliyet bazlı etki eklenirse, iz bölgesi etkileşimi fazla olan türbinlerin kule

yükseklİği artarken, daha az iz bölgesi etkileşimi olan türbinlerin kule yüksekliği ise azalmaktadır.

Anahtar Kelimeler: Kule Yüksekliği Optimizasyonu, FLORIS, Rüzgar Türbini İz Bölgesi, Rüzgar Santrali Etkileşimi, Kümelenmiş İz Bölgesi

To my precious Banu Çiçek...

ACKNOWLEDGMENTS

I would like to express my deepest gratitude to my supervisor, Prof. Dr. Oğuz Uzol, for allowing me to work with him and benefit from his invaluable insights and experiences, as well as his guidance in completing my study. Without his enthusiasm and energy, I would not be capable of completing my study.

I would like to express gratitude Dr. Mustafa Çelebi in EMRA for his patience and broad understanding in completing the thesis.

I would like to thank the Havza wind farm and Kayadüzü wind farm operating companies for the information they have provided regarding the SCADA data.

Finally, but most importantly, I would like to express my endless gratitude to my family and wife for their never-ending prayers, love, and support throughout my life, and of course to my dear daughter Bilge.

TABLE OF CONTENTS

LIST OF TABLES

LIST OF FIGURES

FIGURES

xvii

LIST OF ABBREVIATIONS

ABL	Atmospheric Boundary Layer
AEP	Annual Energy Production
CCD	Central Composite Design
CFD	Computational Fluid Dynamic
DoE	Design of Experiment
EU	European Uninon
FLORIS	Flow Redirection and Induction in Steady-State
GCH	Gauss Curl Hybrid
GW	Giga Watt
GWEC	Global Wind Energy Council
HH	Hub Height
kWh	Kilowatts Hours
LES	Large Eddy Simulation
LCoE	Levelized Cost of Energy
MW	Megawatts
NREL	National Renewable Energy Laboratory
OEC	Overall Evaluation Crtiteria
RANS	Reynolds Averaged Navier-Stokes
RE	Relative Elevation
RSE	Response Surface Equation
SCADA	Supervisory Control And Data Acquisition
SOWFA	Simulator for Wind Farm Applications
TE	Terrain Elevation
TI	Turbulence Intensity
USA	United State of America
WPP	Wind Energy Power Plant
WRF	Weather Research and Forecasting

LIST OF SYMBOLS

a	Axial induction factor
a'	Tangential induction factor
α	Shear coefficient
A	Rotor area
B	Number of blade of a wind turbine
c	Scale parameter in weibull distribution
c_T	Thrust coefficient
Γ	Circulation strength
γ	Yaw angle
γ_{eff}	Effective yaw angle
γ_{turb}	Exact amount of yaw offset
δ	Wake deflection
D	Rotor diameter
D_w	Wake Expansion
I	Turbulence Intensity
I_+	Added turbulence
I_{wake}	Streamwise turbulence intensity
K	First kind of elliptic integral
k	Shape parameter in weibull distribution
k^*	Wake growth rate
λ	Tip speed ratio
l_m	Mixing length
N	Number of turbines in a wind farm
Π	Secon kind of elliptic integral
ρ	Air density
T	Thrust force
σ	Standart deviation

U	Wind velocity
ν_T	Turbulent viscosity
u_{HH}	Hub height velocity
u_{Ref}	Reference velocity
$\bar{u}_{Scada}$	Average velocity on SCADA data
$\bar{u}_{Floris}$	Average velocity on FLORIS simulations
$\emptyset$	Amount of the veer
V_{rot}	Rotational velocity
V_{rel}	Relative velocity
z_{RE}	Relative elevation of the turbine
z_{Ref-V}	Reference virtual hub height
z_{Ref}	Reference specified wind height
z_{TE}	Terrain elevation of the turbine
z_V	Virtual hub height

CHAPTER 1

INTRODUCTION

The increasing global energy need and the environmental problems felt on a global scale increase the demand for renewable energy sources in electricity energy generation. In order to meet more electricity generation from renewable energy sources, countries have developed various support mechanisms that will facilitate the establishment of facilities based on renewable energy sources on a national scale. Through these mechanisms, the installed power based on renewable energy sources, especially hydraulic, wind and solar energy, has increased day by day. While the total installed capacity based on wind energy sources was 24 Giga Watts (GW) in 2001 in the world, it became 837 GW by the end of 2021 [1]. Regarding the electricity generation, the share of wind energy in global electricity generation reached 5.4% from 0.9% in last 20 years [2].

Renewable energy-based power plants must be constructed where the source is, which means that they must always follow the renewable source. Wind energy power plants have been installed on the sea for the past 30 years (Figure 1.2), with the recognition that the wind conditions are also appropriate for the development of these power plants on the sea.

Because wind energy power plants can be installed both on land and in the sea, onshore wind farms and offshore wind farms are the two types of wind farms, depending on where they are constructed. Onshore wind farms have grown across Europe, the USA, and China, whereas offshore wind farms are mostly installed in Europe and China.
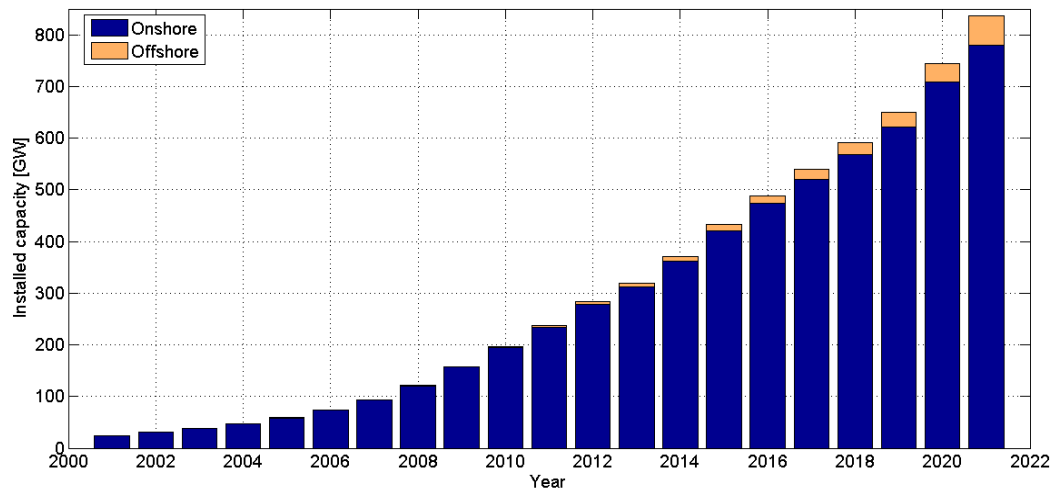
Figure 1.1. Historical development of wind energy installed capacity. Data was
taken from [1]

The installed capacity of onshore wind energy power plants (WPPs) is 837 GW as
of the end of 2021. When examining statistics from the previous 20 years, it is clear
that total onshore WPP capacity has steadily expanded. Between 2001 and 2010,
there was a significant increase in capacity (an annual average increase of 26%), and
the installed capacity doubled every 3 years during this 10-year period. The rate of
increase has slowed slightly after 2010, yet installed power has continued to rise.
The capacity of 100 GW in 2008, 400 GW in 2015, and 600 GW in 2019 has all been
exceeded. Despite the detrimental effects of the global supply chain, the highest
yearly installed capacity rise was in 2021, when 93.6 GW of capacity was added.

China is be the leading country in terms of onshore installed capacity by the end of
2021, with 310.6 GW installed capacity. The United States comes in second with
134.4 GW of installed capacity, Germany is third with 56.8 GW, and India is fourth
with 40.1 GW [1]. Turkey is one of the leading countries in the world in onshore
WPP projects with 10.8 GW installed capacity [3].

In terms of offshore WPP projects, the world's first offshore WPP project was
commissioned on the coast of Vindeby, Denmark, in 1991. The power plant, which

2

consists of 11 turbines with a total installed power of 450 kW, has a total installed capacity of 4.95 MW and was erected at a distance of 2 km from the coast at a water depth of 4 meters [4]. Despite the fact that the first offshore WPP project was installed in 1991, there was little progress in offshore WPP installation during the 1990s. The rise in installation began in the early 2000s. Offshore renewable energy projects were established in the southern North Sea, the Irish Sea, and the Baltic Sea during these years. These places are deemed acceptable project zones for offshore power plants since the average wind speed across these seas is more than 8 m/s and the average sea depth is less than 50 meters [4].

The installed capacity of offshore wind power plants reached 57.2 GW by the end of 2021 (Figure 1.2). In terms of offshore wind installed capacity, there has been a significant increase in the last ten years, particularly in Europe and China. The United Kingdom, Germany, Belgium, Denmark, and the Netherlands are key European countries for offshore WPP projects in Europe. Aside from European countries, China has made tremendous progress in project development, ranking first in installed capacity by the end of 2021. In terms of average sea depth and wind speed, cost of China is excellent zones for offshore wind projects as in North and Baltic Sea [1].
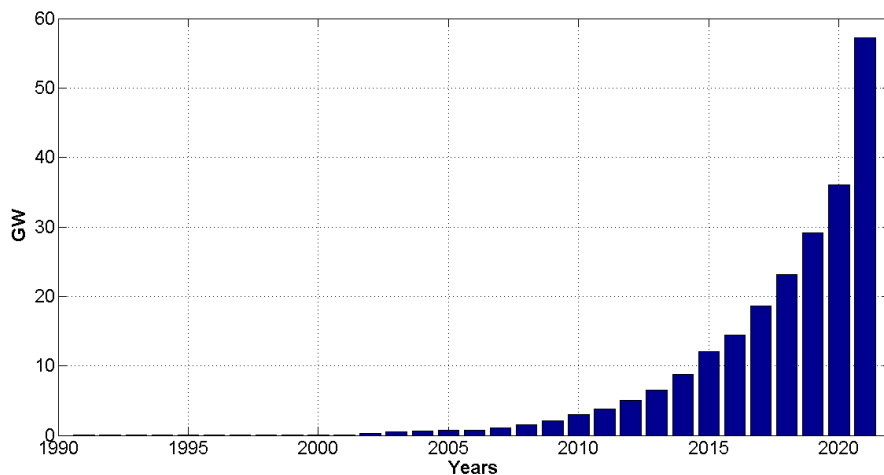
Figure 1.2. Historical development of offshore wind installed capacity. Data was taken from [1]

In addition to the current condition, 466 GW onshore and 90 GW offshore wind projects are expected to be built between 2022 and 2026 [1].

There are two main reasons behind the increase in the demand for renewable energy sources, especially wind energy. The first of these is the efforts of countries to ensure energy supply security. The second reason is related to environmental concerns. The EU, Japan, South Korea, Canada, and South Africa all pledged to achieve net zero carbon emissions by 2050 in 2020, making it a watershed year for carbon neutrality. Aside from these countries, China has declared a net zero aim for 2060, while the United States has established a target for 2050, in collaboration with the Biden administration [1].

One of the most essential aspects of wind energy power plants is that their installed capacity and number are constantly expanding and will continue to do so in the upcoming period. Because both onshore and offshore projects require installation in wind-efficient zones, the greater the number of these power plants, the more likely they are to be installed close together. The fact that wind power plants are being installed in close proximity to one another increases the interaction between them. Offshore wind farms may have a higher probability of being developed near together than onshore wind farms. Because location of the offshore wind farms are determined by policymakers based on certain site selection criteria, they are typically erected in relatively close proximity to one another. Interaction due to the fact that wind farms operate at relatively close distances to each other is explained by the cluster wake phenomenon, which can be described as the total effect of the wake of each wind turbine in the wind farm as a whole. Annual Energy Production of wind farms is directly affected by the cluster wake interaction. The interaction generated by the cluster wake has a direct impact on the Annual Energy Production of wind farms because it reduces the average wind speed in the cluster wake-affected wind farm. As the distance between wind farms decreases, the cluster wake effect analysis of wind farms becomes an essential subject that must be investigated.

This thesis firstly presents an investigation that focuses on inter-farm cluster-wake interactions for two onshore wind farms that are in close proximity of each other. The simulations are performed using the different wake models in FLORIS framework. Because of the relatively complex terrain of the wind farms, there are significant elevation differences between turbines and this is modeled through an easy to implement terrain elevation representation that takes into account relative hub height and rotor overlap positions. The second part of the thesis focuses on finding the optimum tower height distributions for two interacting on-shore wind farms. The optimization study is performed for hub height distributions based on a systematic procedure that includes introducing definitions of Overall Evaluation Criteria (OEC) parameters for objective setting, generation of Design of Experiments (DoE) tables and related data through FLORIS simulations to properly cover the design space, Pareto analysis of generated data to find the most influential parameters, generation of response surfaces to represent these variations and Monte-Carlo based simulations to determine optimum hub height distributions.

1.1   Wind Turbine Wakes

One of the important concentrations in the design of a wind farm is to get the maximum AEP as a whole. Since, AEP would have a substantial impact on the project's annual revenue and, as a result, its profitability. In a wind farm layout, the wind resource of the site, land availability, and environmental conditions, the location of each turbine can directly affect the AEP value. The ultimate goal from here is to optimize the AEP while staying within the limits and decreasing the cost as possible on the initial investment and running expenditures. Macro-siting is a term used to describe this process [5].

The next stage is to choose the best possible placement for each individual wind turbine. There are various instances of commercial software that may be used to construct a wind farm right now. The main trend has been to deploy wind turbines in locations with the largest wind potential repeatedly. It is determined by the

distance between wind turbines in the direction of the prevailing wind to avoid an excessive wake impact [5]. Wake losses are increased by closer spacing between turbines, whereas higher distances result in inefficient land usage. Wake losses are known to have a major impact on wind farms, accounting for up to 20% of overall output [6]. Along with turbine design, the optimization challenge of turbine positioning for maximum energy output remains one of the difficult tasks for the engineers. The wind turbine wake is the main issue in this optimization task.

The momentum deficiency and higher level of turbulence caused by turbines in a wind farm may cause a loss in power extraction and unstable loads on other turbines, making wind turbine wakes a significant research issue. These research issues were primarily aimed at understanding the physical mechanism of the event [7].

In the wake, there are two primary physical phenomena of interest: the momentum deficit, which reduces downstream turbine power output, and the increased degree of turbulence, which creates unsteady loading on downstream turbines [7].

Near and far wake are two zones within the wake that are researched for wake-induced power losses and blade loadings [7].
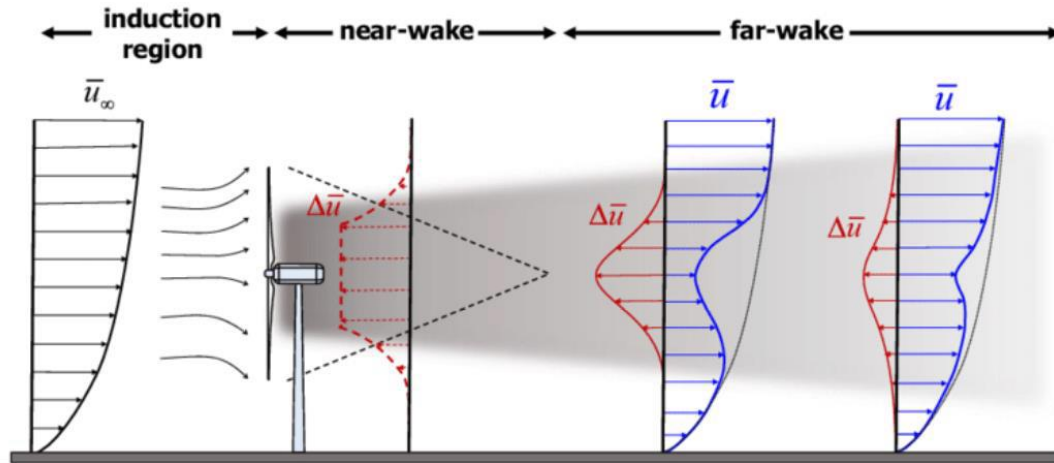
Figure 1.3. Wind turbine wake regions [8]

A significant distinction may be made in the wake behind a wind turbine into to the near and far wake regions (Figure 1.4). The near wake is defined as the region vicinity of the rotor where the rotor's attributes can be distinguished, which is around one rotor diameter downstream. The helical vortex formations characterize the near wake [9]. The rotor geometry has a significant impact on the flow in this region [7].

The far wake is the area beyond the near wake where the rotor features have less of an impact. The actual rotor is given less significance in this model, with the focus being on wake models, wake interference, turbulence models, and topographic impacts [9]. The atmospheric turbulence has also an impact on this region. The velocity deficit approaches a Gaussian profile (which will be discussed in detail in the following chapter) in the far wake [7].

The goal of near-wake research is to maximize power extraction, whereas far-wake research is mainly concerned with the mutual interaction of wind turbines in rows. Then, the velocity of the incident flow over the affected turbines is relatively lower, while the turbulence intesity is higher. This causes a decline in power extraction and an increase in unsteady loads [9].

1.2 Wind Turbine Wake Models

Wind turbine wakes and wake models have been a research area since the late 1970s, when there was a resurgence of interest in wind energy [9]. First, studies were carried out to understand the physical mechanism of the wake region, and then many literature surveys were made on the modeling of this mechanism. In the last 40 years, many independent academic studies on wake models have been conducted. Crespo et al. provide a thorough review of the literature on wake models. They suggested two different approaches to wake models. The first concept was that the turbines act as distributed roughness elements. The second methodology to wake modeling is to describe a single wake, followed by a calculation of its interaction with neighboring wakes [10].

The first model uses a logarithmic wind profile for the unperturbed wind, which incorporates ground roughness as a parameter. The roughness of the surface is increased by the presence of turbines. The wind velocity incident on each turbine may be computed using the modified wind profile, and the energy generation can then be calculated. Although not commonly used by researchers, these models could be useful for predicting the overall effects of wind farms having many turbines on wind properties [10].

The second approach to wake modeling is related to the description of a single wake, followed by a calculation of the wake's interaction with its neighbors. Individual models are the name for this type of model. Lisamann can be considered as the first adopter of this approach. Using basic fluid physics expressions and self-similar wake profiles obtained from Abramovich's experimental work, the author described a computer model for an arbitrary array of turbines [11].

In order to include the effects of all the upstream turbines in the total velocity deficit, four approaches are mainly used, which are the geometric sum, linear sum, energy balance, and quadratic sum [12].

Analytical (or kinematic) models and computational (or field) models are the two types of individual wake models available.

Because they make the least simplifications of the Navier-Stokes equations to completely characterize the turbine wake and turbulence, computational models are very time demanding and computationally expensive. With the use of Computational Fluid Dynamics (CFD), these models determine the flow magnitudes at every location in the flow field.

Taylor provided a two dimensional computational model for wakes in neutrally stratified atmospheric boundary layers based on solving flow equations and results are combined across turbine rows. After comparing his work with other kinematic models and experimental results, the linear superposition of these effects from

8

numerous rows of turbines, according to Taylor, could result in inappropriate power outputs for the backmost rows [13].

The other model that is three-dimensional, proposed by Liu et al. The model includes atmospheric stability effects. The diffusion due to turbulence originated in the wind turbine and the diffusion caused by the shear in the wake are neglected [14].

One of the important fields models was developed by Ainslie. He came up with a parabolic eddy viscosity model based on axisymmetric wake flow. In the analysis, pressure variations are not coupled, and only the continuity and axial momentum equations must be solved. An eddy viscosity closure scheme is used to explain the turbulent shear stresses. Prandtl's free shear layer model is implemented to represent Eddy viscosity. The eddy viscosity is a cross-sectional average value [15].

The other significant three-dimensional wake model is developed by Crespo et al. In this concept, the wind turbine is expected to be immersed in a non-uniform flow. The parameters of the non-uniform flow on the turbine are modeled by taking atmospheric stability and surface roughness into consideration. Turbulence modeling is based on the k- ε method. The conservation equations (mass, momentum, energy) is solved numerically by implementing finite difference method [16].

The other type of individual wake model is Analytical Wake Model. These models employ a modified version of the Navier-Stokes equation as well as semi-empirical functions. These functions are based on self-similar velocity deficit profiles discovered via experimental and theoretical research. The types of profiles of wakes in the near-wake and far-wake regions. In the far wake, the profiles are very similar. The Gaussian velocity shape is used to describe the near wake, which has a constant velocity in the center and a diminishing radius. To simplify the problem, the "top-hat shape profile" is sometimes used instead of the Gaussian profile [10].

In general, the velocity deficit reference value at each section has been calculated using the momentum conservation equation [10].

It has been proposed that the wake growth phenomenon is generated by the sum of ambient turbulence and turbulence created by shear in the wake [11]. Vermeulen added the effect of turbulence created by the turbine itself to this phenomenon [17]. and the wake's radius grows in linearly with downstream distance [18].

If the appropriate parameters are selected, these kinematic models will give results that are compatible with the experimental results [10].

Regarding the analytical wake models used in literature, Jensen wake model is one of the earliest example of the wake models which is first implemented in 1983 and assumes an uniform velocity profile inside the wake and is based on conservation of momentum [18]. This model was subsequently modified by Katic et al. [19] in 1986, taking into account wind turbine characteristics such as a changing thrust coefficient, and is now known as the PARK model. For wind farm modeling, Frandsen et al. [20] present a top-hat shape single wake model similar to Jensen wake model. Gebraad et al. [21], proposed a new top-hat shape based wake model to take into account the wake setting of the turbines. Nygaard et al. [22] developed a top-hat shape based wake deficit model to take into consideration atmospheric turbulence and the turbulence generated in wake itself. Gao et al. [23] used a Gaussian function to create a two dimensional wake model based on the Jensen model.

Martinez-Tossas [24] implemented the yawed condition of the turbines for the modelling of the wake and called this new model as curled wake. Later, Larsen [25], published a Gaussian-shape wake based wake model, which is based on Prandtl's turbulent boundary layer equation. Bastankah and Porté-Agel [26] developed the Gaussian wake model and the Gausssian shape is derived by applying conservation of the mass and momentum equations. Ishihara et al. [27] established a wake model that, for the first time, considers the effect of wake turbulence intensity on wake recovery.

In Chapter 2, the analytical wind turbine wake models are discussed in detail.

1.3   Inter Farm Interaction

Reduced turbine-to-turbine distances in a wind farm causes losses in energy production due to the presence of wind turbine wakes. Similar to these wake interactions occurring within a single wind farm (i.e. intra-farm interactions), wind farms that are in close proximity of each other also interact with each other as a whole (i.e. inter-farm interactions) due to the impact of wake clusters that are generated [28]. Ignoring the effects of such interactions may result in substantial variations in AEP assessments as well as in lifetime predictions of wind turbine structural components [28]. The percentage of energy lost caused by a cluster wake can range from 10% to 20% [29]. Studies conducted in offshore wind farms in recent years show that wakes originating from large offshore wind power plants can reach up to 50 kilometers in length and therefore impacting other neighboring wind farms [29], [30]. Recent studies based on field measurements show that cluster wakes are in fact longer than previously predicted [27], [30], [31], [32]. These studies mainly concentrate on a few key locations and reflect the varying inflow conditions for the various wind turbines in the test field.

Wake interactions in wind farms are generally studied either using analytical wake models [22], or using Computational Fluid Dynamics (CFD) simulations, which can be based on Reynolds Average Navier-Stokes (RANS) solvers (e.g. [32], [33]) or on Large Eddy Simulations (LES) (e.g. [34], [35]). Analytical wake models are generally preferred due to their low computational cost especially when AEP estimations, wind farm layout optimizations or wind farm controller developments are studied. These wake models are integrated in to a computational framework known as Flow Redirection and Induction in Steady-State (FLORIS), which is developed by NREL [36] and includes a variety of analytical wake models [37]. FLORIS was originally created to model and develop responses in power generation when wake control was applied for two or even more turbine layouts [38]. It was calibrated against large eddy simulations consisting of pairs of turbines interacting along their wake [39], using another NREL developed tool known as Simulator for

Wind Farm Applications (SOWFA). FLORIS was used in various previous studies from farm layout optimization for AEP maximization to wake steering based wind farm control [24], [40], [41], [42], [43], and mostly for offshore wind farms.

Regarding inter-farm interactions, the impact of cluster wakes generated in a wind farm on another nearby wind farm is investigated using various tools in previous studies and mostly for offshore wind farms. Comparisons of simulations obtained through various numerical, mesoscale or analytical wake models were performed with data available through the Supervisory Control And Data Acquisition (SCADA) system of the wind farms. Pettas et al. [31] investigated inter-farm interactions using data from Alpha Ventus wind farm located in the North Sea, which contains a fully equipped measurement platform. In their study they investigated how measured parameters such as turbulence intensity, wind speed distributions and wind shear have changed over time, from when the park was the only one operating one in the area to when other farms were established and started operating in close proximity. After 5 different offshore wind farms were installed around Alpha Ventus, varying between 1.4 km and 9 km, the shape parameter of the fitted Weibull distributions was reduced by 21%, indicating that wind speeds were reduced and the AEP of Alpha Ventus decreased from 19.6 GWh to 14 GWh. Hansen et al. [44] investigated wake interactions between two offshore wind farms using eight different flow models, including RANS, mesoscale, and engineering wake models. Simulation scenarios are selected based on wind speed level and results are compared against SCADA data. Presented results reveal that all models can anticipate the position and extent of the wake deficit zone within the downwind wind farm to a reasonable degree. Nygaard et al. [22] studied the effect of the cluster wake of an offshore wind farm on a downstream offshore wind farm using FLORIS framework and compared the results with SCADA data. Good agreement with data was observed especially when TurboPark wake model was used. Inter-farm interactions of on-shore wind farms are also studied previously, mostly using Weather Research and Forecasting (WRF) simulation tool [45]. Being a meso-scale model WRF can solve atmospheric boundary layers over complex terrain and can model local flow dynamics faster than

CFD solvers but still the simulations are generally performed for limited time periods. Lundquist et al. [28] reported approximately 5% loss in power generation in a downstream wind farm using WRF. In another study, the overall efficiency and power generation properties, as well as wake interaction effects between nearby onshore wind farms in China, were studied using WRF under real topographical and atmospheric characteristics. It was found that the entire field's wake recovers at 16.5 km downstream, and the average relative power loss ratio in the downstream region approached 5.8% [46]. In Pakistan, a similar study was conducted using the WRF model to estimate wind speed and power for a wind farm in the presence of wake interference from neighboring wind farms. In the downstream wind farm, incorporating the interaction of upstream wind farms resulted in a reduction of 15% and 26% in the normalized mean absolute error in power output values for the months of June and January, respectively [47].

1.4   Wind Farm Optimization

To reduce the wake effects of turbines and thereby improve the farm production, different optimization strategies are implemented in a wind farm. Wind farm layout optimization [48], and hub height optimization [49] are one of the widely implemented optimization strategies.

1.4.1   Wind Farm Layout Optimization

Wind farm layout optimization is a method for determining the best locations for wind turbines inside a wind farm in order to maximize or minimize any objectives (i.e. maximize AEP or minize the cost) while meeting specific limitations (i.e. border of wind farm, vicinity of wind turbines, noise constraints, initial investment limitaitons) [50]. Apart from the AEP and cost parameters, noise level is, in some cases, implemented as the most influential parameter for the wind farm layout optimization [51], [52].

Layout optimization can be accomplished using either a computationally expensive numerical technique [53], [54], [55], [56] or analytical wake models [48], [51], [57], [58], as a wake analysis method.

Regarding the CFD based techniques, Kuo et al. [56] provides a method for optimizing an onshore wind farm layouts in complex terrains. CFD and mixed-integer programming are combined in the suggested algorithm. The optimization technique uses mixed-integer programming and CFD simulations to iteratively enhance the accuracy of wake deficit estimations. The algorithm is implemented in a onshore wind farm located in a relatively complex terrain in Canada and suggested method produces outstanding layouts in complex terrains, according to the results. King et al. [53] proposed an adjoint method for computing the derivatives of the objective function with regard to the design variables. The optimization is then carried out using these analytical derivatives and a gradient-based minimization technique. For the flow model, 3 dimesional Reynolds-averaged Navier–Stokes (RANS) simulations are performed using a Python library. Using this algorithm 9% AEP improvement is achieved according to the initial condition. Antonini et al. [54] implement the 2 dimensional application of the adjoint method and get nearly 15% improvement in AEP with the graident based wind farm optimization method. In the another study of Antonini et al. [55], adjoint method is applied in a complex terrain onshore wind farm in Norway. AEP of the wind farm is caclculated using the CFD based wake models and optimization of the wind turbine layout in the wind farm is studied using CFD based optimization method in 5 days computational time. As a result of the study, 6.6% increment in AEP was provided.

Wind farm layout optimization studies are examined in some papers using the analytical wake models together with the different optimization algorithms. Yang et al. [58] optimized a wind farm with 49 turbines using three distinct analytical wake models (Jensen, Frandsen and Gaussian wake models). The optimization parameter was the cost of energy. The impelementation of a genetic algorithm to reduce the cost of electricity has been provided in the wind farm, with a cost reduction of 1.9%. Yang et al. [57] provided two different optimization parameters (maximize the

energy production and provide the wake effect uniformity) by using Jensen wake model in an onshore wind farm with 13 turbines. The layout optimization is performed using the heuristic method in the analysis. By using optimization parameters, both AEP was maximized and wake interaction was minimized. However, the proposed objective function fails to achieve both the aims of maximizing energy and limiting wake interaction. Quan and Kim [59] implemented the Jensen Wake model for the layout optimization and performed the Greedy algorithm for the optimization. The optimization parameter in their study was the maximization of the wind farm production. Bossi and Porte-Agel [60] performed the layout optimization using two different wake models (Jensen and Gaussian). A genetic algorithm was applied as the optimization method, and the Jensen Wake model presented a better result than Gaussian in terms of the power output. Stanley and Ning [61] optimized the winf farm layout employing the wake models in FLORIS framework, which included the hub height, rotor diameter, and tower shell thicknesses, with the aim of minimizing the levelized cost of energy. For the optimization of an onshore wind farm, Reddy [48] used the WindFLO framework. This framework was created for wind farm optimization and comprises six different analytical wake models as well as a turbine-based cost model that takes into account the turbine's terrain elevation and hence the wake-terrain interaction. Layout optimization is offered using the WindFLO optimization algorithm in order to maximize wind farm generation while lowering cost of energy. The effectiveness of various wake models was investigated, and the results were compared to experimental data.

Monte-Carlo simulation based optimization is one of the techniques used in optimization problems [62]. For example in Marmidis et al.'s paper [63], optimal wind turbine placement in a wind farm is performed using Monte- Carlo simulation technique. Using the Park model in wake calculations, they optimize the turbine placement in a wind farm and verify their results with previous studies using genetic algorithm for the same optimization.

1.4.2 Hub Height Optimization

Hub height optimization is one of the strategies investigated in literature to optimize the wind farms to reduce the cluster wake effects and thereby improve the AEP. Vasel-Be-Hagh and Archer [49] studied the the effect of tower height optimization on the wind farm production as the only optimization parameter of the wind turbine. They examined three different cases: the first case is two wind turbines aligned with the wind direction, the second case is comparison of two 20-turbine wind farms with 3 different hub heights and the third case is the optimization of the 48-turbine Lillgrund offshore wind farm under all 360 wind directions using a greedy search algorithm. Using the PARK model to calculate wake losses, it is found that AEP could be increased by 2% with the multiple hub height optimization method in Lillgrund offshore wind farm. Stanley et al. [64] suggested a hub height optimization based method with two different tower heights for a 81 turbine onshore wind farm using the gradient-based optimization technique. They used wake models in FLORIS framework and calculated AEP in FLORIS. They aimed to optimize wind farm using different hub heights, rotor diameter and tower wall thickness with the aim of reducing the cost of energy. 4.9% cost of energy reduction was accomplished using two alternative hub heights with a 70 meter rotor diameter and 0.08 shear coefficient in a nine-by-nine arrangement. In Wang et al. [65], a tower height optimization method together with the optimization of the number of turbines in real onshore wind farm in Turkey was applied. They constructed a cost of energy based optimization technique by varying the number of turbines in a wind farm from 30 to 39 and the hub heights from 40 to 80 meters. With 39 wind turbines and varying hub heights, the optimization approach produces approximately 9 kW more power per turbine than the baseline condition and lowers the cost of electricity by 0.08 million dollars per megawatt. MirHassani and Yarahmadi [66] studied the wind farm layout optimization in a 26-turbine wind farm and a 30 turbine wind farm with two different tower heights (50 m and 78 m tower heights) using the Jensen wake model in wake and power calculations. The hub height of turbines is optimization parameter in this

paper, and a 2.5% power incremeament in power output is provided. Chen et al. [67] implemented a wind farm layout optimization of a wind farm located in the comlex terrain usig the greedy algortihm. Their research reveals that, when compared to a wind farm with equal hub height wind turbines, a wind farm with multiple hub height wind turbines can significantly enhance total power output in complex terrain. In another research of the Chen et al. [68], wind farm layout optimization is provided using genetic algorithm for two different hub height (50 m and 78 m) wind turbines. Different hub height wind turbines can also enhance cost per power, according to the different cost models used in the optimization problem.

1.5   Objectives and Thesis Layout

The objective of the thesis is to invesitgate and find the optimum tower height distributions for two interacting onshore wind farms that are located on relatively complex terrain using the analytical wake models in FLORIS framework.

In Chapter 2, seven different analytical wake models in the FLORIS framework are examined in detail and compared with each other. In Chapter 3, the simulations are performed using FLORIS framework to investigate the interactions of onshore wind farms that are located in relatively more complex terrain. Because of the terrain, there are significant elevation differences between turbines and this is modeled through an easy to implement terrain elevation representation that takes into account relative hub height and rotor overlap positions while using realistic estimates (i.e. consistent with SCADA data) for hub height velocity levels despite potentially large differences in hub heights of the wind turbines. Simulations are performed with and without terrain elevation representation using four different wake models that are available in FLORIS (i.e. Jensen, Multizone, GCH and Gaussian) and the variations in velocity fields are compared. Comparisons of FLORIS predicted AEP levels with SCADA data for the year of 2021 are also calculated and compared. The main findings and results are discussed at the end of this section. In Chapter 4, focuses on finding the optimum tower height distributions for two interacting on-shore wind farms. The

optimization study is performed for hub height distributions based on a systematic procedure that includes introducing definitions of OEC parameters for objective setting, generation of DoE tables and related data through FLORIS simulations to properly cover the design space, Pareto analysis of generated data to find the most influential parameters, generation of response surfaces to represent these variations and Monte-Carlo based simulations to determine optimum hub height distributions. Finally in Chapter 5, concluding remarks and future works are presented.

CHAPTER 2

FLOW REDIRECTION AND INDUCTION IN STEADY STATE (FLORIS) FOR WIND FARM ANALYSIS

The National Renewable Energy Laboratory (NREL) and Delft University of Technology created the open-source FLORIS platform, which optimizes wind energy power plants. With this program, the interaction of turbines in a wind energy power plant can be modeled and real-time optimization can be made to increase the performance of wind energy power plant. The FLORIS is a computationally inexpensive, controls-oriented modeling tool for steady-state wake characteristics in wind farms. One of the control-oriented tools is wake steering and energy production of wind farms can be increased through wake steering. According to the results of optimizations, any estimation can be made on the impact of the performance on annual energy production [37].

An important paper on the use of FLORIS as a modeling and simulation tool has been published by Annoni et al. [69]. In this paper, wind turbine wake models used for wind farm controls and optimization were compared with the lidar measurement results. The lidar mounted on the nacelle of a selected 1,5 MW wind turbine scanned the five downstream distances. The lidar measurements are used to validate control-oriented tools. Among the implemented wake models, the Gaussian model is better able to match the lidar data under no misalinged conditions. The Jensen, Multizone, and Gaussian models exhibit strong agreement with lidar data under yaw misaligned settings.

There are three different models in the FLORIS framework: wake model, turbulence model and turbine model. When it comes to FLORIS' tools, there are three types: visualization, optimization, and analysis. The wake models in the FLORIS are

presented in detail on the next page. As a wake turbulence module; Crespo Hernandez turbulence model and Ishihara Qian turbulence models were introduced to FLORIS framework. The turbine module can contain all the essential data (i.e. cp-ct tables, rotor diameter, hub height, TSR etc.) about turbines in the both wind farms [70].

The FLORIS uses the following wake models [71]:

- Jensen model (wake model to estimate velocity deficit)

- Jimenez model (wake deflection model)

- Multi zone model (wake model to estimate velocity deficit)

- Gaussian models (used for both wake deflection and velocity deficit)

- Gauss-Curl-Hybrid (GCH) model (used for second-order wake steering effects)

- Curl model (used for both wake deflection and velocity deficit)

- TurboPark model (wake model to estimate velocity deficit)

A detailed examination and a literature review regarding these models are provided in the following sections.

2.1   Jensen Wake Model

Because of its easiness, effectiveness, and stability, the Jensen wake model is one of the most common among engineering applications. The theory of the model is based on Jensen [18] and Katic et al.'s [19] researches.

This model is computationally inexpensive because of its easy to applicability and is based on the assumptions that the flow is steady, the wake behind a wind turbine expands linearly, and the velocity deficit is only affected by the cross section. The initial diameter of the wake behind a turbine is regarded to be the same as the turbine

diameter. Because of this simplification, the wake velocity cannot be determined with great precision at all downwind sites; however, by changing the spread angle to fit data at distances more than four diameters, only the computation of the nearwake zone will have significant inaccuracies [19].

Instead of using the typical Gaussian distribution which will be discussed in following section, the velocity inside the wake is assumed to be constant, as the model's objective is to assess the energy content of the wind flow seen by downstream turbines rather than to properly represent the velocity field [19].

In this model, an actuator disk model in a constant uniform flow with uniform axial loading is used [69].
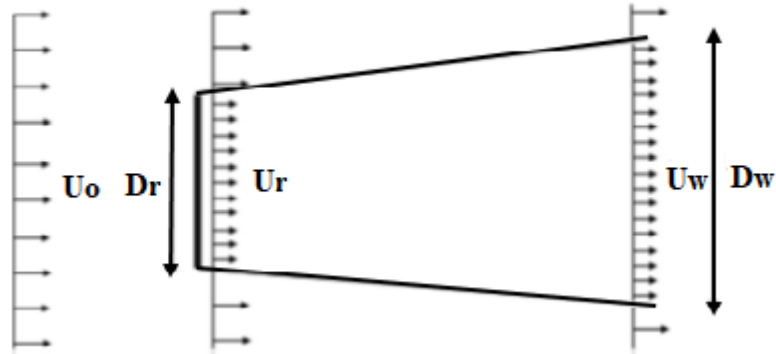
Figure 2.1. Control volume of the Jensen Wake Model [7]

21
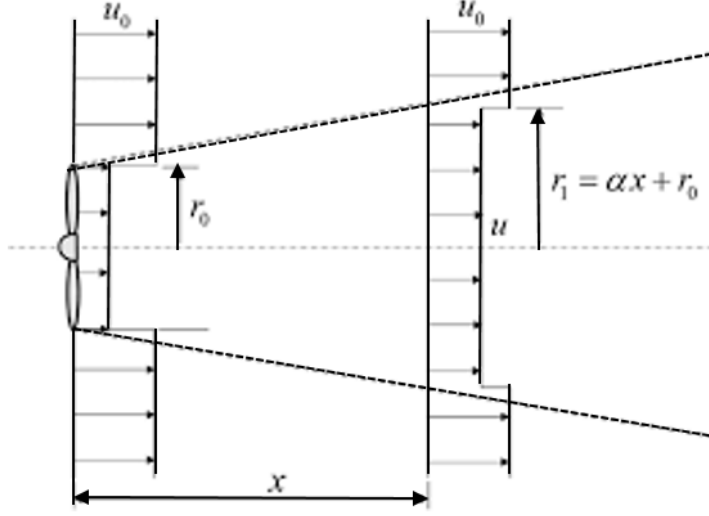
Figure 2.2. Schematic of the Jensen Wake Model [18]

In Figure 2.1, where $D=D_r$ denotes the rotor diameter, and assuming a top-hat in flow profile (Figure 2.2), the mass balance between the rotor plane and the downstream flow produces;

$$\left(\frac{D_r}{2}\right)^2 u_r + \left[\left(\frac{D_w}{2}\right)^2 - \left(\frac{D_r}{2}\right)^2\right] u_0 = \left(\frac{D_w}{2}\right)^2 u_w \qquad (2.1)$$

As previously indicated, the wake is expected to extend linearly as the downstream distance increases.

$$D_w = D_r + 2ax \qquad (2.2)$$

where,

$$\frac{U_r}{U_0} = 1 - 2a \qquad (2.3)$$

a (axial induction factor) can be calculated as:

$$a = \frac{u_0 - u_r}{u_0} \qquad (2.4)$$

Putting Eq. 2 and 3 into Eq (3), the normalized velocity can be calculated as

$$\frac{u_w}{u_0} = 1 - \frac{2a}{\left(1 + (2ax/D_r)\right)^2} \qquad (2.5)$$

The value of *a* can also be estimated using ideal axisymmetric flow, no rotation, no turbulence, and a conic shape wake profile [7]

$$a = \frac{1 - \sqrt{1 - c_T}}{2} \qquad (2.6)$$

where c_T is thrust coefficient.

To summarize the Jensen wake model, the model does not account for the impacts of increased turbulence in the downstream wake caused by changing turbine operation. However, the Jensen model can be calculated in fractions of a second and can provide the turbine interaction in a short time.

2.2   Multizone Model

This model can be considered essentially as a modification of the Jensen Model and it's published in Gebraad and Wingerden's paper [21]. It has been modified in 2 different subjects. These are related to the shape of the velocity profile in the wake region and wake overlap in the yawed condition. In defining the wake region, this model defines three different wake regions. These are named near-wake, far-wake and mixing-wake zone.
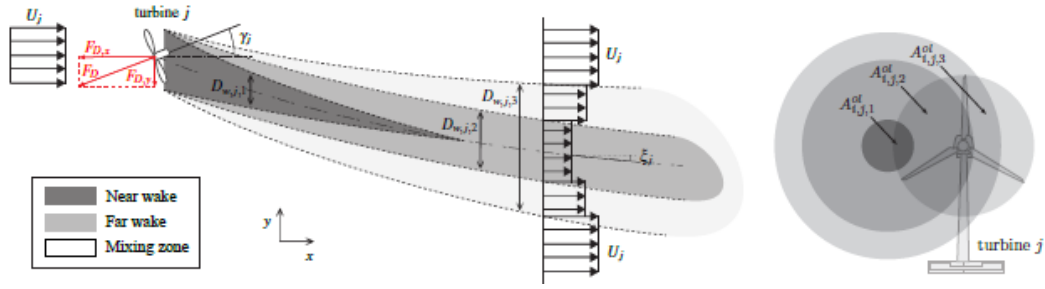
Figure 2.3. Wake regions in Multizoen model *(left: top view, right: cut-through at downstream turbine)* [72]

The downstream turbine's velocity is calculated by summing the impacts of each of the upstream turbine's wake zones.

$$u_i = U_\infty \left(1 - 2 \sqrt{\sum_j \left[a_j \sigma_{q=1}^3 \left(X_i min \left(\frac{A_{j,i,q}^{overlap}}{A_i}, 1 \right) \right) \right]^2} \right) \qquad (2.7)$$

u_i is the velocity at the downstream turbine, i,

j defines the effects of the wake zones of the upstream turbines,

X_i is the x location of the downstream turbine,

$A_{j,i,q}^{overlap}$ is the overlap area of the wake zone,

$c_{j,q}$ is the recovery of a zone q to the free stream conditions,

$$c_{j,q}(x) = \left(\frac{D_i}{D_i + 2k_e m_{U,q}(\gamma_i)[x - X_i]} \right)^2 \qquad (2.8)$$

The $m_{U,q}$ coefficients specify how fast the velocities return to free-stream velocity. For the yaw angle of the rotor, these coefficients are modified as regards:

$$m_{U,q}(\gamma_i) = \frac{M_{U,q}}{\cos(a_U + b_U\gamma_i)} \tag{2.9}$$

q defines the three wake overlap zones. a_u and b_u are model parameters that have been fine-tuned. D_i is the rotor diameter of the turbine i, γ_i is the yaw offset of turbine i, a_U and b_U specify how soon the velocity in the various wake zones returns to free-flow velocity. The parameters of the model were modified in Gebraad et al.'s research to match the results of high-fidelity wake simulations [21].

The Jensen Model's wake expansion suggests a wake that develops in proportion to the axial downstream, and the wind velocity in the wake is uniform in the axial direction, as previously stated. In this model, wake is divided into three regions (near, far, and mixed wake) that expand proportionally in the axial direction. Each region has an individual expansion factor (Figure 2.3). Wake diameters can be calculated as [72]:

$$D_{w,j,q}(x) = \max(D_j + 2k_e m_{e,q}x, 0) \tag{2.10}$$

D denotes the rotor area, and $m_{e,q}$ and k_e are the coefficients to define the expansion area. $q = 1$ corresponds to the near wake, $q = 2$ is the far wake, and $q = 3$ is the mixing region.

In order to sum up the multizone model, the compututionally inexpensive analytical model is tuned to characterize turbine interactions when turbines are operated in partial wake or yawed conditions. The number of modified parameters (for deflection, expansion, velocity and turbine itself) can be used for tuning to get sensitive results. This model, like the Jensen model does not take into consideration of turbulence or additional turbulence effect generated by an upstream turbine [69].

2.3   Gaussian Wake Model

Another wake model added to the FLORIS framework is the Gaussian Model. The model is developed by assuming a Gaussian distribution for the velocity deficit and implementing conservation of mass and momentum. The model is implemented in many papers and includes a Gaussian wake in y and z directions, added turbulence, and atmospheric stability [69].
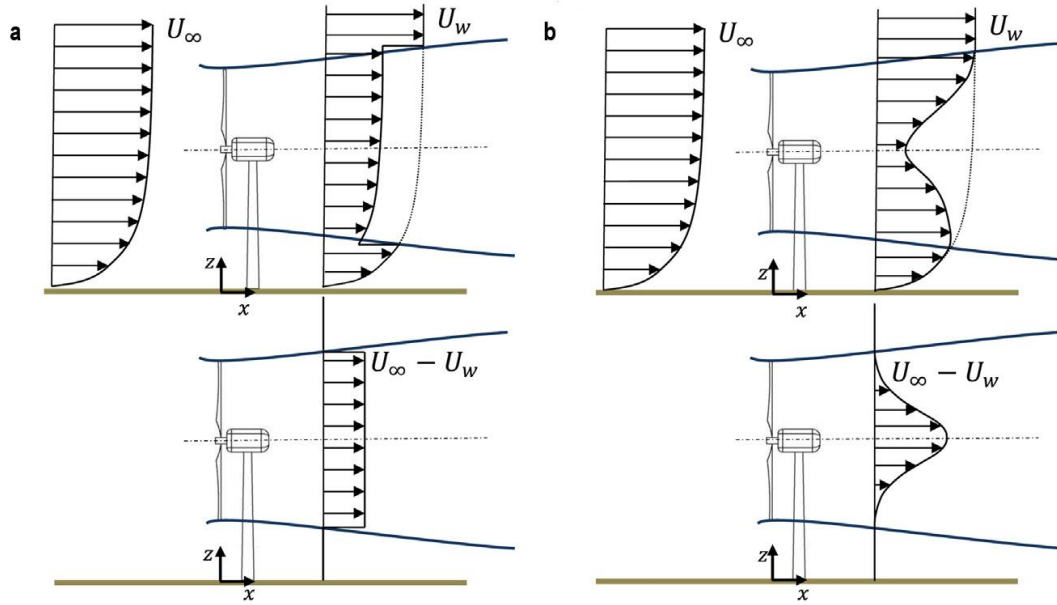
Figure 2.4. Comparison of the top-hat (a) and Gaussian (b) Velocity distribution [26]

The Jensen (also known as Park) model, or multizone model which is prefered in terms of ease of use and low computational cost, also gives an idea of energy content instead of defining a velocity field. At the same time, the power output of the turbine varies as the cube of the wind speed, and, therefore, proper evaluation of the velocity field in a wind farm is crucial for the analysis of the energy output [30]. The Gaussian distribution gives an appropriate approach for the velocity field in the downstream direction of a wind turbine.

2.3.1 Velocity Deficit

Accordig to Bastankhah and Porté-Agel's paper [30], the mass and momentum conservation equations for the wake (viscous and pressure terms are ignored) are presented as follow:

$$\rho \int U_w (U_\infty - U_w) dA = T \tag{2.11}$$

T is the thrust force in the turbine and can be calculated as:

$$T = \frac{1}{2} c_T \rho A_0 U_\infty{}^2 \tag{2.12}$$

Normalized velocity deficit:

$$\frac{\Delta U}{U_\infty} = C(x)(r/\delta(x)) \tag{2.13}$$

Where $C(x)$ is maximum normalized velocity deficit at the center of the wake, r is the radial distance, and $\delta(x)$ the characteristic wake width at each x.

The equation 2.13 can be written as:

$$\frac{\Delta U}{U_\infty} = C(x)e^{-\frac{r^2}{2\sigma^2}} \tag{2.14}$$

σ is the standard deviation of the Gaussian wake deficit at each section.

Equation 2.8 gives:

$$U_w = U_\infty \left(1 - C(x)e^{-\frac{r^2}{2\sigma^2}} \right) \tag{2.15}$$

By solving equation 2.15, $C(x)$ value can be obtain:

$$C(x) = 1 - \sqrt{1 - \frac{c_T}{8(\sigma/d_0)^2}} \tag{2.16}$$

With the linear expansion assumption, σ/d_0 can be written as:

$$\frac{\sigma}{d_0} = k^* \frac{x}{d_0} + \varepsilon \tag{2.17}$$

$k^* = \frac{\partial \sigma}{\partial x}$ is the growth rate of the wake.

ε is the value of the σ/d_0 as x goes to zero.

If we insert Equation (2.17) and (2.16) into Eq. (2.14) and rearrange, it gives:

$$\frac{\Delta U}{U_\infty} = \left(1 - \sqrt{1 - \frac{c_T}{8\left(k^* {}^x/_{d_0} + \varepsilon\right)^2}} \right.$$
$$\times exp\left(-\frac{1}{2\left(k^* {}^x/_{d_0} + \varepsilon\right)^2} \left\{ \left(\frac{z - z_h}{d_0}\right)^2 \right.\right.$$
$$\left.\left.\left. + \left(\frac{y}{d_0}\right)^2 \right\} \right) \right) \tag{2.18}$$

y and z are spanwise and vertical coordinates, and z_h is the hub height of the turbine.

In order to use Equation 2.18, it is necessary to find the value of ε.

The overall mass flow deficit rate calculated by the Frandsen Model [30] at x=0 is:

$$\int \frac{\Delta U}{U_\infty} dA = \frac{\pi}{8} d_0{}^2 \beta \left(1 - \sqrt{1 - \frac{2}{\beta} c_T} \right) \tag{2.19}$$

β is expressed as:

$$\beta = -\frac{11 + \sqrt{1 - c_T}}{2\sqrt{1 - c_T}} \tag{2.20}$$

$$\int \frac{\Delta U}{U_\infty} dA = \int\limits_0^\infty \left(1 - \sqrt{1 - \frac{c_T}{8\varepsilon^2}}\right) \exp\left(\frac{-r^2}{2\varepsilon^2 d_0^{\,2}}\right) 2\pi r dr$$

$$= 2\pi\varepsilon^2 d_0^{\,2} \left(1 - \sqrt{1 - \frac{c_t}{8\varepsilon^2}}\right) \tag{2.21}$$

When we equate Equation 2.19 and Equation 2.21, the following equation is obtained:

$$\varepsilon = 0.25\sqrt{\beta} \tag{2.22}$$

2.3.2 Atmospheric Condition

The atmospheric parameters such as shear, veer, and changes in turbulence intensity are also taken into consideration by the Gaussian model.

Based on the literature review, studies on the application of shear, veer, and turbulence intensity to this model were performed by Abkar and Porté-Agel [73] and Niayifar and Porté-Agel [74].

It should be noted that the atmospheric stability must be characterized not only with this three parameters but also with vertical fluxes and temperature profiles [80].

To give information about wind turbines and the atmospheric boundary layer (ABL), it is necessary to say that wind turbines are installed in the lowest layer of the ABL. For this reason, wind-turbine wakes are significantly affected by ABL characteristics. In other words, turbine wakes are affected by the surface characteristics and thermal propeties of the surface [75].

By using the power law of wind shear can be calculated in the Gaussian Modes as:

$$\frac{u}{U_\infty} = \left(\frac{z}{z_{hub}}\right)^\alpha \tag{2.23}$$

α is the shear coefficient[80].

Veer associated with wind is added to the model such that [75]:

$$\frac{u(x,y,z)}{U_\infty} = 1 - Ce^{-(a((y-\delta)^2)-2b(y-\delta)(z-z_{hub})+c(z-z_{hub})^2)} \tag{2.24}$$

$$a = \frac{\cos^2 \emptyset}{2\sigma_y{}^2} + \frac{\sin^2 \emptyset}{2\sigma_z{}^2} \tag{2.25}$$

$$b = -\frac{\sin 2\emptyset}{4\sigma_y{}^2} + \frac{\sin 2\emptyset}{4\sigma_z{}^2} \tag{2.26}$$

$$c = \frac{\sin^2 \emptyset}{2\sigma_y{}^2} + \frac{\cos^2 \emptyset}{2\sigma_z{}^2} \tag{2.27}$$

where $\emptyset$ is the amount of the veer.

In Abkar and Porté-Agel's paper; to investigate the effect of ABL, large eddy-simulaton and a turbine model based on the Blade Element Theory (BEM) is used. The findings of the simulations reveal that atmospheric thermal stability has a significant impact on the spatial distribution of the mean velocity deficit, turbulence intensity, and turbulent momentum fluxes in turbine wakes. It is also demonstrated that air stability has a significant impact on the wake's meandering nature [73].

Turbulence intensity, another term related to atmospheric conditioning, was used by Niayifar and Porté-Agel to empirically model the wake growth rate (k^*) of the wake behind the turbine [74].

$$k^* = 0.3837I + 0.003678 \qquad (2.28)$$

This emprical   condition is valid for the values of I (turbulence intensity) 0.065<I<0.15 [74].

2.3.3   Added Turbulence

Gaussian Wake Model includes accounts for additional turbulence caused by turbine operating as well as ambient turbulence. For example, if a turbine works at a higher thrust, the wake will recover more quickly. In contrast, if a turbine works at a lower thrust, the wake will recover more slowly [69].

This model uses the thrust coefficient and the ambient turbulence intensity to find the added turbulence at the turbine [74].

$$I_+ = \sqrt{I_{wake}^2 - I_0^2} \qquad (2.29)$$

I_{wake} is the streamwise turbulence intensity, I_0 is the ambient turbulence intensity.

An emprical equation is provided by Quarton an Ainsile [76] to predict the added turbulence:

$$I_+ = 4.8c_T^{0.7}I_0^{0.68}\left(x/x_n\right)^{-0.57} \qquad (2.30)$$

where x_n is the length of the near wake region.

$$x_n = \frac{\sqrt{0.214 + 0.144m}}{(1 - \sqrt{0.214 + 0.144m})} \frac{(1 - \sqrt{0.134 + 0.124m}}{\sqrt{0.134 + 0.124m}} \frac{r_0}{dr/dx} \qquad (2.31)$$

$m = \frac{1}{\sqrt{1-c_T}}$ and $r_0 = d_0/2\sqrt{\frac{m+1}{2}}$ and dr/dx is expressed as:

$$\frac{d_r}{d_x} = \sqrt{\left(\frac{dr}{dx}\right)_a^2 + \left(\frac{dr}{dx}\right)_m^2 + \left(\frac{dr}{dx}\right)_\lambda^2} \qquad (2.32)$$

$$\left(\frac{dr}{dx}\right)_a = 0.25I_0 + 0.005$$

$$\left(\frac{dr}{dx}\right)_m = \frac{(1-m)\sqrt{1.49+m}}{9.76(1+m)}$$

$$\left(\frac{dr}{dx}\right)_\lambda = 0.012\lambda B$$

where B is the number of the blade and λ is the tip speed ratio.

To summarize the Gaussian Wake model, It's based on approximations generated from simplified Navier-Stokes equations. It uses a linear wake expansion model with six tuning parameters to calculate the turbulence intensity and wake expansion. One of the primary concerns with the Gaussian model in FLORIS is that it tends to underestimate power gains downstream when using LES and field data. The fundamental advantages of this model stem from its linkages to actual field data like shear, veer, and turbulence intensity, as well as its origins in self-similar free shear flow theory [69].

2.4 Jimenez Wake Model

This model mostly deals with the wake condition of the turbine and examines the wake characteristic in the yaw condition, and it's analysed by Jimenez et al. [77]. When a turbine is operated in yaw conditions, it applies a force to the flow, causing the wake to deflect and deform in a specific direction. A thorough understanding of the result of deflection phenomenon would enable controlling of upstream turbine yaw angles to direct the wake away from downstream turbines, lessening its impact [77].

With a clear enough understanding of this phenomenon, upstream turbines' yaw angles might be actively controlled to divert the wake away from downstream

turbine. As a result of the yawing mechanism's reduced impact on them, the power production from the wind farm as a whole is optimized. In addition to that, A reduction in fatigue loads on downstream turbines is also realized due to the limited increase in turbulence intensity in wake region. Furthermore, because yawing can produce fatigue, this may increase fatigue in the first turbine; as a result, it should also be evaluated if the net effect is favorable [77].
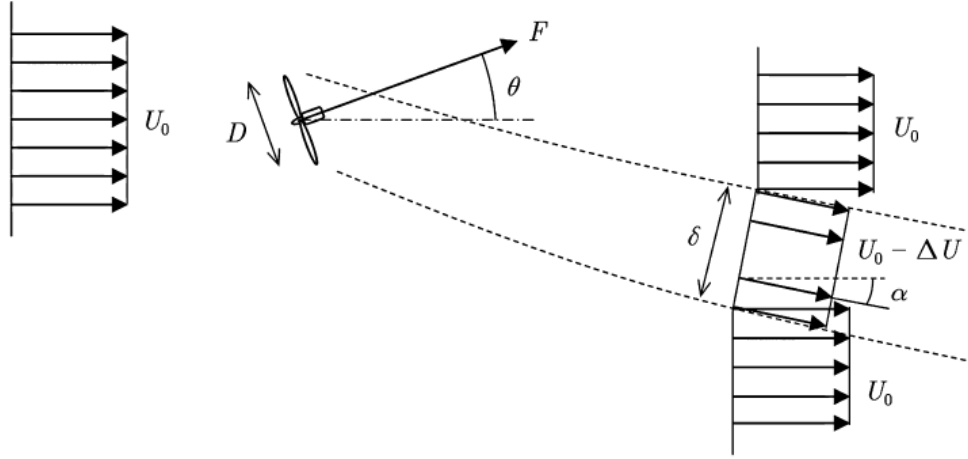
Figure 2.5. Scheme of the model [77]

According to the model initial skew angle of the wake can be calculated as:

$$\alpha_{x=0} \approx \cos^2 \theta \sin \theta \frac{C_T}{2} \tag{2.33}$$

In this model, wake cross-section is assumed to be expand linearly and the Equation 33 becomes:

$$\alpha_{x=0} \approx \frac{\cos^2 \theta \sin \theta \frac{C_T}{2}}{\left(1 + \beta \frac{x}{D}\right)^2} \tag{2.34}$$

33

$\delta = D + \beta x$ defines the linear expansion of the wake.

Value of β is range from 0.09 to 0.125.

Gebraad et al. determines the the wake deflection angle in spanwise direction [78]:

$$\theta(x) = \int_0^x \tan \alpha(x) dx \qquad (2.35)$$

$$\theta(x) \approx \frac{\alpha_{x=0} \left(15 \left(\frac{2k_d x}{D} + 1 \right)^4 + \alpha_{x=0}^2 \right)}{\frac{30k_d}{D} \left(\frac{2k_d x}{D} + 1 \right)^5} - \frac{\alpha_{x=0} D (15 + \alpha_{x=0}^2)}{30k_d} \qquad (2.36)$$

The second-order Taylor series approximation is used to approximate the $\theta(x)$ [78].

Another important paper on the analytical modeling of yaw misalignment has been published by Bastankhah and Porte-Agel [79]. Budget analysis of the Reynolds Averaged Navier-Stokes equations is used to determine the wake deflection generated by yaw misalignment of turbines.

a can be approximated as:

$$a \approx \frac{1}{2 \cos \gamma} \left(1 - \sqrt{1 - C_T \cos \gamma} \right) \qquad (2.37)$$

The skew angle of the flow *(X)* in relation to the rotor axis:

$$X = \theta + \gamma = (0.6a + a)\gamma \qquad (2.38)$$

34

The value of the wake deflection angle at the rotor can be obtained by replacing an in Equation 2.37 with a in Equation 2.38:

$$\theta \approx \frac{0.3\gamma}{\cos\gamma}\left(1 - \sqrt{1 - C_T\cos\gamma}\right) \tag{2.39}$$

The total wake deflection as a result of wake steering is calculated as follows:

$$\delta = \delta_0 + \frac{\theta_{c,0}E_0}{5.2}\sqrt{\frac{\sigma_{y0}\sigma_{z0}}{k_yk_zM_0}}\ln\left[\frac{\left(1.6 + \sqrt{M_0}\right)\left(1.6\sqrt{\frac{\sigma_y\sigma_z}{\sigma_{y0}\sigma_{z0}}} - \sqrt{M_0}\right)}{\left(1.6 - \sqrt{M_0}\right)\left(1.6\sqrt{\frac{\sigma_y\sigma_z}{\sigma_{y0}\sigma_{z0}}} + \sqrt{M_0}\right)}\right] \tag{2.40}$$

$\delta_0 = x_0 \tan\theta$

x_0 is the length of the near-wake of the Bastankhah and Porte-Agel's paper.

$E_0 = {C_0}^2 - 3e^{1/12}C_0 + 3e^{1/3}$

k_y and k_z the rates of wake growth in both the horizontal and vertical directions, σ defines the wake widths in x,y and z directions.

$M_0 = C_0(2 - C_0)$

C_0 is the difference in velocity between the incoming and outgoing velocity at the wake center.

2.5   Curled Wake Model

Another wake model in the FLORIS framework is the model which is presented by Martinez-Tossas et al. [24] and called as *"Curled Wake"*. The main principle behind the curled wake can be identified as a collection of vortices that are released from the top and bottom of the rotor when the turbine is in a yawed condition. Consequently, the wake is pushed to the side by these vortices, resulting in a curled wake shape. In other words, when the tubine is yawed, a curled wake occurs.

Because the wake in yawed situations is not only deflected in the reverse direction of the yaw angle, but also changes shape. This mechanism was first described in a paper published by Howland et al. [24].

Martinez-Tossas et al. developed a curled wake model that computes the wake from each turbine using a linearization of the Navier-Stokes equation with some approximations. In addition, this model was compared the LES results using the actuator disc and the actuator line models and the outcome demonstrates reasonable validity [24].
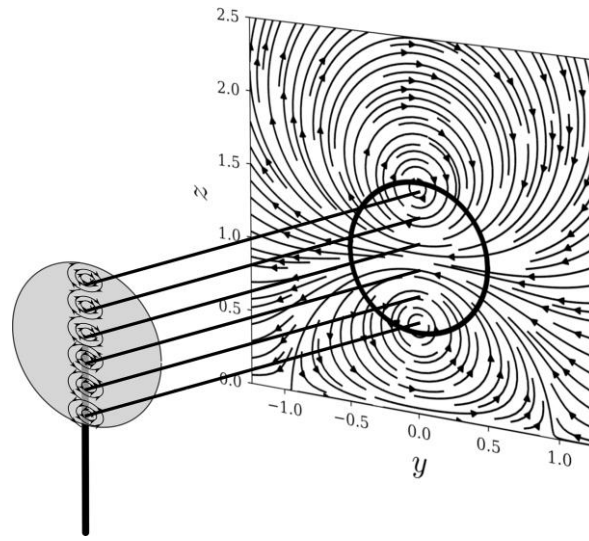
Figure 2.6. The downstream distribution of spanwise velocities due to the superposition of the vortices is illustrated in this diagram [38]

A spread of counter-rotating vortices is introduced to the underlying flow solution to create the curled wake effect. The curled wake shape is formed by the superposition of all the vortices, which results in a spanwise velocity field.

According to the Martines-Tossas et al. each vortex is calculated as:

$$u_t = \frac{\Gamma}{2\pi r}\left(1 - exp\left(-r^2/\sigma^2\right)\right) \qquad (2.41)$$

u_t is the tangential velocity, r is the distance between the vortex center and the observer, Γ is the circulation strength, σ is the vortex core vidth.

The circulation strength can be calculated as a function of the thrust coefficient.

$$\Gamma = \frac{\pi}{8}\rho D U_\infty C_T \sin\gamma \cos^2\gamma \qquad (2.42)$$

C_T is the thrust coefficient, amd γ is the yaw angle.

In the curled wake model, the symmetric assumption holds true, and the entire circulation exits the rotor area via the shed vortices. The vortices are assumed to not deteriorate as they are convected downstream in the current design.

The disk's form is matched by a discrete elliptic distribution of shed vortices:

$$V_{wake\ rotation} = \sum_{i=1}^{N} \frac{y_i \Gamma_i}{2\pi(y_i^2+z_i^2)}\left(1 - exp\left(-\left(\left(y_i^2+z_i^2\right)\Big/\sigma^2\right)\right)\right) \qquad (2.43)$$

$$W_{wake\ rotation} = \sum_{i=1}^{N} \frac{z_i \Gamma_i}{2\pi(y_i^2+z_i^2)}\left(1 - exp\left(-\left(\left(y_i^2+z_i^2\right)\Big/\sigma^2\right)\right)\right) \qquad (2.44)$$

Each of the vortices spread on a line between the top and bottom of the rotor diameter is represented by the index i, N is the number of the vorticies, y_i and z_i are placed on the shed vortex's position. The vortex core's size is set to $\sigma = \frac{D}{5}$.

The elliptical distribution is related to the strength of each vortex:

$$\Gamma_i = -4\Gamma_0 \frac{r_i{}^2}{ND^2 \sqrt{1 - \left(\left(2r_i/D\right)\right)^2}}$$

(2.45)

In the rotor coordinate system, r_i is the radial location of the i$^{\text{th}}$ vortex and $\Gamma_0 = 4/\pi\Gamma$

2.6 Gauss Curled Hybrid (GCH) Model

This model proposes a hybrid wake model that combines analytic approximations of the curl model with the Gaussian model, and for this reason, it is called the GCH model and published by King et al. [40]. One of the key differences between this model and others is that, whereas other models focus on the aerodynamic interaction of wake steering between two different turbines, this model can also examine the effects on more than two turbines. In this model, the concept of secondary effects of wake steering is also covered. This secondary effect of wake steering is called as secondary steering.

Turbines operating in yaw-misaligned conditions generate counter-rotating vortices, as detailed in earlier sections. The vortices, in particular, spread far downstream, dissipate, and influence all downstream turbines directly that generated the vorticies. When the vortices approach a downstream turbine, they cause secondary steering by impacting the downstream turbine's wake. In other words, even when the downstream turbine is aligned with the flow, the spanwise and vertical velocities of upstream turbines affect the deformation and deflection of a wake downstream as if the downstream turbine were applying wake steering. At the downstrem turbine, the counter-rotating vortices acted as an effective yaw angle. Even when the turbine in the wake region is aligned with the flow, the spanwise and vertical velocity components of upstream turbines have an impact on the deflection and deformation of a wake downstream as if the downstream turbine were employing wake steering [40]. Figure 2.7 presents the schematic for the formation of the effective yaw angle.
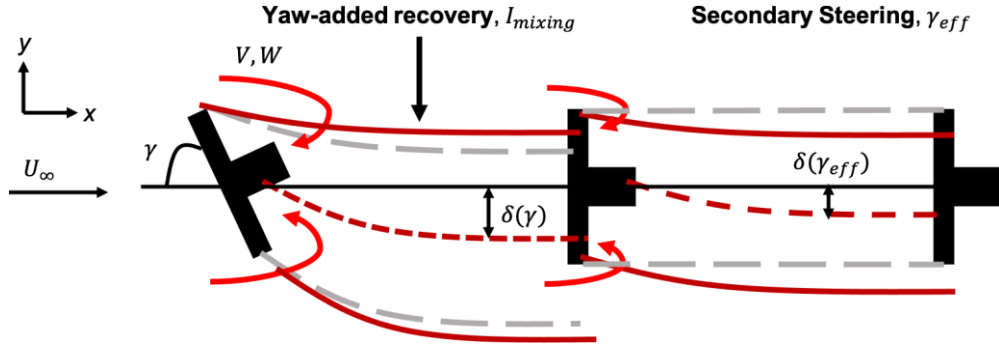
Figure 2.7. Model scheme of secondary steering [40]

To calculate the effective yaw angle, it is necessary to model the secondary steering. For this, it is necessary to describe the effect of vortices created by the upstream turbine on the wake of the downstream turbine.

Before proceeding to the calculation of the effective yaw angle, it'd better mention the additional spanwise and vertical velocity components formed on the top and bottom sides of the turbine by the counter rotating vortices [40].

$$V_{wake} = V_{top} + V_{bottom} + V_{wake\ rotation} \qquad (2.46)$$

$$W_{wake} = W_{top} + W_{bottom} + W_{wake\ rotation} \qquad (2.47)$$

$V_{wake\ rotation}$ and $W_{wake\ rotation}$ are computed in Matines-Tossas' paper [24] and presented in equation 2.43 and 2.44

$$V_{top} = \frac{\Gamma_{top}(z - z_h + D/2)}{2\pi \left((y - y_0)^2 + \left(z - (z_h + D/2)\right)^2\right)} \left(1 \right.$$
$$\left. - exp \frac{-\left((y - y_0)^2 - \left(z - (z_h + D/2)\right)\right)^2}{\sigma^2}\right)$$

(2.48)

$$V_{bottom} = \frac{\Gamma_{bottom}(z - z_h - D/2)}{2\pi \left((y - y_0)^2 + \left(z - (z_h - D/2)\right)^2\right)} \left(1 \right.$$
$$\left. - exp \frac{-\left((y - y_0)^2 - \left(z - (z_h - D/2)\right)\right)^2}{\sigma^2}\right)$$

(2.49)

V_{top} and V_{bottom} come from the rotor's rotating vortex at the top and bottom. Γ_{top} and Γ_{bottom} can be calculated according to the Equation 2.45. Similarly:

$$W_{top} = \frac{\Gamma_{top}(y - y_0)}{2\pi \left((y - y_0)^2 + \left(z - (z_h + D/2)\right)^2\right)} \left(1 \right.$$
$$\left. - exp \frac{-\left((y - y_0)^2 - \left(z - (z_h + D/2)\right)\right)^2}{\sigma^2}\right)$$

(2.50)

$$W_{bottom} = \frac{\Gamma_{bottom}(y - y_0)}{2\pi \left((y - y_0)^2 + \left(z - (z_h - D/2)\right)^2\right)} \left(1 \right.$$
$$\left. - exp \frac{-\left((y - y_0)^2 - \left(z - (z_h - D/2)\right)\right)^2}{\sigma^2}\right)$$

(2.51)

Finally, the dissipation of these vortices is identified in the following equations:

$$V = V_{wake} \left(\frac{\sigma^2}{4\nu_T \frac{(x - x_0)}{U_\infty} + \sigma^2} \right) \tag{2.52}$$

$$W = W_{wake} \left(\frac{\sigma^2}{4\nu_T \frac{(x - x_0)}{U_\infty} + \sigma^2} \right) \tag{2.53}$$

where ν_T is the turbulent viscosity and calculated based on the mixing length model:

$$\nu_T = l_m{}^2 \frac{\partial U}{\partial z} \tag{2.54}$$

where $l_m = \frac{kz}{1 + kz/\lambda_T}$, k=0.41, $\lambda_T = D/8$, In a free atmosphere, λ_T is the value of the mixing length [41].

After calculating the V_{wake} value, it can then proceed to calculate the effective yaw angle (γ_{eff}) value. The difference between the effective spanwise velocity and the spanwise velocity calculated at the rotor is minimized to find γ_{eff}:

$$\gamma_{eff} = argmin|\bar{V} - V_{eff}| \tag{2.55}$$

$$V_{eff} = V_{wake}(\gamma) \tag{2.56}$$

Total wake deflection can be expressed as:

$$\gamma = \gamma_{turb} + \gamma_{eff} \qquad (2.57)$$

γ_{turb} is the exact amount of yaw offset applied by the turbine.

2.7   Turbo Park Model

The latest wake model inserted into the FLORIS framework is called the Turbopark Model, and its details are reviewed in the paper published by Nygaard et al. [22]. In this model, two different new wake models have been proposed for wind turbine interaction, and a methodology has been created to bring these models together. The first model presented by Nygaard et al. is essentially an improvement of the model described in the previous section, also called the Park model, with a top-hat velocity profile in the wake region. In this model, ambient turbulence and turbulence generated in the wake region have also been added to the existing model. Because turbulence effects are incorporated into the model, this model is assumed to be more suitable for describing wake recovery over long ranges, such as between wind farms.

The second model examines the effect caused by the holistic effect of wind farm. This model, called wind farm blockage, is based on the approach that the effect contributed by each turbine creates a total effect in a wind farm. This total blockage effect created by the wind farm directly affects the production of that wind farm.

These two models are linked because the outcomes of one model feed into the inputs of the other, and vice versa. The connection between these two models was determined by an iteration method suggested in the paper.

2.7.1   Determination of the Wake Expansion

Nygaard et al. propose a locally linear wake expansion [22]:

$$\frac{dD_w}{dx} = AI(x) \tag{2.58}$$

where, $I(x)$ determines the local turbulence intensity, A is constant for calibration, D_w is wake expansion.

The Frandsen wake turbulence model [32] is proposed for determining $I(x)$.

$$I(x) = \sqrt{I_0{}^2 + I_w{}^2(x)} \tag{2.59}$$

where I_0 is the atmospheric turbulence and I_w is the generated turbulence.

$$I_w(x) = \frac{1}{c_1 + c_2 \dfrac{x/D}{\sqrt{c_T(V_{in})}}} \tag{2.60}$$

c_1 and c_2 are given as 1.5 and 0.8, respectively [80].

The local expansion rate is integrated from the rotor to where the wake width is assumed to be equal to the rotor diameter to determine the wake diameter.

$$
\begin{aligned}
D_w(x) = D + \frac{AI_0 D}{\beta} \Bigg(& \sqrt{(\alpha + \mathcal{E}x/D)^2 + 1} - \sqrt{1 + \alpha^2} \\
& - \ln\left[\frac{\left(\sqrt{(\alpha + \mathcal{E}x/D)^2} + 1\right)\alpha}{(\sqrt{1+\alpha^2}+1)(\alpha + \mathcal{E}x/D)} \right] \Bigg)
\end{aligned}
\tag{2.61}
$$

where $\alpha = c_1 I_0$ and $\mathcal{E} = c_2 I_0 / \sqrt{C_T(V_{in})}$ and added to equation as additional variables. A is defined as expansion parameter and is assumed to 0.6 [22].

2.7.2　　　Aggregated Wind Farm Effect

In this paper, a new aspect has been developed separately from other wake models. Apart from the wind speed reduction originating from a single turbine, the effect of wind farm as a whole on velocity reduction has been investigated. This new model is based on the assumption that the induction effects of each turbine in a wind farm generate an overall effect, and this effect is called wind farm blockage. Aside from this publication, researches of by Bleeg et al. [80], and Segalini and Dahlberg [81] have revealed wind speed reductions upstream of wind farms, which are consistent with a blocking effect caused by the wind farms.

A vortex cylinder model is used to describe the buildup of single-turbine induction effects in the simple wind farm obstruction model. The generated axial velocity in the vortex cylinder model is axisymmetric around the rotor's center, dependent only on the spanwise position x. It is assumed that the axial and streamwise velocity components are equivalent. Vortex cylinder model defines an actuator disk in uniform flow (Equation 2.62). Vorticity in this model is a function of inflow speed and thrust coefficient.

$$
u(x,r) = \frac{\gamma}{2} \left(\frac{R - r + |R - r|}{2|R - r|} \right.
$$
$$
+ \frac{xm(x,r)}{2\pi\sqrt{rR}} \left[K\big(m(x,r)\big) \right.
$$
$$
\left. + \frac{R - r}{R + r} \Pi(m(0,r), m(x,r)) \right] \Bigg)
$$

(2.62)

K and Π are the elliptic integrals first and second kind respectively. r is the radial distance from rotor centre. γ is the vorticity and m is the dependent variable according to rotor radius.

$$m\left(x,r\right) = \frac{4rR}{x^2 + (R+r)^2} \tag{2.63}$$

In the scope of the thesis study, 4 different analytical wake models in the FLORIS framework is introduced. Jensen, Multizone, Gaussian and GCH wake models are the implemented wake models in the interfarm wake interactions studies. Jensen and Multizone wake model includes top-hat shape velocity distribution in wake region (see Figure 2.2), and gaussian shape velocity distribution occurs in wake region in GCH and Gaussian wake model (see Figure 2.4). Besides, the Multizone wake model is the developed version of the Jensen wake model and GCH wake model is the developed version the Gaussian wake model. Thus, it is aimed to investigate different velocity distributions in wake region and modified versions of the wellknown Jensen and Gaussian wake models.

CHAPTER 3

ANALYSIS OF THE INTER-FARM INTERACTION

This section presents an investigation that focuses on inter-farm cluster-wake interactions for two on-shore wind farms that are in close proximity of each other (3 km) and are located in northern part of Turkey close to the Black Sea coast. Because of the terrain, there are significant elevation differences between turbines and this is modeled through an easy to implement terrain elevation representation that takes into account relative hub height and rotor overlap positions while using realistic estimates (i.e. consistent with SCADA data) for hub height velocity levels despite potentially large differences in hub heights of the wind turbines. The simulations are performed using FLORIS framework with and without terrain elevation representation using four different wake models that are available in FLORIS (i.e. Jensen, Multizone, GCH and Gaussian)

3.1 Studied Wind Farms

Two onshore wind farms located in the northern region of Turkey near the Black Sea coastline are selected for this study. The location of the wind farms is shown in Figure 3.1.

Figure 3.1. Location of selected wind farms in the northern region of Turkey

The turbine layout of both wind farms are given in Figure 3.2. The wind farm more to the south is known as Kayadüzü wind farm as marked in the figure and it includes 30 wind turbines positioned over the terrain as shown. The wind farm to the north is known as the Havza wind farm and it consists of 16 turbines. The terrain on which these wind farms are positioned is quite complex and there is significant elevation differences between the turbines in wind farms, as will be shown in more detail later. These wind farms are specially chosen due to the fact that they are in very close proximity of each other, about 3 km, and they experience wake interactions from each other. The locations of wind farms and the coordinates of their turbines are obtained from the database of Energy Market Regulatory Authority of Turkey (EMRA) that contains all wind farms and turbine coordinates. Details regarding the selected wind farms are given in Table 3.1.
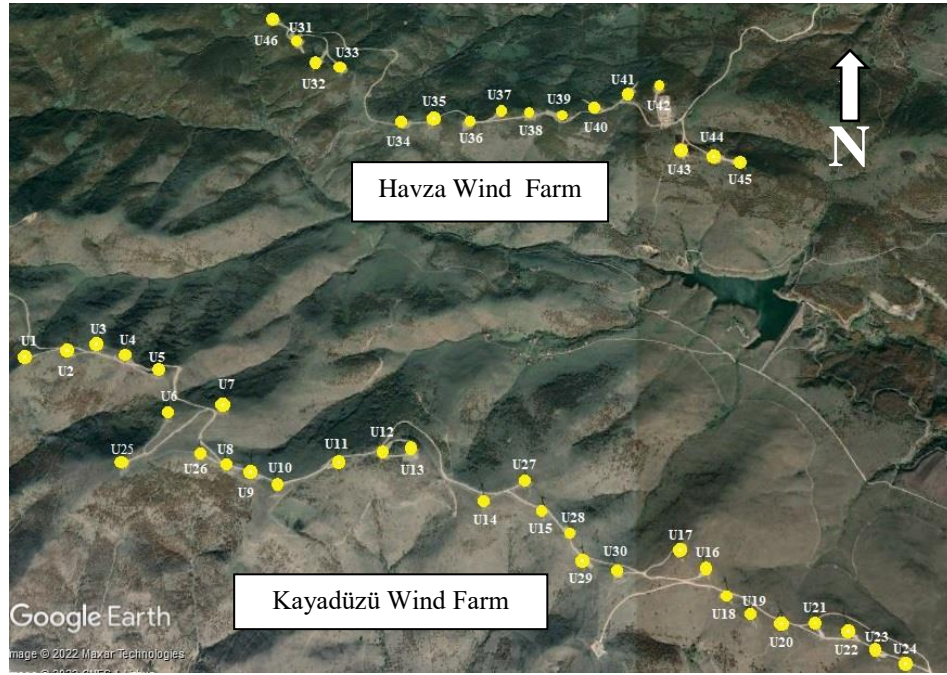
Figure 3.2. Turbine layouts of the selected wind farms.

Table 3.1 Details of Kayadüzü and Havza wind farms used in this study

	Capacity [MW]	Number of turbines	Rated power [MW]	Rotor diameter [m]	Hub height [m]
Kayadüzü	82	30	**2.5 MW** *(U1-U10 and U19-U24)* **3 MW** *(U11-U18) and U25-U30)*	**99.8** *(U1-U10 and U19-U24)* **116.8** *(U11-U18) and U25-U30)*	**80** *(U1-U10 and U19-U24)* **91** *(U11-U18) and U25-U30)*
Havza	56	16	3.5	138	111

The power curve and cp-ct plots of the 2.5 MW and 3 MW turbines of Kayadüzü wind farm are presented in Figure 3.3 [82], [83]. C_p and C_T tables of all turbines in both wind farms are inserted to FLORIS code.

(a)   (b)

(c)   (d)
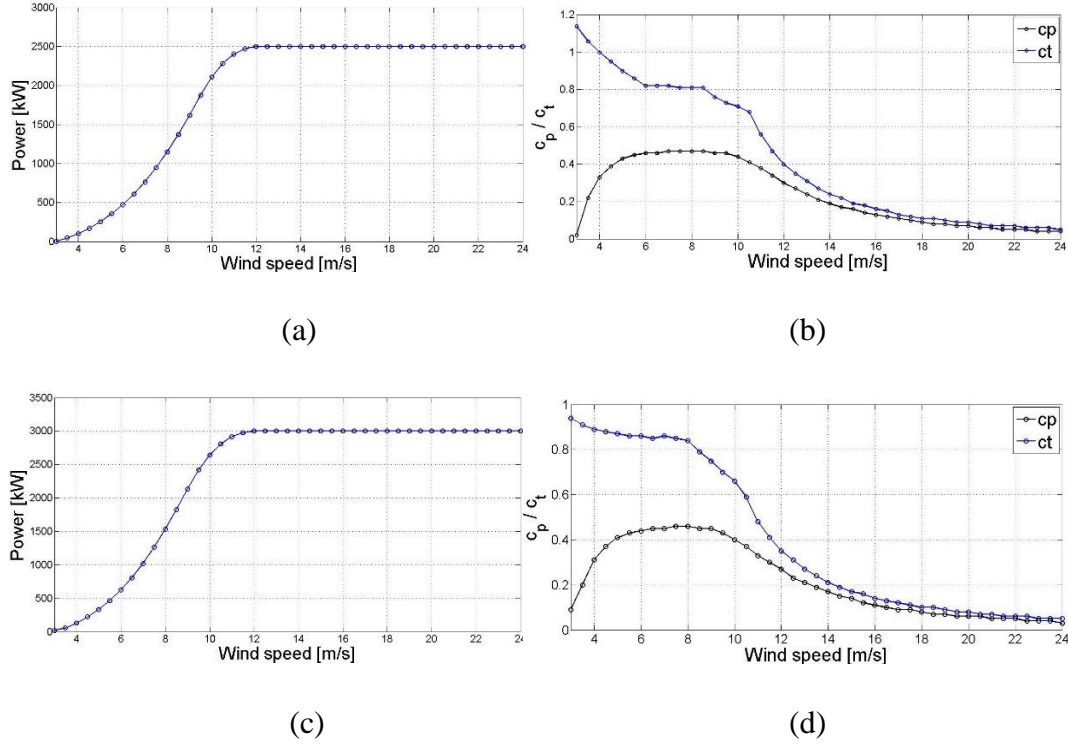
Figure 3.3. Power curve and cp-ct plots of the 2.5 MW Nordex N100 (a)-(b) and 3 MW Nordex N117 (c)-(d) model turbines of Kayadüzü wind farm

Field data are obtained from the SCADA system of Kayadüzü wind farm, which includes 10-minute average wind speed and direction data for all turbines in the farm for the year 2021. This dataset was recorded between January 17 and December 31 in 2021 resulting in a dataset that is available for a total of 8350 hours. In addition, the SCADA system also provided 10-minute average turbine based power generation data as well. Figures 3.4 and 3.5 show the windrose and histogram superimposed with corresponding Weibull distribution, respectively, obtained using the SCADA data for Kayadüzü wind farm. Note that the wind direction is predominantly from South-Southwest most of the year, indicating that for most part of the year Havza

wind farm, which is situated to the north of Kayadüzü, will be operating under the cluster wake influence of the Kayadüzü wind farm. In fact, using the SCADA data we calculated that Havza wind farm operates under the influence Kayadüzü wind farm about 79 % of the year, as will be explained in more detail later in this section.
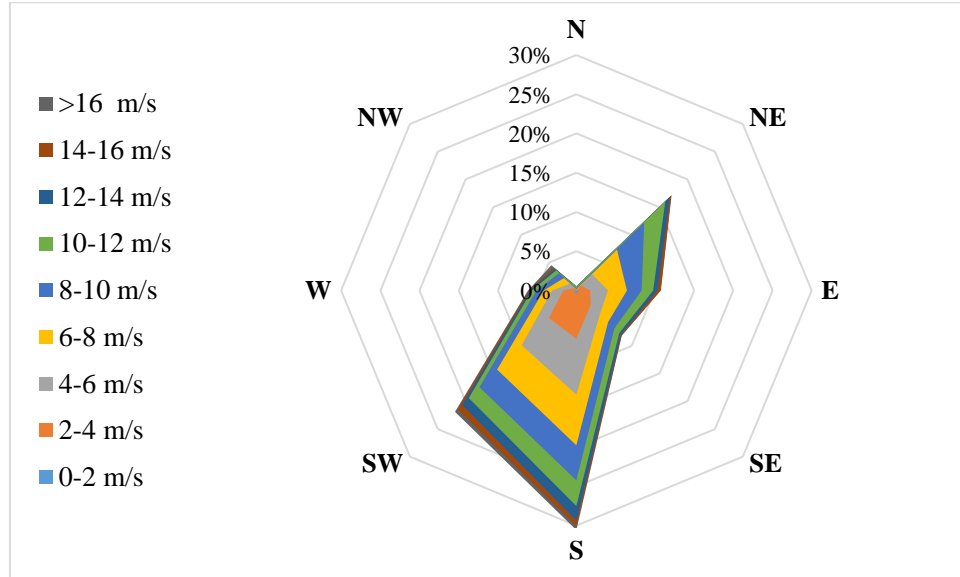
Figure 3.4. Wind rose generated using the SCADA data from Kayadüzü wind farm for the year 2021
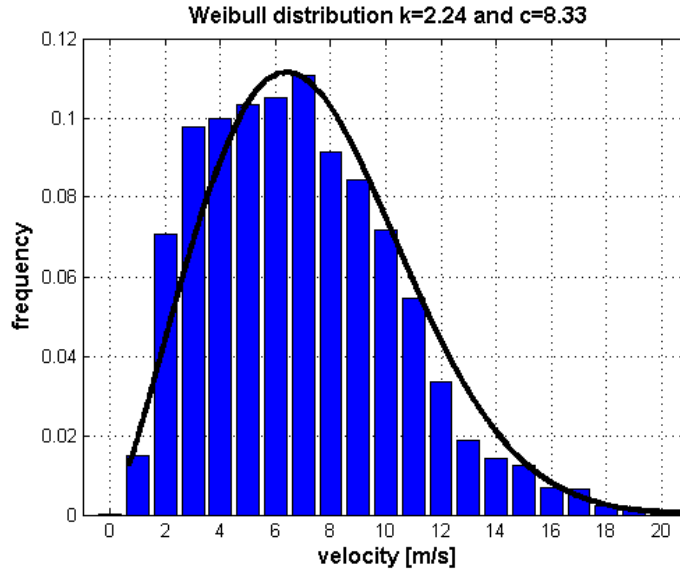
Figure 3.5. Wind speed histogram and Weibull distribution obtained using the SCADA data from Kayadüzü wind farm for the year 2021

3.2   FLORIS Simulation Methodology with Terrain Elevation

In a typical FLORIS simulation of a wind farm with no elevation difference between turbine hub heights (i.e. similar to those in off-shore wind farms), all turbine rotors are placed at the same hub height (if there are no variations in make and model and in tower heights) and a reference velocity and an elevation is specified, which in turn are used to calculate hub height velocities through the power law relation given as,

$$u_{HH} = u_{Ref} \left(\frac{z_{HH}}{z_{Ref}} \right)^{\alpha}$$

(3.1)

If the hub height velocity measurements are available, the reference values are usually taken as equal to the hub height values. Figure 3.6a conceptually illustrates such a scenario where all the turbine rotors are at the same hub height (i.e. $z_{HH1}=z_{HH2}=\ldots=z_{HHn}$).

52

For an on-shore wind farm on complex terrain, however, there can be significant differences in turbine elevations within a wind farm in addition to the fact that there could be tower height variations depending on the location of the turbine as well as depending on its make and model. Such a scenario is conceptually presented in Figure 3.6b. As one can see, each turbine can be positioned at a certain terrain elevation from sea level (marked using parameter z_{TE}) and each turbine can have its own tower height (z_{HH}). In such a scenario, the wakes of certain turbines in a wind farm may not interact with other downstream turbines in the farm or with turbines in other closeby wind farms when there is sufficiently large elevation difference between them or the wakes may partially be impacting the downstream turbines.

(a)

(b)

53

(c)
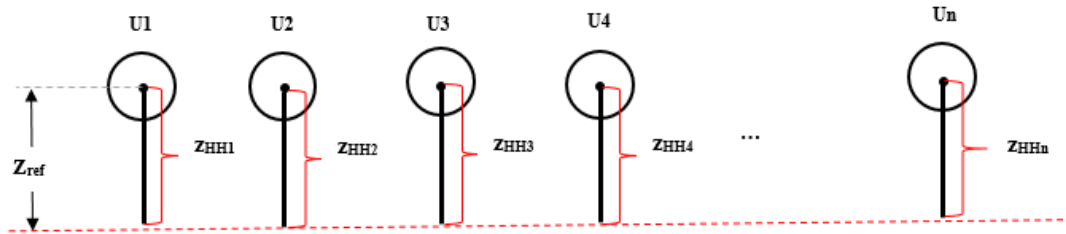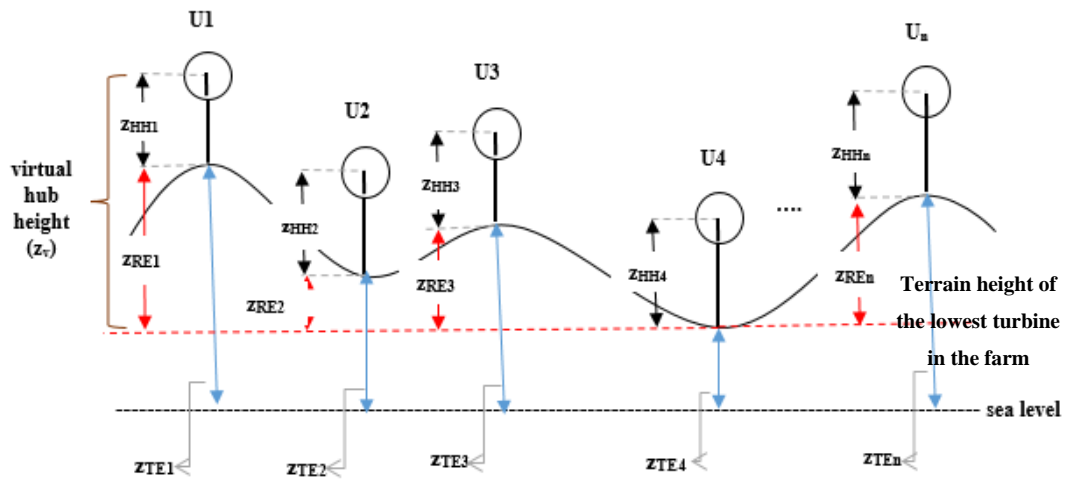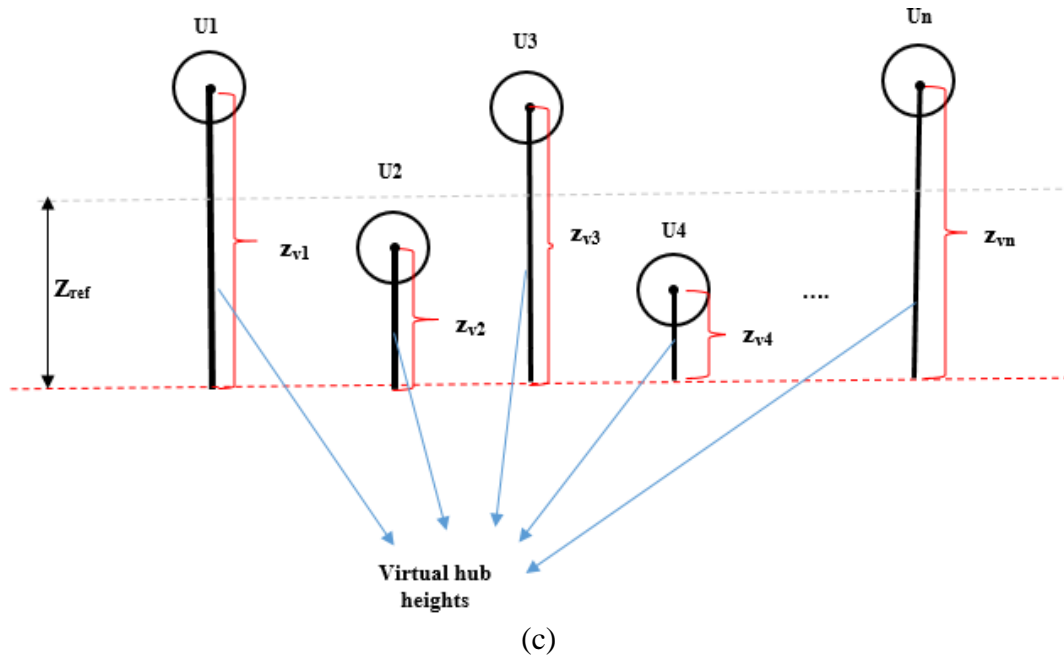
Figure 3.6. Conceptual representation of (a) wind turbines on simple terrain (b) wind turbines on complex terrain and (c) FLORIS simulation model of complex terrain by placing all turbines at their respective virtual hub height positions.

Table 3.2 Hub height, virtual hub height and elevation data for Kayadüzü and Havza wind farms. Turbines 1-30 are in Kayadüzü wind farm and turbines 31-46 are in Havza wind farm

Turbine No.	Turbine Power [MW]	Rotor Diameter [m]	Hub Height (z_{HH}) [m]	Terrain Elevation (z_{TE}) [m]	Relative Elevation (z_{RE}) [m]	Virtual Hub Height (z_V) [m]
U1	2.5	100	80	1273	238	318
U2	2.5	100	80	1287	252	332
U3	2.5	100	80	1286	251	331

Table 3.2 cont'd

U4	2.5	100	80	1300	265	345
U5	2.5	100	80	1308	273	353
U6	2.5	100	80	1301	266	346
U7	2.5	100	80	1265	230	310
U8	2.5	100	80	1224	189	269
U9	2.5	100	80	1225	190	270
U10	2.5	100	80	1227	192	272
U11	3	117	91	1249	214	305
U12	3	117	91	1234	199	290
U13	3	117	91	1235	200	291
U14	3	117	91	1182	147	238
U15	3	117	91	1151	116	207
U16	3	117	91	1123	88	179
U17	3	117	91	1086	51	142
U18	3	117	91	1051	16	107
U19	3	100	80	1037	2	82
U20	2.5	100	80	1035	0	80
U21	2.5	100	80	1036	1	81
U22	2.5	100	80	1038	3	83
U23	2.5	100	80	1038	3	83

Table 3.2 cont'd

U24	2.5	100	80	1080	45	125
U25	3	117	91	1295	260	351
U26	3	117	91	1245	210	301
U27	3	117	91	1175	140	231
U28	3	117	91	1154	119	210
U29	3	117	91	1133	98	189
U30	2.5	117	91	1119	84	175
U31	3.5	136	111	1190	155	266
U32	3.5	136	111	1228	193	304
U33	3.5	136	111	1220	185	296
U34	3.5	136	111	1157	122	233
U35	3.5	136	111	1160	125	236
U36	3.5	136	111	1185	150	261
U37	3.5	136	111	1186	151	262
U38	3.5	136	111	1186	151	262
U39	3.5	136	111	1184	149	260
U40	3.5	136	111	1155	120	231
U41	3.5	136	111	1130	95	206
U42	3.5	136	111	1163	128	239
U43	3.5	136	111	1146	111	222

Table 3.2 cont'd

U44	3.5	136	111	1124	89	200
U45	3.5	136	111	1128	93	204
U46	3.5	136	111	1175	140	251

Therefore, we first calculate relative elevation values for each turbine in a wind farm (z_{RE}). This value is the elevation of any turbine with respect to the turbine that is positioned at the lowest elevation level in the farm, as shown in Figure 3.7b. Then we combine the relative elevation level with the hub height of each turbine and determine what we define as "virtual hub height", marked as z_V in Figure 3.7b. Afterwards, in order to be able to construct a FLORIS simulation model we place all turbines on flat terrain but now placing all rotors at their respective virtual hub height position, as shown in Figure 3.7c. This layout will make sure the terrain elevation differences are represented to a certain degree in FLORIS and therefore wind farm wake interactions will be more realistic compared to the case where all the turbine rotors are taken at the same hub height, as given in Figure 3.7a. Table 3.2 shows relevant hub height, virtual hub height and elevation data for the two on-shore wind farms, i.e. Kayadüzü and Havza wind farms, interactions of which are attempted to be simulated using FLORIS in this study. The terrain elevation data are obtained using Google Earth for the known turbine coordinates.

One should note that for the FLORIS simulation of the wind farms given in Table 3.2, the virtual hub height difference between the lowest (Turbine 20 with z_V=80 m) and the highest turbine (Turbine 5 with z_V=353 m) is 273 m. This large difference in hub heights creates a problem regarding determination of realistic (i.e. consistent with SCADA data) hub height wind velocities for the simulation. As explained before for the simple case depicted in Figure 3.7a defining a proper reference velocity and height is sufficient and FLORIS uses a power law to determine the hub height velocity values. However if one uses similar reference velocity and height for a simulation that has turbines with a wide range of hub heights as given in Table 3.2,

57

the hub height velocity levels for the highest turbines would be unrealistically high, i.e. much higher than those observed in the SCADA data. Also, in the current version of FLORIS, it is not possible to explicitly specify different hub height velocity values or reference height values separately for each front row turbine in a farm simulation. Therefore, here we propose the following approximate approach to obtain more realistic hub height velocity distribution for this kind of simulation.

Using the SCADA data from Kayadüzü wind farm, we first calculate the average hub height velocity level for each simulation using the measured hub height wind velocities. Keep in mind that we are performing hourly simulations for an entire year and the calculated average hub height velocity level is for the hour of the simulation. Then we assume that this average value is equal to the average hub height velocities in the simulation and also equal to the reference velocity (u_{ref}) needed for the power law calculation. Hence,

$$\bar{u}_{Scada} = \bar{u}_{Floris} = u_{Ref} = \bar{u}_{HH} \tag{3.2}$$

where,

$$\bar{u}_{Scada} = \frac{1}{N} \sum_{i=1}^{N} u_{Scada}^i \text{ and } \bar{u}_{Floris} = \frac{1}{N} \sum_{i=1}^{N} u_{Floris}^i \tag{3.3}$$

and N is the number of wind turbines at Kayadüzü wind farm, i.e. $N=30$ for this simulation. Therefore the turbine hub height velocities for each turbine can be calculated during the simulation using,

$$u_{HH}^i = u_{Ref} \left(\frac{z_V^i}{z_{Ref}} \right)^\alpha \tag{3.4}$$

Here, i is the index again for the turbine number in the simulation. In this equation, however, z_{Ref} is an unknown in addition to u_{HH}^i. The reason is that because of the large variations in hub heights, as explained in the previous paragraph, choosing a

proper z_{Ref} value is not straight forward. In order to overcome this issue we combine equations 3.2, 3.3 and 3.4 to obtain,

$$u_{Ref} = \bar{u}_{HH} = \frac{1}{N}\sum_{i=1}^{N} u_{Floris,HH}^i = \frac{1}{N}\sum_{i=1}^{N} u_{Ref}\left(\frac{z_V^i}{z_{Ref}}\right)^\alpha \qquad (3.5)$$

and from this equation an expression for a virtual reference height, $z_{Ref\text{-}V}$, can be derived as,

$$z_{Ref-V} = \left[\frac{\sum_{i=1}^{N}\left(z_V^i\right)^\alpha}{N}\right]^{\frac{1}{\alpha}} = \left[\frac{\left\{(z_V^1)^\alpha + (z_V^2)^\alpha + \cdots + \left(z_V^N\right)^\alpha\right\}}{N}\right]^{\frac{1}{\alpha}} \qquad (3.6)$$

For the simulation of the on-shore wind farms investigated in this study, $z_{Ref\text{-}V}$ is calculated as 221 m and this value is used as the "specified wind height" parameter in current FLORIS simulations. One should note that, in the case that the FLORIS simulation is being performed for a wind farm on a flat terrain (such as in offshore wind farms) with turbines all having the same hub height, the above formulation simply gets reduced to equation 3.1. If the wind farm is on flat terrain but there are still relatively minor variations in hub height values of the turbines, above formulation and methodology still can be used to obtain better estimates since it will allow taking into account the variations in wake heights of individual turbines.

Figure 7 shows the implementation of above formulation for a sample wind condition case on 2 February 2021 at 17:00 hours during which Havza wind farm operates under the cluster wake influence of Kayadüzü wind farm. On this specific day and time average hub-height wind speed is 8.45 m/s and at 202 degrees from North as obtained from the SCADA data and as shown on in Figure 3.7a. For this sample case where Kayadüzü wind farm turbines will be facing the oncoming wind condition,

actual terrain elevation + hub height ($z_{TE}+z_{HH}$) variation is presented in Figure 3.7b (wind into the page). Figure 6c shows the case if all Kayadüzü turbines would be placed on flat terrain, showing only variations in hub height due to the differences in their respective tower heights. Figure 3.7d shows the case when we implement the terrain elevation representation proposed above using the virtual hub height (z_V) distribution. As indicated before, in this representation the hub height difference between the highest and the lowest wind turbine is 273 m as shown, and a proper way for calculation of hub height velocities for FLORIS simulation is needed, such as the one proposed previously based on a virtual reference height calculation (z_{Ref-V}). In order to demonstrate the extent of wake interaction zones between the two farms for this wind condition, Figure 3.7e presents a comparison of virtual hub heights for both wind farms along an axis (marked as *x'* in Fgure 3.7a) that is normal to the wind direction. The rotor upper and lower boundaries are also marked on the figure to show overlapping regions of rotor disks of Kayadüzü and Havza wind farms. As can be seen many partial wake interaction regions exist and now can be taken into account in the FLORIS simulation with the current approach.

Figure 3.8 shows the hub-height wind speed distributions for Kayadüzü wind turbines, again for 2 February 2021 at 17:00 hours. The figure shows the values from SCADA data (black line with symbols) and their overall average value for all turbines (solid black line), which is 8.45 m/s for this scenario. Since individual hub-height velocities can not be directly specified for each turbine in FLORIS simulations, we implement the above described methodology based on virtual reference height calculation, which approximately distributes the overall average wind speed from SCADA data to each turbine in Kayadüzü wind farm. As can be seen from the solid red line, the approximate distribution varies around the SCADA data and local differences do exist. However, the dashed red line, which is the overall average value of the solid red line, shows that it is exactly equal to the overall average of the value obtained from the SCADA data. Therefore, usage of the virtual reference height at least ensures the average hub-height velocity level is the same as the SCADA data in the simulations, even though there are significant hub-height

60

differences between the turbines. If one does not apply to above described methodology, i.e. without the calculation of a virtual reference height, and for example chooses the hub-height of the lowest turbine in the farm, i.e. 80 m, then we get the green distributions in the figure. As is evident both the overall average hub-height wind speed and approximate hub-height wind speed distribution gets significantly overestimated in general.
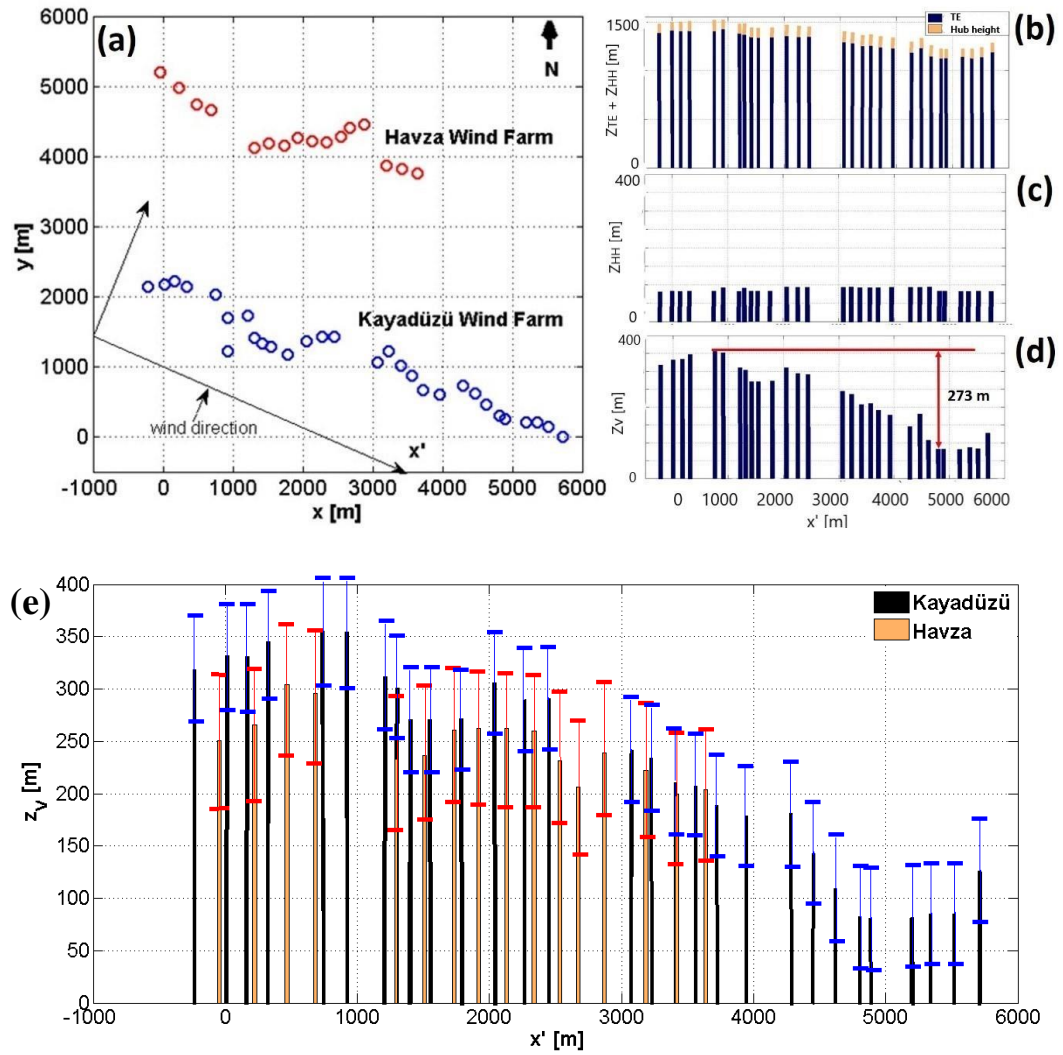
Figure 3.7. (a) Sample wind condition on 2 February 2021 at 17:00 hours - 8.45 m/s wind speed at 202 degrees (based on hourly averages of hub height measurements from SCADA data). For this condition: (b) terrain elevation+hub height distribution for Kayadüzü wind farm, (c) hub height distribution of

Kayadüzü wind turbines if elevation information is removed, (d) virtual hub height distribution to be used in FLORIS simulation for Kayadüzü wind farm, (e) virtual hub height comparisons of the Kayadüzü and Havza wind farms together.
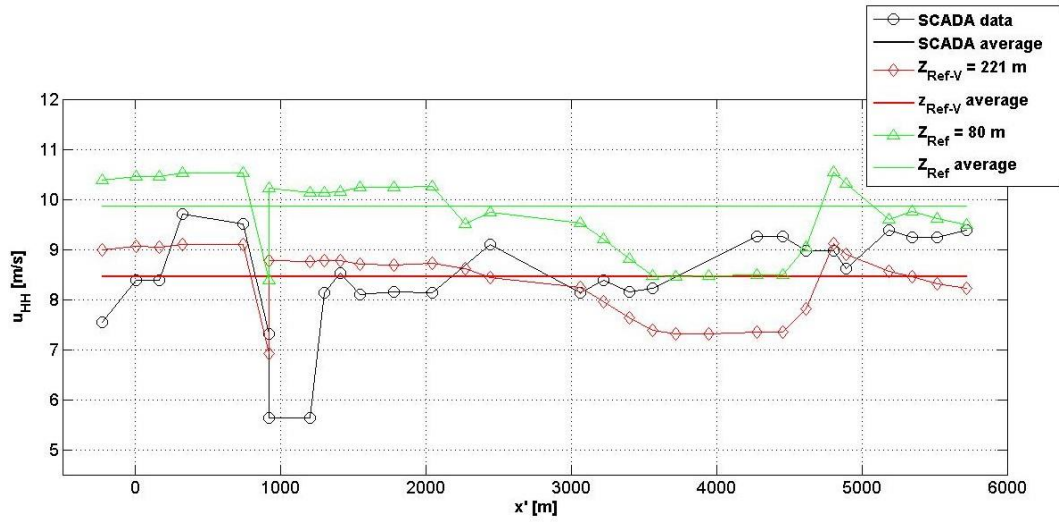
Figure 3.8. Average hub-height wind speed distributions for Kayadüzü wind farm turbines for 2 February 2021 at 17:00 hours.

Some other properties used in the current FLORIS simulations are presented in Table 3.3. Average terrain elevation of the selected wind farms are 1180 m and air density at that altitude is assumed to be 1.09 kg/m^3 [84]. Turbulence intensity of the terrain is obtained from the data provided by the operating companies. Shear coefficient of the terrain is calculated as 0.15 [85].

Table 3.3 Atmospheric properties used in the FLORIS simulations

ρ [kg/m^3]	α	TI
1.09	0.15	0.15

3.3 Baseline Simulation Results with and without Terrain Elevation Model

Using Kayadüzü wind farm's SCADA data for the year 2021, which is available as 10-minute averages, we first calculate hourly average values for wind speed and direction for every turbine in the farm. Then we perform hourly FLORIS simulations for the whole year resulting in 8350 simulations, using the hourly-average inflow conditions from the SCADA data, which is in turn used to generate u_{Ref} and z_{Ref-v} values to be input to FLORIS for every simulation case, as explained in the previous section. The power and thrust coefficient curves for the turbines are also input to FLORIS. In the simulations four different wake models are used to investigate the effect of wake models on AEP predictions for the cases with or without terrain elevation representation: Jensen wake model [18], Multizone wake model [21], Gauss Curl Hybrid model (GCH) [26] and Gaussian wake model [27]. GCH and Gaussian wake models are developed by assuming a Gaussian distribution for the velocity deficit. In the Jensen and Multizone wake models, instead of using the typical Gaussian distribution, the velocity inside the wake is assumed to be constant, as the models' objective is to assess the energy content of the wind flow seen by downstream turbines rather than to properly represent the velocity field.

3.3.1 Simulation Results without Terrain Elevation

In order to investigate the effect of the terrain elevation on AEP predictions, we first performed simulations with no terrain elevation as a baseline case, i.e. all turbines in both wind farms are taken at the same elevation and only variation in hub height is due to the differences in tower heights of existing turbines. Because of the lack of elevation difference, all the wakes generated at Kayadüzü wind farm will get convected downstream and will influence the turbines in Havza wind farm in a similar manner.

Figure 3.9 shows the results of two sample simulations obtained using the GCH wake model and when there is no elevation difference between turbines. Figures 3.9a and

9b are for 2 October 2021 at 19:00 hours and 2 February 2021 at 17:00 hours. As is evident, in certain wind directions the wake interactions between the two wind farms are minimal such as the case presented in Figure 3.9a where the wind direction is 125 degrees. However on other days, such as the one presented in Figure 3.8b where the wind direction is 212 degrees, the Havza wind farm operates completely under the influence of the Kayadüzü wind farm. Similar to the results presented in Figure 3.9, when we examine FLORIS simulations for the whole year and using the annual wind direction distributions from the SCADA data we observe that two wind farms do not interact significantly with each other when the wind directions are between 80 and 135 degrees and between 260 and 315 degrees. The analysis also indicates that the wind farms interact with each other approximately 6800 hours out of 8350 in total in 2021. Therefore, in 82% of the year wake interactions occur for these wind farms. Furthermore, out of the total interaction cases, 79% of the time Havza wind farm operates under the cluster wake influence of Kayadüzü wind farm, similar to the case presented in Figure 3.9b. Keep in mind that simulations are performed for the whole year of 2021 regardless of the fact that there is interaction or not, to obtain the estimated AEP values for the wind farms.

(a)   (b)
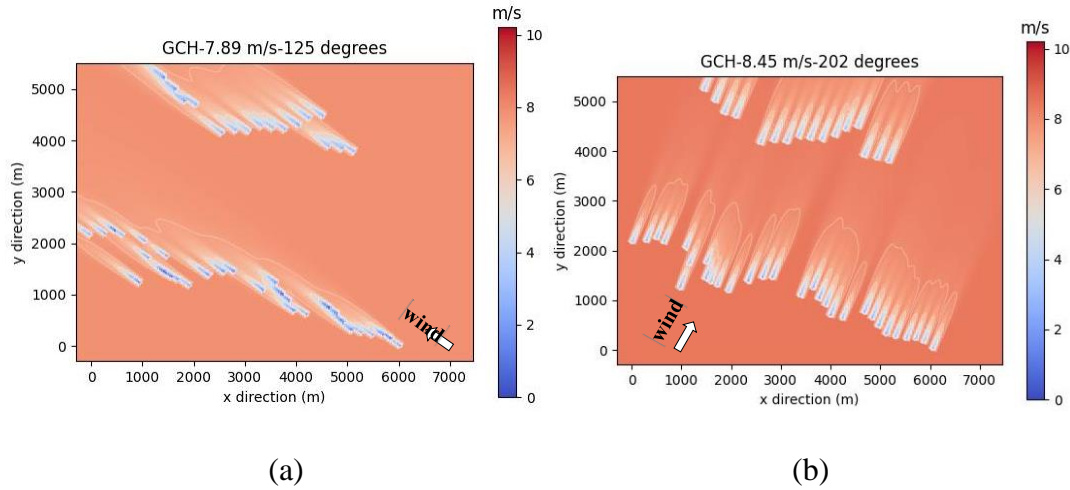
Figure 3.9. Sample FLORIS simulation results using GCH wake model for (a) 7.89 m/s and 125 degrees wind direction on 2 October 2021 at 19:00 hours (b) 8.45 m/s wind speed and 202 degrees wind direction on 2 February 2021 at 17:00 hours. No terrain elevation model.

Figure 3.10 shows a comparison of simulation results, again with no terrain elevation model and for the same date and hour as presented in Figure 3.9b, but now using four different wake models. All wake models predict Havza wind farm operates under the complete cluster wake influence of the Kayadüzü wind farm, albeit to varying degrees depending on the wake model. Jensen and Multizone models (Figures 3.10a and 10b), which are based on constant wake deficit, predict relatively longer wake zones, resulting in reduced hub height velocities for the Havza wind farm in general compared to GCH and Gaussian wake model predictions, which in turn will affect the AEP values. Jensen wake model predicts wider wake zones near Havza wind farm most probably due to higher wake diffusion compared to the Multizone model. Gaussian wake models presented in Figures 3.10c and 10d predict wakes that diffuse more quickly and hence resulting in increased hub height velocity values for the Havza wind farm (see Figure 3.11). In any case, as mentioned before there are minor partial wake-rotor interactions due to the lack of elevation difference (but existing tower height differences only) and Kayadüzü wakes influence the Havza wind turbines in a similar manner for a selected wake model.
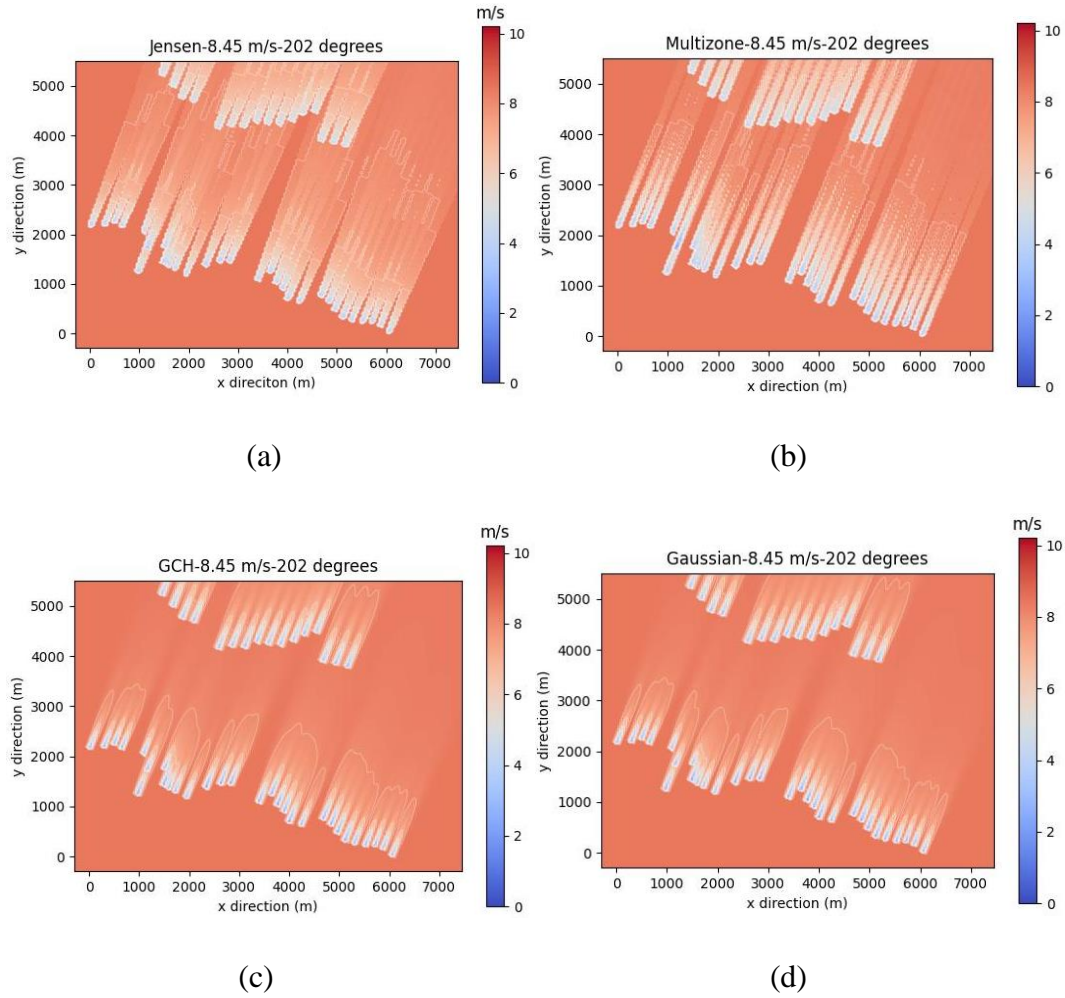
Figure 3.10. Sample simulation results obtained using four different wake models: (a) Jensen (b) Multizone (c) GCH (d) Gaussian for 8.45 m/s wind speed and 202 degrees wind direction. No terrain elevation model. Simulations are for 2 February 2021 at 17:00 hours

In Figure 3.11, hub height velocities of Havza wind farm obtained using four different wake models are presented. Since Jensen wake model generates wider wake zones near Havza wind farm, hub height velocities of the turbines are relatively smaller compared to the levels predicted by other wake models. The wake zone generated by the GCH and Gaussian wake model causes almost the same wind speeds at hub heights of Havza wind farm's turbines. Turbines U32, U37, U41 and

U42 (please refer to Figure 3.2 for turbine positions) are not affected from the wake zones predicted by the Multizone wake model and it is seen that hub height velocities are higher in these turbines (Figures 9b and 10). The same is true for turbine 41 in Jensen wake model (Figures 9a and 10).
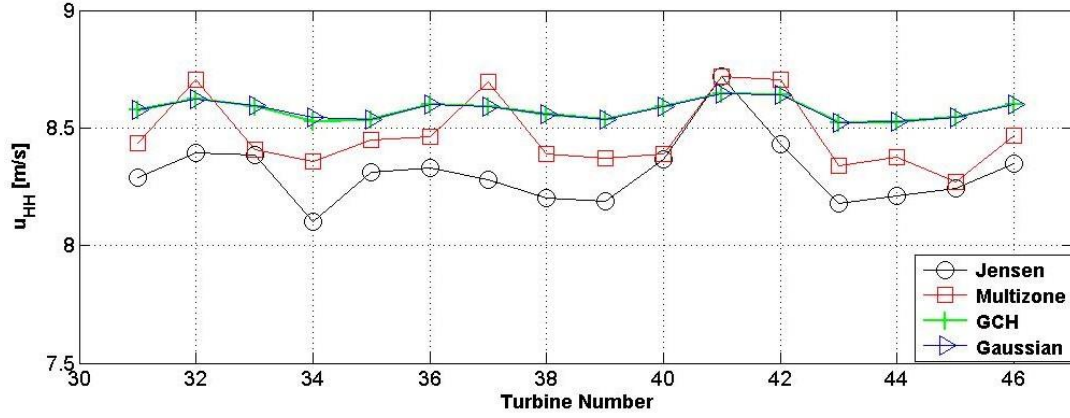
Figure 3.11. Hub height velocities for Havza wind farm obtained using four different wake models for the case presented in Figure 10.

3.3.2   Simulation Results with Terrain Elevation

Using the same hourly simulation methodology described above, FLORIS simulations are performed for the same 8350 cases but now by implementing the terrain elevation representation explained above. Keep in mind that the hub height difference between the turbine with the highest topographic height and the turbine with the lowest is 273 meters. Due to this large topographic height variation, wake effects vary significantly at different heights.

Figure 3.12 shows the wake interactions predicted by GCH wake model for the same conditions given in Figure 3.10, but now on different horizontal planes taken at different virtual hub heights. When the cut plane is taken from the horizontal plane of U1 with virtual hub height of 318 meters, the wakes of the turbines with a relatively low virtual hub height (i.e U16-U24) are barely visible (Figure 3.12a). When the cut plane is at a virtual hub height of 239 meters (turbine U41) (Figure

67

3.12b), this time the wakes of the turbines with higher (U1-U7) and lower virtual hub heights (U19-U24) are not visible. If the cut plane is taken from the horizontal plane of the U20 with virtual hub height of 81 meters, only the wake of turbines with low virtual hub height (U17-U24) can be seen (Figure 3.12d). These results show that variations in wake distributions due to elevation differences are indeed captured with the current approach. Because the topographic heights of the turbines are included in the terrain elevation model, the wakes of different turbine groups are developed at varying heights, as seen in Figure 3.12. When examining the wake of the turbines in the Kayadüzü wind farm, different heights of turbines generate three major wake zones ranging from 270-350 meters (U1-U13 and U125-U26), 150-270 meters (U14-U15 and U27-U30), and 80-150 meters (U16-U24).
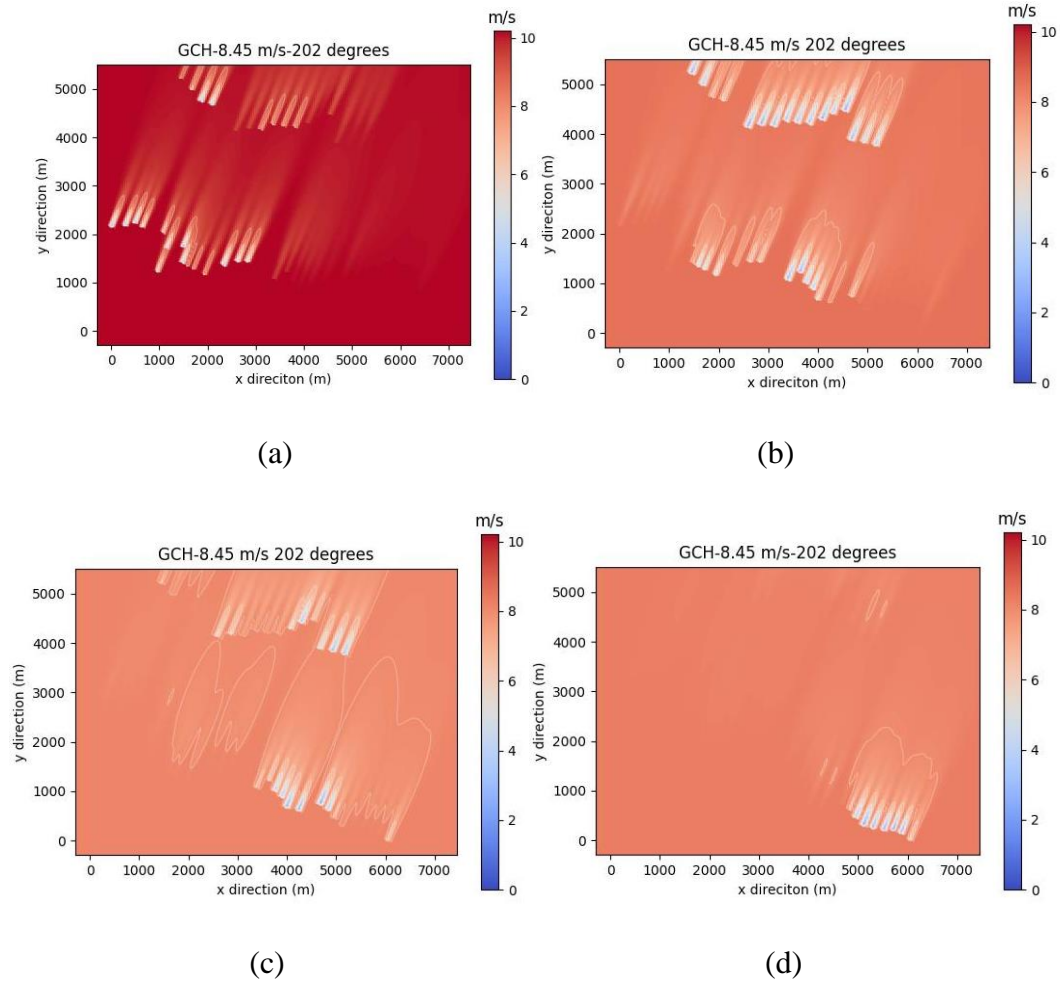
Figure 3.12. Sample FLORIS simulation results using GCH wake model for 8.45 m/s and 202 degrees wind direction on 2 February 2021 at 17:00 hours: (a) on the horizontal plane of the turbine U1 (virtual hub height 318 m) (b) on the horizontal plane of the turbine U41 (virtual hub height 239 m) (c) on the horizontal plane of the turbine U29 (virtual hub height 175 m) and (d) on the horizontal plane of the turbine U20 (virtual hub height 81 m).

Figure 3.13 shows a comparison of hub height velocities of the turbines in Havza wind farm as predicted using the terrain elevation representation and the no terrain elevation baseline cases, for four different wake models. These sample results are again for the same case presented before, i.e. 8.45 m/s and 202 degrees wind direction on 2 February 2021 at 17:00 hours. It can be seen that for the turbines U31-U35 in Havza wind farm there are minor variations in predicted hub height velocities

between the terrain elevation and no terrain elevation cases. For turbines U36-U39 predicted hub height velocities are almost identical and for turbines U40-U45 all wake models predict consistently lower hub height velocities when terrain elevation representation is implemented.

These observed differences can be explained as follows: When no terrain elevation model is used, only differences in hub height levels is due to the varying tower heights of the turbines. For example, tower heights of the turbines in Kayadüzü wind farm are 80 and 91 meters and the tower heights of Havza wind farm turbines are 111 m, as presented previously in Table 3.2. Therefore the hub height differences between Kayadüzü and Havza wind farms change between 20 to 31 meters. However when the terrain elevations are taken into consideration, the virtual hub heights of the turbines U40-U45, which is on average 217 meters, and the virtual hub heights of turbines U14-U15 and U27-U29, the wakes of which affect the turbines U40-U45, are at 215 meters on average. Hence, the hub heights of U14-U15 and U27-U29 turbines at Kayadüzü wind farm and those of U40-U45 in Havza wind farm become very close to each other (i.e 2 m difference in average, which was about 20 m for no terrain elevetion case). Because of this reason, the wakes of Kayadüzü wind farm's turbines (U14-U15 and U27-U29) affect Havza wind farm's U40-U45 turbines more strongly than no terrain elevation model case, causing a significant drop in the hub height velocities of U40-U45 turbines in Havza wind farm. Regarding the turbines U36-U39 of Havza wind farm, which operate under the wake influence of U11-U13 turbines of Kayadüzü wind farm, when no terrain elevation model is implemented, the difference in hub height levels between these turbine groups is 20 meters (again due to tower height differences). When terrain elevation model is implemented, the difference in hub heights is 29 meters. So for these turbine groups implementing the terrain elevation model does not make a major difference in hub height velocity predictions. This is indeed observed for all the cases using different wake models as presented in Figure 3.13. These sample results presented for the specific date and time are mainly given and discussed here to demonstrate the impact of using terrain elevation representation on hub height velocities. The next step will be to check if

these differences observed in hourly simulations will lead to better predictions of AEP for the wind farms in consideration when the entire 8350 hour simulation data is considered for the year 2021. These results are presented in the next section.

(a)

(b)

(c)

(d)
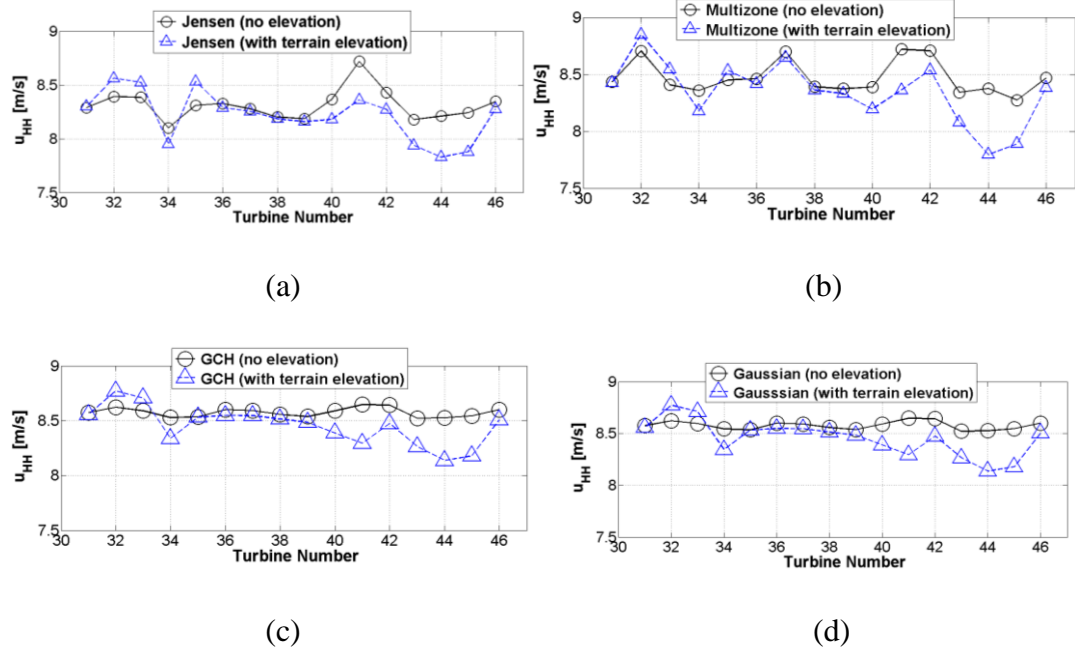
Figure 3.13. Comparison of hub height velocities of Havza wind farm with and without terrain elevation model obtained using (a) Jensen (b) Multizone (c) GCH and (d) Gaussian wake models for 8.45 m/s wind speed and 202 degrees wind direction on 2 February 2021 at 17:00 hours)

3.3.3 Effect of Terrain Elevation Model on AEP predictions – Comparisons with SCADA data

Using the simulation results for the year 2021, we compare the AEP predictions obtained using the *"no terrain elevation"* and *"terrain elevation"* representations with SCADA data in this section. The results are presented in Table 3.4, as percent differences from the SCADA data, calculated using,

$$\frac{AEP_{FLORIS} - AEP_{SCADA}}{AEP_{SCADA}} x100 \qquad (3.7)$$

Table 3.4 Comparison of AEP estimations using FLORIS with SCADA data (using equation 3.7) for the year 2021 for "no terrain elevation (No-TE)" and "terrain elevation (TE)" cases using different wake models

	Kayadüzü		Havza		Total	
	[%]		[%]		[%]	
	No-TE	TE	No-TE	TE	No-TE	TE
Jensen	-7.6	-6.1	24.8	19.8	4.5	3.6
Multizone	-7.6	-6.2	27.5	22.2	5.5	4.4
GCH	-5.1	-3.7	30.7	26.6	8.3	7.6
Gaussian	-4.7	-3.4	31.3	27.0	8.7	7.9

Results presented in Table 3.4 show that, for Kayadüzü wind farm, AEP values are generally underestimated while for Havza wind farm simulations overestimate the AEP values. In terms of total wind farm output, i.e. combining Kayadüzü and Havza estimations, an overprediction can be seen. However for all cases the absolute value of the differences with respect to SCADA data gets reduced when terrain elevation representation is implemented. The closest predictions to SCADA data are obtained using the GCH and Gaussian wake models when the terrain elevation representation is implemented. For Havza wind farm, Jensen model combined with terrain elevation gives the closest estimation, albeit it is significantly worse than the prediction level for the Kayadüzü wind farm. This relatively high level of overestimation for Havza wind farm (though less when terrain elevation is implemented) is most probably due to the prediction of higher hub-height velocities in general from FLORIS

simulations. The terrain elevation representation resolves this to a certain level by allowing partial wake interactions to occur and hence obtaining more realistic hub-height velocities, and hence obtaining AEP results closer to the SCADA data (see Table 3.4 and Figure 3.14). However, of course the influence of the complex terrain topography is still not completely represented, possibly leading to the levels of over and underestimation presented in Table 3.4. The complexity of the terrain topography could create local variations in the in-flow characteristics of a wind turbine, which in turn could modify wake velocity distributions from the ones predicted by the wake models. Therefore the power production characteristics of turbines operating within the wakes of the upstream turbines could be different.

Figure 3.14 shows a comparison of the different wake models with respect to the no-TE and TE representations in terms of AEP prediction differences.

(a)   (b)

(c)   (d)
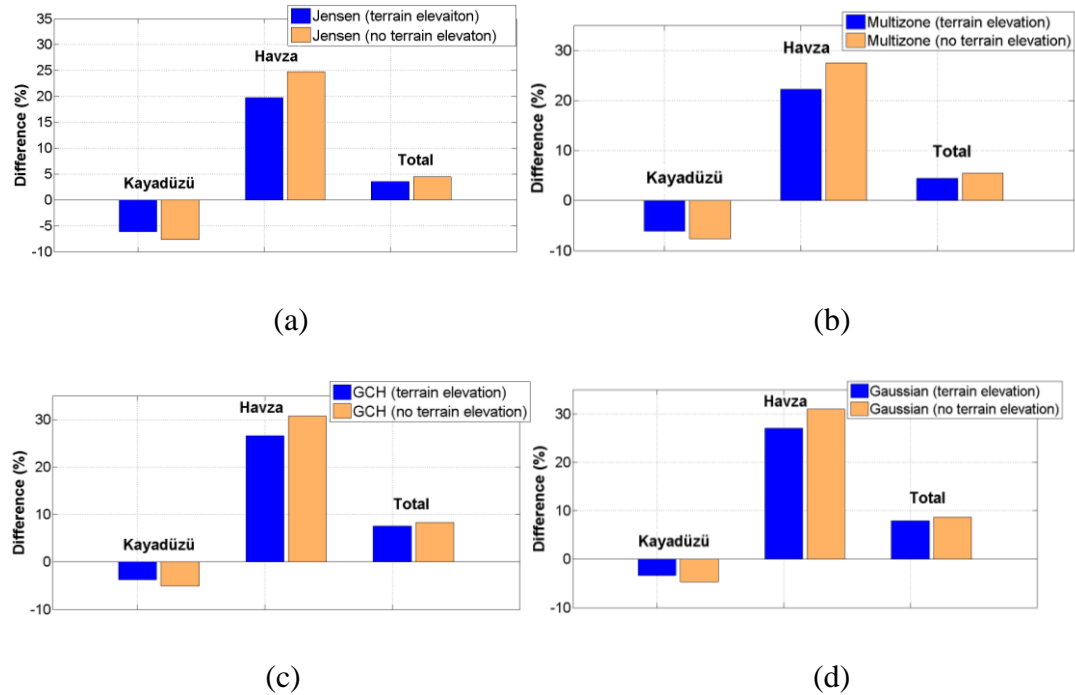
Figure 3.14. Comparison of AEP prediction with SCADA data in *"no terrain elevation"* and *"terrain elevation"* with (a) Jensen, (b) Multizone, (c) GCH and (d) Gaussian wake models

CHAPTER 4

HUB HEIGHT DESIGN OPTIMIZATION

In this section we use the methodology introduced in previous section that allows us to take into account significant elevation differences in FLORIS simulations of cluster-wake type interaction analysis of onshore wind farms, to investigate the effectiveness of deliberate hub height variations on wind farm power performance implemented in these wind farms. The optimization is performed using JMP and based on a systematic procedure that includes introducing definitions of Overall OEC parameters for objective setting, generation of DoE tables and related data through FLORIS simulations to properly cover the design space, Pareto analysis of generated data to find the most influential parameters, generation of response surfaces to represent these variations and Monte-Carlo based simulations to determine optimum hub height distributions.

4.1 Definitions of Overall Evaluation Criteria (OEC) Parameters as Optimization Objectives

The Optimization objective should be determined first in wind farm optimization problems, as described in the literature research. Various optimization objectives, such as maximizing AEP, minimizing LCoE, or limiting noise emission of a wind farm, are included in the optimization objective types. For that reason, we first introduce two different definitions of an OEC parameter to evaluate and compare wind farm performance levels. These are,

$$OEC_1 = \frac{wind\ farm\ power}{wind\ farm\ power\_BL} \qquad (4.1)$$

$$OEC_2 = w_1 x \frac{wind\ farm\ power}{wind\ farm\ power\_BL} + w_2 x \frac{CAPEX\_BL}{CAPEX}$$
$$+ w_3 \frac{OPEX\_BL}{OPEX} \tag{4.2}$$

Here, "wind farm power" is the total wind farm power generated by all turbines for a given simulation time and date. CAPEX is the capital expense related cost parameter but here we only include variations in cost due to changes in hub height levels of the turbines in a given wind farm. According to the cost model proposed by National Renewable Energy Laboratory (NREL) [86] there are three different cost parameters that get affected with a change in the hub height of the turbines: the tower cost, the foundation cost and the assembly and installation cost. These can be calculated using the equations given below as proposed in [86].

$$Tower\ cost = 1.5x[(0.3973\ x\ swept\_area\ x\ hub\_height)$$
$$- 1414] \tag{4.3}$$

$$Foundation\ cost = 303.24x(hub\_height\ x\ swept\_area)^{0.4037} \tag{4.4}$$

$$Assembly\ and\ installation\ cost$$
$$= 1.965x(hub\_height\ x\ rotor\_diameter)^{1.1736} \tag{4.5}$$

and therefore the CAPEX can be calculated as,

$$CAPEX = Tower\ cost + Foundation\ cost$$
$$+ Assembly\ and\ installation\ cost \tag{4.6}$$

Based on NREL's cost model [38], the operation and maintenenace cost, i.e. OPEX, is given directly proportional to Annual Energy Production (AEP) as given below,

$$Operation\ and\ maintanence\ cost = 0.007\ x\ AEP \tag{4.7}$$

Similar to the OPEX model proposed by NREL, in this study we take the OPEX as directly proportional to wind farm power.

The subscript "BL" in equation 9 indicates baseline values when the hub height levels have their unmodified original values as given in Table 2 and w_1, w_2 and w_3 are weighting coefficients, which will be discussed in detail later in this paper. As one can notice, while OEC1 focuses on maximizing the total produced wind power, OEC2 introduces the CAPEX and OPEX related cost parameters based on varying hub heights [86].

Using these OEC definitions we studied four different cases:

Case-1: Finding optimum hub height distribution that maximizes OEC_1, including all turbines in both farms

Case-2: Finding optimum hub height distribution that maximizes OEC_2, including all turbines in both farms

Case-3: Finding optimum hub height distribution that maximizes OEC_1, including only turbines in Havza wind farm

Case-4: Finding optimum hub height distribution that maximizes OEC_2, including only turbines in Havza wind farm

Cases 3 and 4 are selected especially because Havza wind farm operates under the cluster-wake influence of the Kayadüzü wind farm during majority of the time in 2021, as explained previously.

In order to find the optimized hub height distributions for each one of the above-mentioned cases We employed the JMP statistical analysis tool, which is commonly used in Six Sigma, quality control, and engineering, as well as research in science, clinical sciences, engineering, and social sciences [87].

As in the preceding sections, the analysis is performed for 2 February 2021 at 17:00 hours with a wind speed of 8.45 m/s and a direction of 202 degrees. Figure 4.1 shows the wind direction histogram obtained using the SCADA data of the Kayadüzü wind

farm. As can be seen, this wind direction is the most representative wind direction condition during which the Havza wind farm is operating under the influence of the Kayadüzü wind farm. Therefore the optimization study is performed for this most representative wind direction condition.
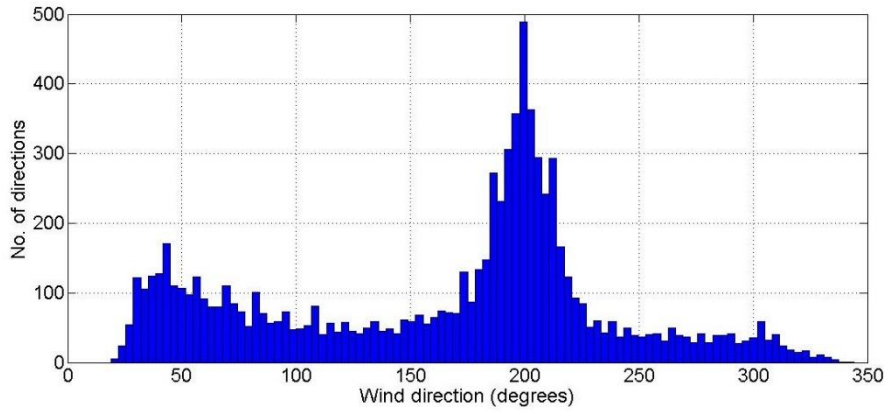
Figure 4.1. Wind direction histogram obtained using the SCADA data from Kayadüzü wind farm for the year 2021

4.2 Generation of Design of Experiments (DoE) Tables and Related Data for Each Case

DoE is a statistical approach concerned with the designing, planning, execution, analysis, and interpretation of the experiments. The purpose of DoE methodology is to assess the influences on the value of a parameter or set of parameters on the experiment. When it's considered that more than one variable component is influencing an experiment, DoE technique can be used. The DoE scheme provides the response of most influential key factors of responses of the measured variable, main effects of the process and least affected variables in a problem setting [88].

As the first section of the this study, we generate DoE tables to analyze the design space for each one of the four cases described above using fractional factorial scheme [92], in which the hub heights of turbines are the design variables. Therefore, for cases 1 and 2 the total number of design variables is 46 (i.e. the total number of turbines including both wind farms) and for cases 3 and 4 it is 16, i.e. the total number

78

of turbines in Havza wind farm only. For each design variable (i.e. hub height) a variation range must be assigned. In this study, a reasonable variation of ±15 m from the baseline hub heights is used, keeping in mind that increasing the hub height would generate an increase in tower costs and decreasing hub heights would reduce the ground clearance of the blades (see Figure 4.2). This range would also influence how much would the downstream turbines be operating partially or fully immersed within the wakes of upstream turbines.
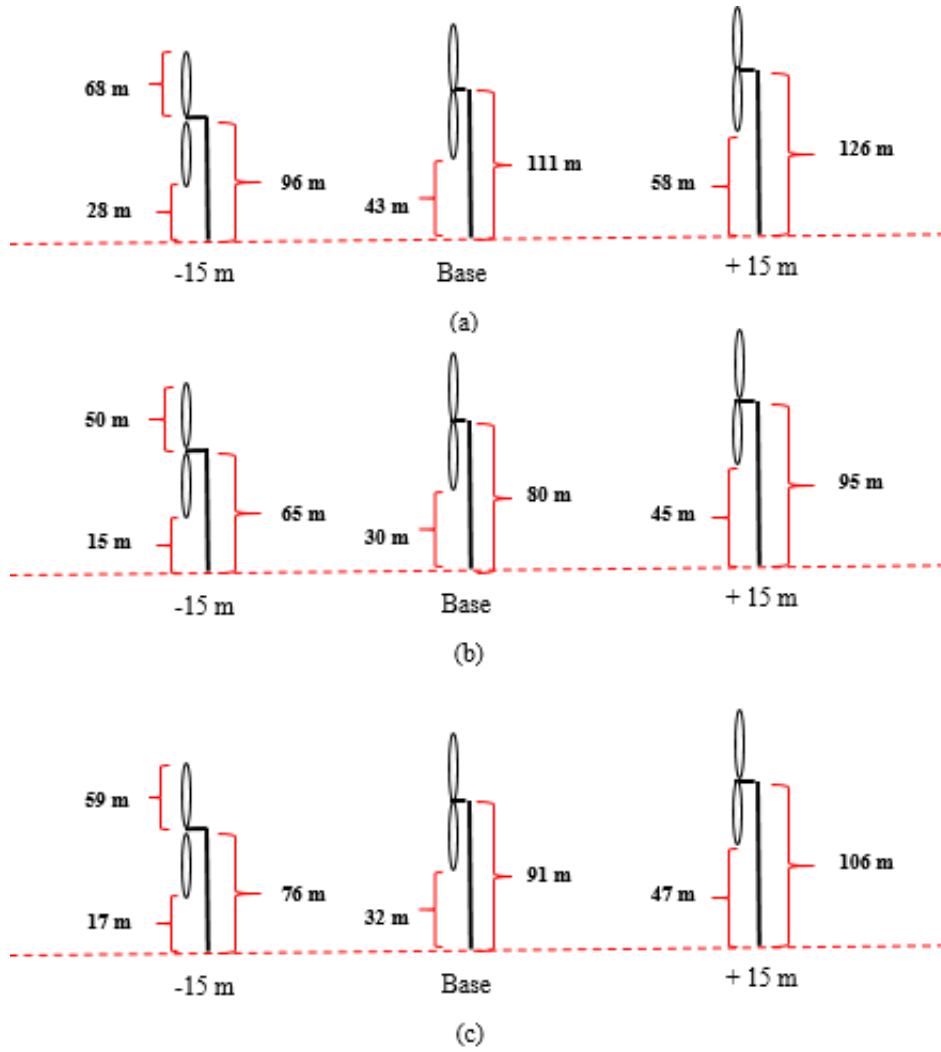
Figure 4.2. Hub height variation in turbines of both wind farms between -+15 meters (a) Havza wind farm's turbines, (b)-(c) Kayadüzü wind farm's turbines

Five sample rows out of 129 rows of the DoE table used for cases 3 and 4 are given in Figure 4.2. The plus and the minus signs under the "pattern" column indicates the applied variation pattern for that row and the corresponding hub heights for each turbine are given to the right (for example a minus for U31 corresponds to the lower boundary of the variation from the baseline hub height, i.e. $111 - 15 = 96$ m). The DoE tables for each case are generated in a similar manner and they consist of 128 variational rows and an additional row for the baseline case, making the total number of rows 129.

To create a DoE table for a screening test we need to go to DoE section and select "Screening Design" button in JMP. We add the number of continuous variables that we are considering. After adding the continuous variables (hub height of the turbines), we click "Continue" button in JMP. As screening type we choose from a list of fractional factorial designs. From the menu opened we choose "Fractional factorial with a resolution 4 with some 2-factor interactions" with no value in the block size column. We add 1 center point so that any quadratic effects could be simulated. Under the drop menu for "Run Order", we select the option "Keep the Same" rather than the default of "Randomize" so that we can always repeat the identical DoE in the future. Once we are done, we select the "Make Table" button. Figure 4.2 presents fiwe sample rows out of 129 rows of the DoE table for case 3 and 4.

	Pattern	U31	U32	U33	U34	U35	U36	U37	U38	U39	U40	U41	U42	U43	U44	U45	U46
1	---------+-++--	96	96	96	96	96	96	96	96	126	96	126	126	126	96	96	96
2	-------++-----+-	96	96	96	96	96	96	126	126	96	96	96	96	126	96	126	96
3	------+-+--+--++	96	96	96	96	96	126	96	126	96	96	126	126	96	96	126	126
4	------++-------+	96	96	96	96	96	126	126	96	126	96	96	96	96	96	96	126
5	-----+--+++-----++	96	96	96	96	126	96	96	126	126	126	96	96	96	96	126	126

Figure 4.3. Five sample rows out of 129 rows of the DoE table used for analyzing the design space for cases 3 and 4

After the generation of the DoE tables, FLORIS simulations with terrain elevation representation are performed for each one of the rows in the tables and the outputs are obtained as OEC_1 or OEC_2 values.

4.3 Analysis of DoE Tables to Determine Proper Weighting Coefficients

Once the DoE tables are generated, the weighting coefficients must be properly determined to obtain a meaningful distribution of the OEC2 value among the 129 cases in the DoE table. Since the OEC2 distribution will later be used to fit a response surface, which is in turn going to be used for the Monte-Carlo simulations for optimization, finding a distribution that will make sense for optimization is critical. As an example, Figure 4.4 shows the OEC2 distributions for all 129 cases in the DoE table considering the variations of CAPEX_BL/CAPEX with respect to Power/PowerBL. Here, each dot in the plots is a case in the DoE table, colored with respect to its corresponding OEC_2 value. When all weighting coefficients are selected as 1 (Figure 4.4a), the OEC_2 distribution in the DoE table shows that the majority of the cases with the highest OEC_2 values are mainly clustered in the top left quadrant, which corresponds to a decrease in both power and CAPEX levels with respect to the baseline. This case would not be very preferrable in terms of optimization objective due to a decrease in power levels, instead, one would expect to have an OEC2 distribution that would have the highest values mostly in the top right quadrant, where power levels increase and CAPEX levels decrease with respect to the baseline. This case is presented in Figure 4.4b, where the weighting coefficient for power, w_1, is increased to 7, while w_2 and w_3 are kept at 1. As is evident, the majority of the cases with the highest OEC_2 values are now clustered more in the top right quadrant with some cases existing in the bottom right quadrant. As illustrated by this example, choosing $w_1=7$, $w_2=1$, $w_3=1$ for OEC_2 calculations and then fitting a response surface to these variations to be used in the Monte-Carlo simulations will lead to an optimization that would generate hub height distributions that will try to increase power while either decreasing or keeping the CAPEX change minimal. The conclusion is, depending on the required objective of the optimization an analysis of the DoE tables must be performed such as the one presented here to determine proper weighting coefficients. Keep in mind that both the CAPEX and OPEX models are relatively simplistic here and are based on the NREL cost model. More realistic

models can be implemented into the methodology whenever they are available. In the following sections we present our optimization results with weighting coefficients selected as $w_1=7$, $w_2=1$, $w_3=1$.

(a) (b)
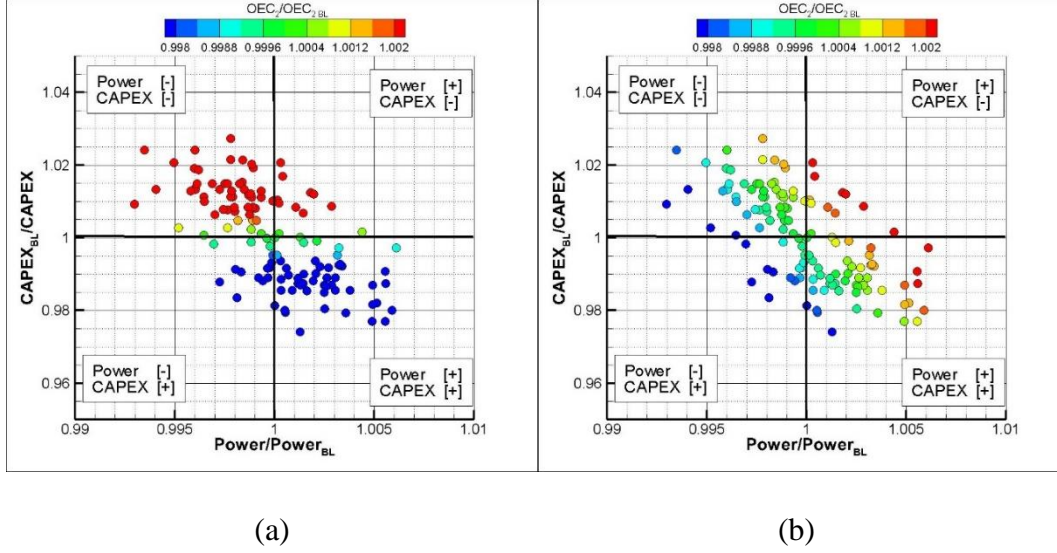
Figure 4.4. Sample OEC2 distributions for the 129 cases in the DoE table for (a) $w_1=1$, $w_2=1$, $w_3=1$ and (b) $w_1=7$, $w_2=1$, $w_3=1$. "[+]" and "[-]" symbols for power and CAPEX in the four quadrants indicate an increase or decrease, respectively, with respect to the baseline case.

4.4 Analysis of Generated Data to Find The Most Influential Parameters

After the OEC data is generated through FLORIS simulations for each one of the investigated rows in the DoE tables, a Pareto analysis is performed to determine which design variables (i.e. which turbines' tower height variations) are the most influential in affecting the OEC outputs. In other words, this analysis helps us to understand the sensitivity of the OEC values to the hub height variation of each individual turbine included in the design process. A Pareto Analysis, which yields a Pareto plot, can be used to perform this. According to the Pareto Principle, 20% of the factors are responsible for 80% of the variability in a response [89].

The effectiveness of various variables (i.e. turbine height), was investigated using most effective variables of the Pareto analysis, and it was determined how many

82

variables the system fit best. The statistical analysis methodology R-squared was used to determine how many variables the system began to fit. R-squared demonstrates how closely the data fit the JMP regression model. In the analysis for case-2, as the number of inputs increases, the R-squared value approaches 1, indicating that the input is beginning to fit more closely with the JMP regression model (see Figure 4.5). RSE has been fitted according to 8 inputs in all cases since it has been found that the R-squared value of the regression model is significantly close to 1 according to 8 input (i.e. 8 most influential parameters based on the pareto analysis) values, or in other words, that the system fits better.
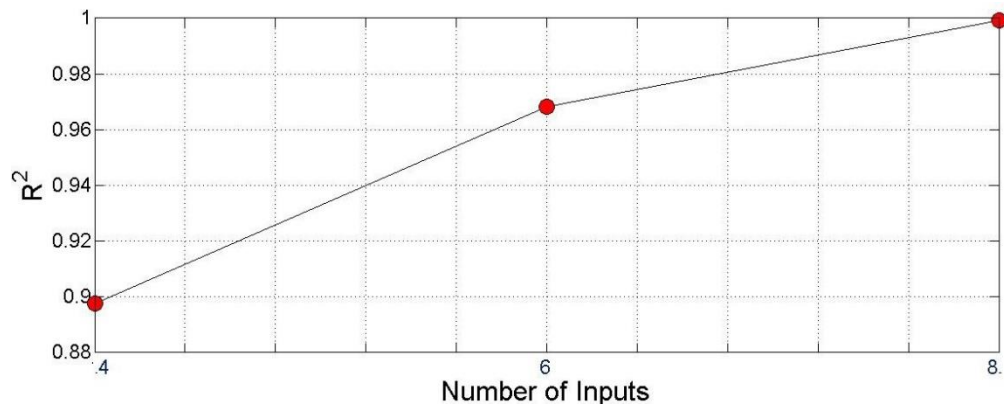
Figure 4.5. R-squared results of the different inputs for case-2

Figure 4.6 shows the Pareto plots obtained for each one of the four cases defined previously for the most influential 8 parameters. The individual influence of each design variable is quantified using t-ratio, which is a statistical parameter for determining the significance level of a parameter estimate. The t-ratio values in Figure 4.6 are presented as normalized with respect to the max. t-ratio value in each case.
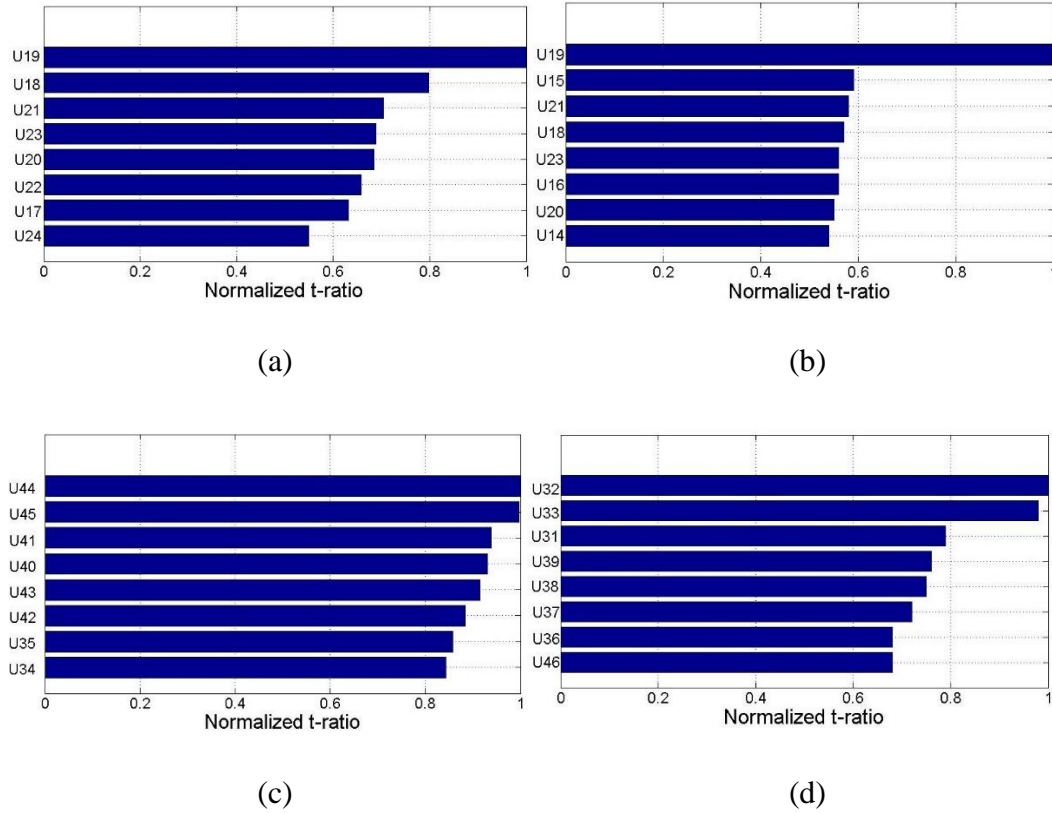
Figure 4.6. Results of Pareto analysis for the four investigated cases: (a) Case 1 (b) Case 2 (c) Case 3 and (d) Case 4

The results of the Pareto analysis presented in Figure 4.6 are discussed below separately for each case:

Case 1 (Total wind farm optimization with OEC_1, Figure 4.6a): In this case, all of the most influential turbines in terms of OEC_1 are the turbines towards the eastern end of the Kayadüzü wind farm, the wakes of which do not in fact affect the Havza wind farm (see Figures 3.2 and 3.7e). Because OEC_1 only focuses on maximizing the total wind power, the easiest way to increase the total farm is to increase the hub height of the turbines that do not have wake interaction with each other. When the hub height increases, the farm power of Kayadüzü increases according to the power law, while the farm power of Havza is not adversely affected since there is no wake interaction with the turbines in Havza wind farm.

84

Case 2 (Total wind farm optimization with OEC$_2$, Figure 4.6b): Similar to Case 1, all of the most influential turbines, now in terms of OEC$_2$, are the turbines in Kayadüzü wind farm. However unlike the results for Case 1, the most influential turbines, the tower height variation of which is impacting the OEC$_2$ the most, are not the ones towards the eastern end of the farm but other turbines such as U14 and U15 seem to have a strong influence as well. Since OEC$_2$ introduces a cost related parameter, wind farm optimization aims to optimize between wake effects, rather than just focusing on increasing the tower heights.

Case 3 (Havza wind farm optimization with OEC$_1$, Figure 4.6c): The Pareto analysis for this case show that the most influential turbines for OEC$_1$ are either under partial influence of the cluster-wake effects of the Kayadüzü wind farm (U34, U35, U40, U41 and U42) or the ones operating under more strong wake effects (U43, U44 and U45) (see Figures 3.2 and 3.7e).

Case 4 (Havza wind farm optimization with OEC$_2$, Figure 4.6d): Regarding the Pareto analysis for Case 4, i.e. considering OEC$_2$ which now includes a cost related term, different turbines turn out to be more influential compared to Case 3, again some of them partially (i.e. U31, U32, U33, U38 and U39) and some of them more strongly (i.e. U36, U37 and U46) get affected from the cluster-wake of the Kayadüzü wind farm (see Figures 3.2 and 3.7e).

4.5   Response Surface Equations (RSE) and RSE Prediction Performance

After the Pareto analysis is completed, Response Surface Equations (RSE) are obtained for the OEC variations of the determined most influential design parameters. As a result, the need for investigating all possible hub height variations of all turbines is prevented and only the most influential turbines in terms of hub height variations are included in the optimization. RSE is a set of mathematical and statistical approaches that may be used to simulate and optimize stochastic models. For representing a curved parabolic surface to continuous variables, response surface

designs are helpful [88]. In this analysis we used second order response surface design given by,

$$RSE = b_0 + \sum_{i=1}^{k} b_i\, x_i + \sum_{i=1}^{k} b_{ii}x_i{}^2 + \sum_{i=1}^{k-1} \sum_{j=i+1}^{k} b_{ji}x_i\, x_j \qquad (4.3)$$

where b_i are the regression coefficients for the linear terms, b_{ii} are the coefficients for pure quadratic terms, b_{ji} are coefficients for cross-product terms (second order interactions) and x_i, x_j are the design variables. Here, $x_i x_j$ denotes interactions between two design variables.

After identifying the most influential 8 variables that contributes to our OECs, Response Surface Design tab from the DoE menu is selected in JMP. For all cases investigated in this study, Central Composite Design (CCD) second-order response surfaces are used. The CCD, as shown in Figure 4.7, is one of the popular response surface design. To estimate the curvature of the surface, it uses a two-level fractional factorial points and two different types of points. A set of axial points (also known as star points) and a center point consist of the two distinct points in CCD design [90].
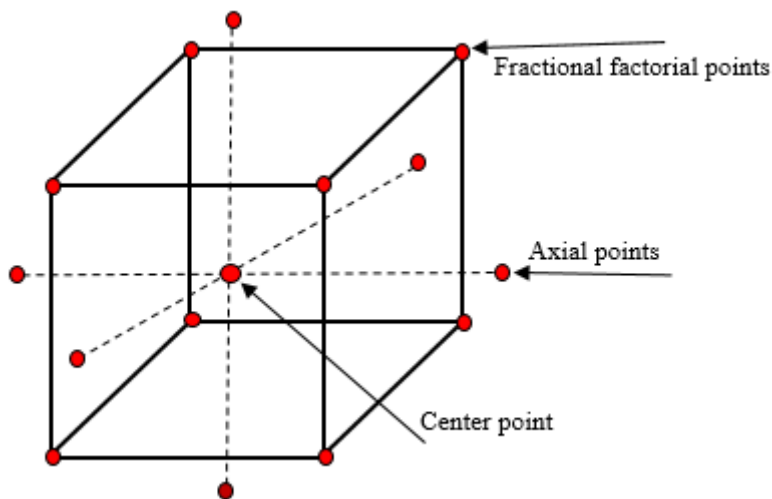
Figure 4.7. Central Composite Design scheme

86

The response surface equations obtained for four different cases using the CCD are provided in appendices.

In order to check the prediction performance of the response surfaces, actual vs. predicted plots are presented in Figure 4.8. While actual values in OECs are actual results based on the FLORIS simulations and tower height distributions, predicted values represent the response surface predictions for those cases. Each red dot on the plots is practically on the diagonal line, which shows that the generated response surfaces prediction performance is reasonably well.

(a)   (b)

(c)   (d)
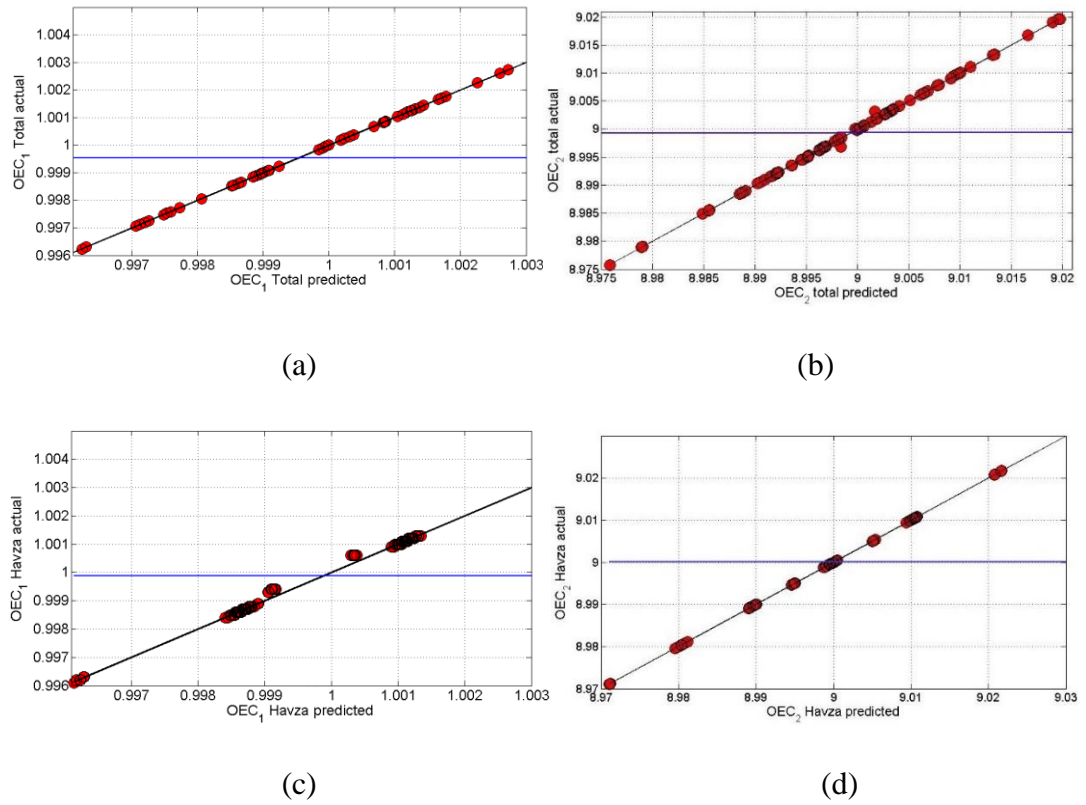
Figure 4.8. Actual vs predicted plots for (a) Case 1 (b) Case 2 (c) Case 3 (d) Case 4

4.6   Monte-Carlo Simulations to Find Optimized Hub Height Distributions

The obtained response surfaces are now used for Monte-Carlo based simulations for obtaining the optimized hub height layout separately for each case, that is giving the maximum OEC value. Since the computation of the validated response surfaces is relatively much faster than obtaining FLORIS simulation results we could perform hundreds of thousands of simulations relatively quickly. For this purpose we performed Monte-Carlo based simulations for each one of the cases. The maximum OEC value is determined after a convergence is achieved for the simulations. The convergence plots are given in Figure 4.9 below for all cases. As can be seen, convergence is achieved after about 2×10^6 simulations for these cases.
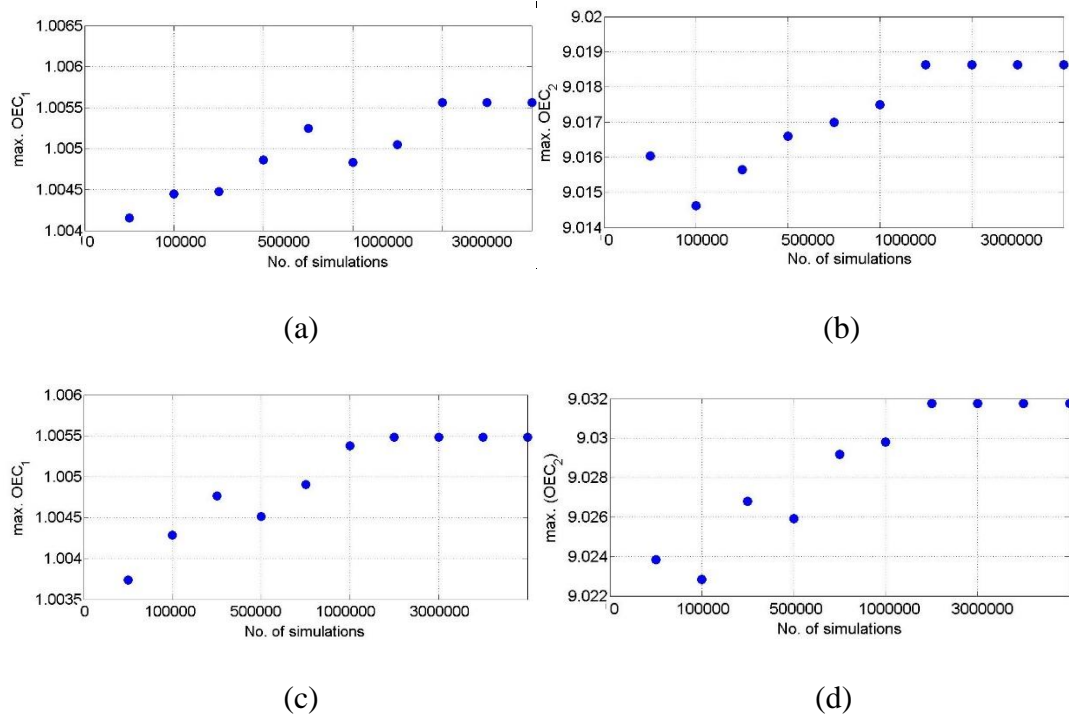
Figure 4.9. Convergence of the OECs for different JMP simulations (a) Case 1 (b) Case 2 (c) Case 3 (d) Case 4

According to the simulation results, the hub height distributions giving the maximum converged OEC values are listed for each case separately in Tables 4.1 through 4.4.

Table 4.1 Optimization results for Case 1 (Total wind farm optimization with OEC_1)

Turbine No.	Hub height baseline [m]	Hub height optimized [m]	Change in hub height [m]
U19	80	94	+14
U18	91	104	+13
U21	80	84	+4
U23	80	91	+11
U20	80	93	+13
U22	80	93	+13
U17	91	105	+14
U24	80	94	+14
Total hub height change [m]			**+96**
Total Hub Height	**Baseline [m]**	**Optimized [m]**	**Change (%)**
	4330	4426	2.22
CAPEX	**Baseline ($)**	**Optimized ($)**	**Difference ($)**
	38,326,192	38,967,635	641,443 (1.67% increase)
Farm Power	**Baseline [MW]**	**Optimized [MW]**	**Change (%)**
	70.871	71.266	0.56
AEP	**Baseline [kWh]**	**Optimized [kWh]**	**Difference [kWh]**
	428,587,510	430,589,437	2,001,927 (0.47% increase)

Table 4.2 Optimization results for Case 2 (Total wind farm optimization with OEC$_2$)

Turbine No.	Hub height baseline [m]	Hub height optimized [m]	Change in hub height [m]
U19	80	95	+15
U15	91	85	-6
U21	80	85	+5
U18	91	104	+13
U23	80	91	+11
U16	91	77	-14
U20	80	88	+8
U14	91	82	-9
		Total tower height change [m]	**23**
Total Hub Height	**Baseline [m]**	**Optimized [m]**	**Change (%)**
	4330	4353	0.53
CAPEX	**Baseline ($)**	**Optimized ($)**	**Difference ($)**
	38,326,192	38,435,538	109,346 (0.28% increase)
Farm Power	**Baseline [MW]**	**Optimized [MW]**	**Change (%)**
	70.871	71.154	0.40
AEP	**Baseline [kWh]**	**Optimized [kWh]**	**Difference [kWh]**
	428,587,510	429,513,638	926,128 (0.22% increase)

Table 4.3 Optimization results for Case 3 (Havza wind farm optimization with OEC_1)

Turbine No.	Hub height baseline [m]	Hub height optimized [m]	Change in hub height [m]
U44	111	126	+15
U45	111	115	+14
U41	111	118	+7
U40	111	120	+9
U43	111	123	+12
U42	111	126	+15
U35	111	124	+13
U34	111	122	+11
Total tower height change [m]			**+96**

Total Hub Height	Baseline [m]	Optimized [m]	Change (%)
	4330	4426	2.22
CAPEX	**Baseline ($)**	**Optimized ($)**	**Difference ($)**
	38,326,192	39,244,840	918,648 (2.40% increase)
Farm Power	**Baseline [MW]**	**Optimized [MW]**	**Change (%)**
	70.871	71.225	0.50
AEP	**Baseline [kWh]**	**Optimized [kWh]**	**Difference [kWh]**
	428,587,510	429,501,039	913,529 (0.21% increase)

Table 4.4 Optimization results for Case 4 (Havza wind farm optimization with OEC_2)

Turbine No.	Hub height baseline [m]	Hub height optimized [m]	Change in hub height [m]
U32	111	100	-11
U33	111	109	-2
U31	111	96	-15
U39	111	101	-10
U38	111	98	-13
U37	111	102	-9
U36	111	98	-13
U46	111	98	-13
Total tower height change [m]			**-86**
Total Hub Height	**Baseline [m]**	**Optimized [m]**	**Change (%)**
	4330	4244	-1.99
CAPEX	**Baseline ($)**	**Optimized ($)**	**Difference ($)**
	38,326,192	37,408,904	-917,288 (-2.39% decrease)
Farm Power	**Baseline [MW]**	**Optimized [MW]**	**Change (%)**
	70.871	70.656	-0.30
AEP	**Baseline [kWh]**	**Optimized [kWh]**	**Difference [kWh]**
	428,587,510	427,583,776	-1,003,734 (-0.23% decrease)

As previously stated, OEC_1 aims to maximize farm power regardless of hub height, while OEC_2 attempts to maximize farm power the farm power while trying to reduce CAPEX and OPEX levels.

For Case 1 (Table 4.1), the tower heights of all eight turbines increased when both wind farms were included in the optimization using OEC1. Since with this definition of OEC cost is not considered, the hub heights of the most influential turbines, which are to the east end of the Kayadüzü wind farm and the wakes of which are not influencing the Havza wind farm turbines, are increased to higher levels in order to benefit from the increased wind speeds. As a result, the farm power increased by 0.56%, while the total tower height is also increased by 96 meters, i.e. 2.22% increase from the original total tower height corresponding to a 1.67% increase from the original CAPEX. FLORIS analysis for this optimized configuration also shows a 0.47% increase in the AEP level.

Here, the total farm power (i.e. combined power of both wind farms) increased by 0.4 %, corresponding to more than 920,000 kWh increase in total AEP level estimated by the FLORIS simulation of the optimized hub height distribution, while CAPEX is increased by 0.28% (see Table 4.2). The hub heights of the three turbines (i.e. U14, U15, U16) interacting with Havza wind farm decreased, while the hub heights of the five turbines (i.e. U18, U19, U20, U21 and U23) not interacting with Havza wind farm increased. Note that the wind turbines at Kayadüzü wind farm whose hub heights decrease basically produce less power due to the reduction in hub height velocities calculated from the power law relation. However this is compensated in the optimization results through two effects: The first one is due to the reduced wake effects at the Havza wind farm and the second one is due to the increased hub heights of the wind turbines at Kayadüzü wind farm that actually do not interact with the Havza wind farm (i.e. U18, U19, U20, U21 and U23).

As indicated before, Cases 3 and 4 are studied to investigate the impact of hub height variations only in Havza wind farm, because of the fact that Havza wind farm is the one that operates under the influence of the Kayadüzü wind farm most of the year.

In these studies Kayadüzü wind turbines are not included in the design optimization process. When OEC1 is selected as the objective (Case 3, Table 4.3), we see that the farm power increased by 0.50% while sum of the tower height increased by 96 meters in total i.e. 2.22% increase, corresponding to a 2.4% increase in CAPEX. A 0.21 % increase in AEP is obtained with this optimized configuration based on the FLORIS simulations of the optimized hub height distribution. Similar to Case 1, the tower heights are all increased in this case.

Regarding the results presented in Table 4.4 for Case 4 interesting results are obtained. Case 4 is a much more challenging scenario than the other cases in general. Because enhancing the farm power output while decreasing the CAPEX of Havza wind farm, while keeping the hub heights of the Kayadüzü wind farm fixed considerably reduces the degree of freedom for the optimization method. In this case when Havza wind farm hub heights are optimized based on OEC2 the total farm power gets decreased by 0.3%, while sum of the tower heights gets also decreased by 86 meters resulting in a 2.39% decrease in CAPEX. Here we see that the tower heights of the turbines interacting strongly with Kayadüzü wind farm are reduced and the optimization nearly maintains the original farm power output while achieving a significant reduction in CAPEX. When the power output level is not constrained to be always positive such optimization results can be obtained with the current methdology and this also shows that a different set of weighting coefficients might be needed for this optimization case. Figure 4.9 shows a visual comparison of the baseline and optimized hub height distributions for all cases investigated in this study. Turbine coordinates in Figure 4.10 are along the x' axis as in Figure 3.7e.
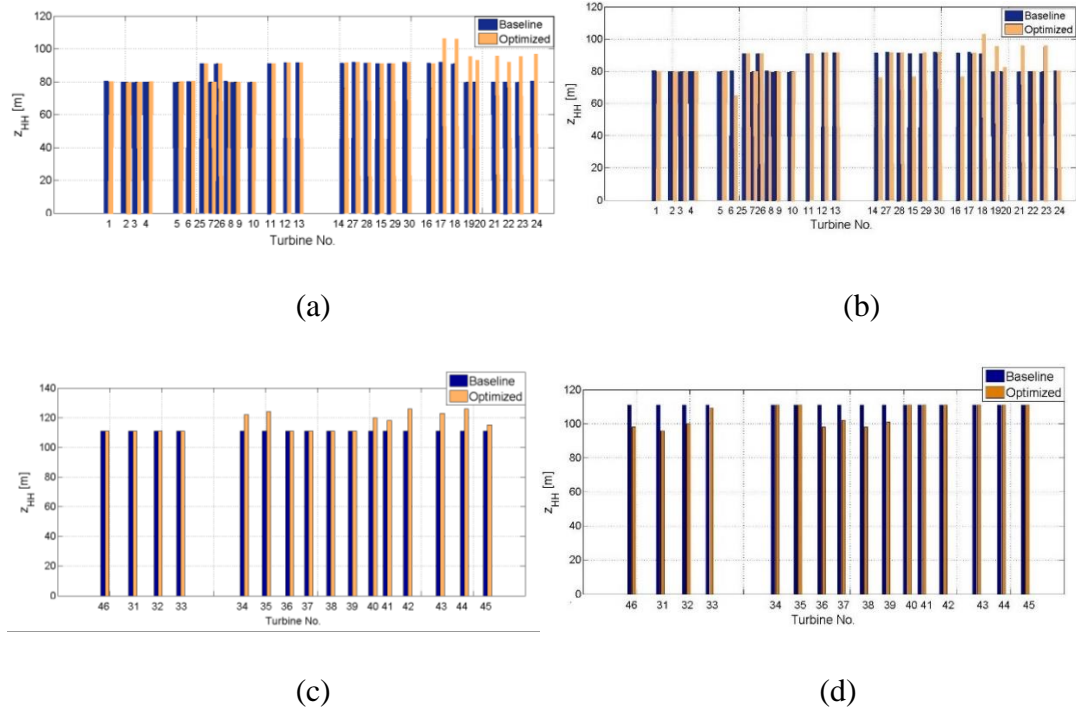
Figure 4.10. Comparison of baseline and optimized hub heights of the 8 most influential (in terms of OEC definitions) turbines (a) Case 1 (b) Case 2 (c) Case 3 (d) Case 4

CHAPTER 5

CONCLUSIONS

In this study, the results of an investigation that focuses on finding the optimum hub height distributions for two interacting real on-shore wind farms that are located on relatively complex terrain with significant elevation differences between turbines are presented. One of the wind farms operates under the cluster-wake influence of the other farm majority of the time. Four different optimization scenarios are studied based on two different definitions of objective functions, which takes into account both the power production capacity and the relevant cost variations due to changing hub heights. The study is based on simulations performed using the FLORIS framework.

In the first part of this study, Inter-farm cluster wake interactions between two on-shore wind farms that are in close proximity of each other is investigated using FLORIS framework. Investigated on-shore wind farms are located on relatively complex terrain. This is modeled through an easy to implement terrain elevation representation that takes into account relative hub height and rotor overlap positions while using realistic estimates (i.e. consistent with SCADA data) for hub height velocity levels despite potentially large differences in hub heights of the wind turbines. Simulations are performed with and without terrain elevation representation using four different wake models that are available in FLORIS (i.e. Jensen, Multizone, GCH and Gaussian) and the variations in velocity fields are compared. Results show that partial wake interactions that occur at different elevations are captured as expected, which lead to more realistic representation of hub height velocities for the downstream wind farm that is operating within the cluster wake of the upstream wind farm. Comparisons of FLORIS predicted AEP

levels with SCADA data for the entire year of 2021 show closer agreement to SCADA data when terrain elevation representation is implemented.

In the second part of the study, the impact of optimizing the hub-height distributions for two interacting on-shore wind farms is investigated. The optimizations are performed using different definitions of objective functions both with and without considering cost increases related to tower height changes. The optimizations are performed using Monte-Carlo simulations that utilize response surfaces generated through a systematic analysis of the design space, which includes creation of Design of Experiments tables, generation of relevant databases using FLORIS simulations and Pareto analysis. Because of significant elevation differences between turbines due to the complex terrain, the terrain elevation representation is also implemented in FLORIS to obtain a more realistic representation of partial wake interactions that are occurring between the two wind farms.

When both wind farms are included in the optimization process, the most influential wind turbines that are affecting the defined objective functions turned out to be always from the upstream wind farm. If the cost related tower height parameter is not included in the objective function definition, the optimization process tends towards increasing the hub height levels of the turbines in the upstream wind farm to benefit from increased wind speeds at higher hub heights. However, when the cost related tower height is included, the optimization both tries to reduce wake interaction effects while increasing hub heights of the turbines that are not interacting with the downstream wind farm.

When only the downstream wind farm is included in the optimization process but if the cost related tower height is not included in the objective function definition, the optimized results show that hub heights of all of the most influential turbines get increased. However when the cost related tower height is included, the optimized results show that the hub heights of the partially interacting turbines get decreased and those that are operating under stronger cluster-wake effects get increased.

Overall, the optimized results most of the time show a reasonable increase in wind farm power output levels. While doing this, inclusion of a cost parameter results in total tower height levels either not changing or for some cases even getting reduced for the wind farms in consideration and hence preventing significant increases in cost levels due to potential increases in hub heights.

As the future work studies, two significant points can be proposed. Although the terrain elevation of the turbines is implemented into the FLORIS as the *"terrain elevation methodology"* to properly represent the interaction of the cluster wake of the wind farms, the influence of the complex terrain topography is still not completely represented, possibly leading to the levels of over and underestimation presented in Table 3.4. The optimum hub height optimization distribution was achieved using DoE and response surface equation-based advanced statistical approaches. For hub height distribution optimization, approaches such as artificial intelligence-based genetic algorithms can be used. Another future study within the scope of the thesis study can be recommended as a wake analysis about what the minimum separation should be between these two onshore wind farms.

REFERENCES

[1]   GWEC, "Global Wind Energy Report 2021," Hamburg, Mar. 2021.

[2]   IEA, "https://www.iea.org/data-and-statistics/data-browser?country=WORLD&fuel=Energy%20supply&indicator=RenewGen BySource," Oct. 29, 2021. .

[3]   EMRA, "Electricity Market Generation Licenece," *http://lisans.epdk.gov.tr/epvys-web/faces/pages/lisans/elektrikUretim/elektrikUretimOzetSorgula.xhtml*, Oct. 31, 2021. .

[4]   ESMAP, "Expanding Offshore Wind to Expanding Markets," Washington, Oct. 2019.

[5]   J. Serrano González, M. Burgos Payán, J. M. R. Santos, and F. González-Longatt, "A review and recent developments in the optimal wind-turbine micro-siting problem," *Renewable and Sustainable Energy Reviews*, vol. 30. pp. 133–144, 2014, doi: 10.1016/j.rser.2013.09.027.

[6]   R. J. Barthelmie and Danmarks Tekniske Universitet. Risø DTU, *Flow and wakes in large wind farm : final report for UpWind WP8*. Risø DTU - National Laboratory for Sustainable Energy, 2011.

[7]   T. Göçmen, P. Van Der Laan, P. E. Réthoré, A. P. Diaz, G. C. Larsen, and S. Ott, "Wind turbine wake models developed at the technical university of Denmark: A review," *Renewable and Sustainable Energy Reviews*, vol. 60. Elsevier Ltd, pp. 752–769, Jul. 01, 2016, doi: 10.1016/j.rser.2016.01.113.

[8]   F. Porté-Agel, M. Bastankhah, and S. Shamsoddin, "Wind-Turbine and Wind-Farm Flows: A Review," *Boundary-Layer Meteorol.*, vol. 174, no. 1, pp. 1–59, Jan. 2020, doi: 10.1007/s10546-019-00473-0.

[9]   L. J. Vermeer, J. N. Sørensen, and A. Crespo, "Wind turbine wake aerodynamics," *Progress in Aerospace Sciences*, vol. 39, no. 6–7. Elsevier

Ltd, pp. 467–510, 2003, doi: 10.1016/S0376-0421(03)00078-2.

[10]   A. Crespo, J. Hernandez, and S. Frandsen, "Survey of Modelling Methodsfor Wind Turbine Wakes andWind Farms," *Wind Energy*, vol. 2, pp. 1–24, 1999.

[11]   P. B. S. Lissaman, "Energy Effectiviness of Arbitrary Arrays of Wind Turbines," *J. energy*, vol. 3, no. 6, pp. 323–328, 1979, doi: 10.2514/3.62441.

[12]   N. Panossian, T. Herges, and D. Maniaci, "Wind Turbine Wake Definition and Identification Using Velocity Deficit and Turbulence Profile."

[13]   P.A. Taylor, "On Wake Decay and Row Spacing for WECS Farms," in *Int. Symp. on Wind Energy Systems*, 1980, pp. 451–468.

[14]   M. K. Liu, M. A. Yocke, and T. C. Myers, "Mathematical Model for the Analysis of Wind-Turbie Wakes," *J. energy*, vol. 7, no. 1, pp. 73–78, 1983, doi: 10.2514/3.48065.

[15]   J.F. Ainsile, "Development of an eddy viscosity model for wind turbine wakes," in *Proc. 7th BWEA Wind Energy Conf.*, 1985, pp. 61–66.

[16]   A. Crespo, F. Manuel, and J. Hernandez, "Numerical modelling of wind turbine wakes," in *Proc. 1990 EuropeanCommunity Wind Energy Conf.*, 1990, pp. 166–170.

[17]   P.E.J. Vermeulen, "An experimental analysis of wind turbine wakes," in *Proc. 3rd Int. Symp. on Wind Energy Systems*, 1980, pp. 431–450.

[18]   N. O. Jensen, *A note on wind generator interaction*. Risø National Laboratory, 1983.

[19]   I. ; Katic, J. ; Højstrup, and N. O. Jensen, "A Simple Model for Cluster Efficiency," APA, 1987.

[20]   S. Frandsen *et al.*, "Analytical modelling of wind speed deficit in large offshore wind farms," in *Wind Energy*, 2006, vol. 9, no. 1–2, pp. 39–53, doi:

10.1002/we.189.

[21] P. M. O. Gebraad and J. W. Van Wingerden, "A control-oriented dynamic model for wakes in wind plants," in *Journal of Physics: Conference Series*, 2014, vol. 524, no. 1, doi: 10.1088/1742-6596/524/1/012186.

[22] N. G. Nygaard, S. T. Steen, L. Poulsen, and J. G. Pedersen, "Modelling cluster wakes and wind farm blockage," in *Journal of Physics: Conference Series*, Sep. 2020, vol. 1618, no. 6, doi: 10.1088/1742-6596/1618/6/062072.

[23] X. Gao, H. Yang, and L. Lu, "Optimization of wind turbine layout position in a wind farm using a newly-developed two-dimensional wake model," *Appl. Energy*, vol. 174, pp. 192–200, Jul. 2016, doi: 10.1016/j.apenergy.2016.04.098.

[24] L. A. Martínez-Tossas, J. Annoni, P. A. Fleming, and M. J. Churchfield, "The aerodynamics of the curled wake: A simplified model in view of flow control," *Wind Energy Sci.*, vol. 4, no. 1, pp. 127–138, Jan. 2019, doi: 10.5194/wes-4-127-2019.

[25] G. C. Larsen, *A simple wake calculation procedure*. 1988.

[26] M. Bastankhah and F. Porté-Agel, "A new analytical model for wind-turbine wakes," *Renew. Energy*, vol. 70, pp. 116–123, 2014, doi: 10.1016/j.renene.2014.01.002.

[27] T. Ishihara and G. W. Qian, "A new Gaussian-based analytical wake model for wind turbines considering ambient turbulence intensities and thrust coefficient effects," *J. Wind Eng. Ind. Aerodyn.*, vol. 177, pp. 275–292, Jun. 2018, doi: 10.1016/j.jweia.2018.04.010.

[28] J. K. Lundquist, K. K. DuVivier, D. Kaffine, and J. M. Tomaszewski, "Costs and consequences of wind turbine wake effects arising from uncoordinated wind energy development," *Nat. Energy*, vol. 4, no. 1, pp. 26–34, Jan. 2019, doi: 10.1038/s41560-018-0281-2.

[29] T. Ahsbahs, N. G. Nygaard, A. Newcombe, and M. Badger, "Wind farm wakes from SAR and doppler radar," *Remote Sens.*, vol. 12, no. 3, Feb. 2020, doi: 10.3390/rs12030462.

[30] B. Canadillo *et al.*, "Offshore wind farm wake recovery: Airborne measurements and its representation in engineering models," *Wind Energy*, vol. 23, pp. 1249–1265, Jun. 2020.

[31] V. Pettas, M. Kretschmer, A. Clifton, and P. W. Cheng, "On the effects of inter-farm interactions at the offshore wind farm Alpha Ventus," *Wind Energy Sci.*, vol. 6, no. 6, pp. 1455–1472, Nov. 2021.

[32] M. P. van deer Loan *et al.*, "An Improved k-ε model applied to a wind turbine wake in atmospheric turbulence," *Wind Energy*, vol. 18, pp. 889–907, Apr. 2015.

[33] I. Ammara, C. Leclerc, and C. Masson, "A viscous three-dimensional differential/actuator-disk method for the aerodynamic analysis of wind farms," *J. Sol. Energy Eng. Trans. ASME*, vol. 124, no. 4, pp. 345–356, Nov. 2002, doi: 10.1115/1.1510870.

[34] N. Troldborg, G. C. Larsen, H. A. Madsen, K. S. Hansen, J. N. Sørensen, and R. Mikkelsen, "Numerical simulations of wake interaction between two wind turbines at various inflow conditions," *Wind Energy*, vol. 14, no. 7, pp. 859–876, Oct. 2011, doi: 10.1002/we.433.

[35] F. Porté-Agel, H. Lu, and Y. T. Wu, "Interaction between large wind farms and the atmospheric boundary layer," in *Procedia IUTAM*, 2014, vol. 10, pp. 307–318, doi: 10.1016/j.piutam.2014.01.026.

[36] P. Fleming, "FLORIS: Flow Redirection and Induction in Steady State," *2018*, Nov. 09, 2021. https://www.nrel.gov/wind/floris.html (accessed Nov. 10, 2021).

[37] NREL, "FLORIS: FLOw Redirection and Induction in Steady State."

https://www.nrel.gov/wind/floris.html (accessed Mar. 13, 2022).

[38] P. Fleming *et al.*, "Overview of FLORIS updates," in *Journal of Physics: Conference Series*, Sep. 2020, vol. 1618, no. 2, doi: 10.1088/1742-6596/1618/2/022028.

[39] P. Fleming *et al.*, "Simulation comparison of wake mitigation control strategies for a two-turbine case," *Wind Energy*, vol. 18, pp. 2135–2143, 2015, Accessed: Mar. 13, 2022. [Online]. Available: https://onlinelibrary.wiley.com/doi/epdf/10.1002/we.1810.

[40] J. King *et al.*, "Control-oriented model for secondary effects of wake steering," *Wind Energy Sci.*, vol. 6, no. 3, pp. 701–714, May 2021, doi: 10.5194/wes-6-701-2021.

[41] P. Fleming *et al.*, "Initial results from a field campaign of wake steering applied at a commercial wind farm – Part 1," *Wind Energy Sci.*, vol. 4, no. 2, pp. 273–285, 2019, doi: 10.5194/wes-4-273-2019.

[42] E. Simley, P. Fleming, and J. King, "Design and analysis of a wake steering controller with wind direction variability," *Wind Energy Sci.*, vol. 5, no. 2, pp. 451–468, Apr. 2020, doi: 10.5194/wes-5-451-2020.

[43] P. Gebraad, J. J. Thomas, A. Ning, P. Fleming, and K. Dykes, "Maximation of the annual energy production of wind power plants by optimizaiton of the layout and yaw-based wake control," *Wind Energy* , vol. 20, pp. 97–117, 2017, Accessed: Mar. 13, 2022. [Online]. Available: https://onlinelibrary.wiley.com/doi/epdf/10.1002/we.1993.

[44] K. S. Hansen *et al.*, "Simulation of wake effects between two wind farms," in *Journal of Physics: Conference Series*, Jun. 2015, vol. 625, no. 1, doi: 10.1088/1742-6596/625/1/012008.

[45] M. A. Prósper, C. Otero-Casal, F. C. Fernández, and G. Miguez-Macho, "Wind power forecasting for a real onshore wind farm on complex terrain

using WRF high resolution simulations," *Renew. Energy*, vol. 135, pp. 674–686, May 2019, doi: 10.1016/j.renene.2018.12.047.

[46] Q. Wang, K. Luo, R. Yuan, S. Zhang, and J. Fan, "Wake and performance interference between adjacent wind farms: Case study of Xinjiang in China by means of mesoscale simulations," *Energy*, vol. 166, pp. 1168–1180, Jan. 2019, doi: 10.1016/j.energy.2018.10.111.

[47] R. M. A. Feroz, A. Javed, A. H. Syed, S. A. A. Kazmi, and E. Uddin, "Wind speed and power forecasting of a utility-scale wind farm with inter-farm wake interference and seasonal variation," *Sustain. Energy Technol. Assessments*, vol. 42, Dec. 2020, doi: 10.1016/j.seta.2020.100882.

[48] S. R. Reddy, "Wind Farm Layout Optimization (WindFLO): An advanced framework for fast wind farm analysis and optimization," *Appl. Energy*, vol. 269, Jul. 2020, doi: 10.1016/j.apenergy.2020.115090.

[49] A. Vasel-Be-Hagh and C. L. Archer, "Wind farm hub height optimization," *Appl. Energy*, vol. 195, pp. 905–921, 2017, doi: 10.1016/j.apenergy.2017.03.089.

[50] J. Feng and W. Z. Shen, "Solving the wind farm layout optimization problem using random search algorithm," *Renew. Energy*, vol. 78, pp. 182–192, Jun. 2015, doi: 10.1016/j.renene.2015.01.005.

[51] X. Wu, W. Hu, Q. Huang, C. Chen, M. Z. Jacobson, and Z. Chen, "Optimizing the layout of onshore wind farms to minimize noise," *Appl. Energy*, vol. 267, Jun. 2020, doi: 10.1016/j.apenergy.2020.114896.

[52] S. Yamani Douzi Sorkhabi, D. A. Romero, J. C. Beck, and C. H. Amon, "Constrained multi-objective wind farm layout optimization: Novel constraint handling approach based on constraint programming," *Renew. Energy*, vol. 126, pp. 341–353, Oct. 2018, doi: 10.1016/j.renene.2018.03.053.

[53]   R. N. King, K. Dykes, P. Graf, and P. E. Hamlington, "Optimization of wind plant layouts using an adjoint approach," *Wind Energy Sci.*, vol. 2, no. 1, pp. 115–131, 2017, doi: 10.5194/wes-2-115-2017.

[54]   E. G. A. Antonini, D. A. Romero, and C. H. Amon, "Continuous adjoint formulation for wind farm layout optimization: A 2D implementation," *Appl. Energy*, vol. 228, pp. 2333–2345, Oct. 2018, doi: 10.1016/j.apenergy.2018.07.076.

[55]   E. G. A. Antonini, D. A. Romero, and C. H. Amon, "Optimal design of wind farms in complex terrains using computational fluid dynamics and adjoint methods," *Appl. Energy*, vol. 261, Mar. 2020, doi: 10.1016/j.apenergy.2019.114426.

[56]   J. Y. J. Kuo, D. A. Romero, J. C. Beck, and C. H. Amon, "Wind farm layout optimization on complex terrains – Integrating a CFD wake model with mixed-integer programming," *Appl. Energy*, vol. 178, pp. 404–414, Sep. 2016, doi: 10.1016/j.apenergy.2016.06.085.

[57]   K. Yang, G. Kwak, K. Cho, and J. Huh, "Wind farm layout optimization for wake effect uniformity," *Energy*, vol. 183, pp. 983–995, Sep. 2019, doi: 10.1016/j.energy.2019.07.019.

[58]   Q. Yang, H. Li, T. Li, and X. Zhou, "Wind farm layout optimization for levelized cost of energy minimization with combined analytical wake model and hybrid optimization strategy," *Energy Convers. Manag.*, vol. 248, Nov. 2021, doi: 10.1016/j.enconman.2021.114778.

[59]   N. Quan and H. M. Kim, "Greedy robust wind farm layout optimization with feasibility guarantee," *Eng. Optim.*, vol. 51, no. 7, pp. 1152–1167, Jul. 2019, doi: 10.1080/0305215X.2018.1509962.

[60]   N. Kirchner-Bossi and F. Porté-Agel, "Realistic wind farm layout optimization through genetic algorithms using a Gaussian wake model," *Energies*, vol. 11, no. 12, Dec. 2018, doi: 10.3390/en11123268.

[61] A. P. J. Stanley and A. Ning, "Coupled wind turbine design and layout optimization with nonhomogeneous wind turbines," *Wind Energy Sci.*, vol. 4, no. 1, pp. 99–114, Jan. 2019, doi: 10.5194/wes-4-99-2019.

[62] "Monte Carlo Simulation." https://www.ibm.com/cloud/learn/monte-carlo-simulation (accessed May 12, 2022).

[63] G. Marmidis, S. Lazarou, and E. Pyrgioti, "Optimal placement of wind turbines in a wind park using Monte Carlo simulation," *Renew. Energy*, vol. 33, no. 7, pp. 1455–1460, Jul. 2008, doi: 10.1016/j.renene.2007.09.004.

[64] A. P. J. Stanley, A. Ning, and K. Dykes, "Optimization of the turbine design in wind farms with multiple hub heights, using analytic gradients and structural constraints," *Wind Energy*, vol. 22, pp. 605–619, 2019, Accessed: May 09, 2022. [Online]. Available: https://onlinelibrary.wiley.com/doi/epdf/10.1002/we.2310.

[65] L. Wang, M. E. Cholette, Y. Zhou, J. Yuan, A. C. C. Tan, and Y. Gu, "Effectiveness of optimized control strategy and different hub height turbines on a real wind farm optimization," *Renew. Energy*, vol. 126, pp. 819–829, Oct. 2018, doi: 10.1016/j.renene.2018.04.004.

[66] S. A. MirHassani and A. Yarahmadi, "Wind farm layout optimization under uncertainty," *Renew. Energy*, vol. 107, pp. 288–297, 2017, doi: 10.1016/j.renene.2017.01.063.

[67] K. Chen, M. X. Song, X. Zhang, and S. F. Wang, "Wind turbine layout optimization with multiple hub height wind turbines using greedy algorithm," *Renew. Energy*, vol. 96, pp. 676–686, Oct. 2016, doi: 10.1016/j.renene.2016.05.018.

[68] Y. Chen, H. Li, K. Jin, and Q. Song, "Wind farm layout optimization using genetic algorithm with different hub height wind turbines," *Energy Convers. Manag.*, vol. 70, pp. 56–65, 2013, doi: 10.1016/j.enconman.2013.02.007.

[69] J. Annoni *et al.*, "Analysis of Control-Oriented Wake Modeling Tools Using Lidar Field Results," *Wind Energy Sci. Discuss.*, vol. 3, no. 2, pp. 1–17, 2018, doi: 10.5194/wes-2018-6.

[70] C. Bay *et al.*, "FLORIS: A Brief Tutorial," Accessed: Nov. 10, 2021. [Online]. Available: https://www.nrel.gov/wind/assets/pdfs/systems-engineering-workshop-2019-floris.pdf.

[71] "FLORIS Wake Modeling Utility." https://floris.readthedocs.io/en/main/ (accessed Nov. 10, 2021).

[72] P. M. O. Gebraad *et al.*, "A data-driven model for wind plant power optimization by yaw control," in *Proceedings of the American Control Conference*, 2014, pp. 3128–3134, doi: 10.1109/ACC.2014.6859118.

[73] M. Abkar and F. Porté-Agel, "Influence of Atmospheric Stability on Wind-Turbine Wakes: A Large-Eddy Simulation Study."

[74] A. Niayifar and F. Porté-Agel, "Analytical modeling of wind farms: A new approach for power prediction," *Energies*, vol. 9, no. 9, pp. 1–13, 2016, doi: 10.3390/en9090741.

[75] R. Stull, *An introduction to boundary-layer meteorology*. Dordrecht,: Kluwer Academic Publishers, 1988.

[76] D. C. Quarton and J. F. Ainslie, "Turbulence in Wind Turbine Wakes," 1990.

[77] A. Jimenez, A. Crespo, and E. Migoya, "Application of a LES Technique to Characterize the Wake Deflection of a Wind Turbine in Yaw," *Wind Energy*, vol. 13, pp. 559–572, 2010.

[78] P. M. O. Gebraad, Teeuvisse F.W., Wingede J.W., Flemin P.A., and Ruben S.D., "Wind plant power optimization through yaw control using a parametric model for wake effects—a CFD simulation study," *Wind Energy*, vol. 16, pp. 95–114, 2016.

[79] G. W. Qian and T. Ishihara, "A new analytical wake model for yawed wind turbines," *Energies*, vol. 11, no. 3, Feb. 2018, doi: 10.3390/en11030665.

[80] J. Bleeg, M. Purcell, R. Ruisi, and E. Traiger, "Wind farm blockage and the consequences of neglecting its impact on energy production," *Energies*, vol. 11, no. 6, Jun. 2018, doi: 10.3390/en11061609.

[81] A. Segalini and J. Å. Dahlberg, "Blockage effects in wind farms," *Wind Energy*, vol. 23, no. 2, pp. 120–128, Feb. 2020, doi: 10.1002/we.2413.

[82] "Nordex N100." https://en.wind-turbine-models.com/turbines/44-nordex-n100-gamma (accessed Feb. 07, 2022).

[83] "Nordex N117," Accessed: Feb. 07, 2022. [Online]. Available: https://en.wind-turbine-models.com/turbines/439-nordex-n117-delta.

[84] F. M. White, *Fluid Mechanics*, 7th ed. New York: McGraw Hill.

[85] Ministry of Energy and Natural Resources of Turkey, "The final meeting of the project for the creation of Turkey wind energy potential atlas and wave energy potential atlas," Ankara, May 2020.

[86] L. Fingersh, M. Hand, and A. Laxson, "Wind Turbine Design Cost and Scaling Model," 2006. [Online]. Available: http://www.osti.gov/bridge.

[87] "JMP." https://www.jmp.com/en_us/software/data-analysis-software.html (accessed Apr. 24, 2022).

[88] "Design of Experiment Scheme." https://asq.org/quality-resources/design-of-experiments (accessed May 26, 2022).

[89] "Pareto Principle." https://www.forbes.com/sites/kevinkruse/2016/03/07/80-20-rule/?sh=6eafe1d73814 (accessed May 22, 2022).

[90] SAS Institute., *Design of experiments guide : JMP 11*. SAS Institute, 2013.

APPENDICES

A. Response Surface Equation for Case-1

$$OEC_1 = 0.99999775 + 0.0013689xU19 + 0.0011009xU18 + 0.0009340xU21$$
$$+ 0.0009128xU23 + 0.0009454xU20 + 0.0009120xU22$$
$$+ 0.0008682xU17 + 0.0007224xU24 + U19(-0.000110xU19)$$
$$+ U19x(0.0000002xU18) + U18x(-0.000054xU18)$$
$$+ U19x(0.000002xU21) + U18x(0.0000002xU21)$$
$$+ U21x(-0.000082xU21) + 0.0000002xU23)$$
$$+ U18x(0.0000002xU23) + U21x(-0.0000007xU23)$$
$$+ U23x(-0.000075xU23) + U19x(0.0000007xU20)$$
$$+ U18x(-0.0000002xU20) + U21x(-0.0000002xU20)$$
$$+ U23x(-0.0000002xU20) + U20x(-0.000082xU20)$$
$$+ U19x(0.0000002xU22) + U18x(0.0000002xU22)$$
$$+ U21x(-0.0000007xU22) + U23x(-0.0000007xU22)$$
$$+ U20x(-0.0000002xU22) + U22x(-0.000075xU22)$$
$$+ U19x(0.0000002xU17) + U18x(0.0000002xU17)$$
$$+ U21x(0.0000002xU17) + U23x(0.0000002xU17)$$
$$+ U20X(-0.0000002xU17) + U22x(0.0000002xU17)$$
$$+ U17x(-0.000040xU17) + U19x(0.0000002xU24)$$
$$+ U18x(0.00000002xU24) + U21x(-0.0000002xU24)$$
$$+ U23x(-0.0000002xU24) + U20x(-0.00000002xU24)$$
$$+ U22x(-0.0000007xU24) + U17x(0.0000002xU24)$$
$$+ U24x(-0.000040xU24)$$

B. Response Surface Equation for Case-2

$$OEC_2 = 8.99978 + 0.00578xU19 - 0.00163xU15 - 0.00319xU21 - 0.00342xU18$$
$$+ 0.00308xU23 + 0.00321xU16 + 0.00327xU20 - 0.00309xU14$$
$$+ U19x(-0.00042xU19) + U19x(0.00002xU15)$$
$$+ U15x(-0.00024xU15) + U19x(U21x0.00001)$$
$$+ U15x(0.00002xU21) + U21x(-0.00051xU21)$$
$$+ U19x(U18x0.00002) + U15x(U18x0.0003) + U21x(0.00002xU18)$$
$$+ U18x(0.00131xU18) + U19x(0.00002xU23)$$
$$+ U15x(0.00023xU23) + U21x(0.0002xU13)$$
$$+ U18x(-0.00047xU23) + U23x(0.00003xU23)$$
$$+ U19x(0.00002xU16) + U15x(0.00003xU16)$$
$$+ U21x(0.00002xU16) + U18x(0.00002xU16)$$
$$+ U23x(0.00271xU16) + U16x(0.00002xU16)$$
$$+ U19x(0.00003xU20) + U15x(0.00002xU20)$$
$$+ U21x(0.00002xU20) + U18x(0.00002xU20)$$
$$+ U23x(0.00002xU20) + U16x(-0.00097xU20)$$
$$+ U19x(0.00002xU14) + U15x(0.00003xU14)$$
$$+ U21x(0.00003xU14) + U18x(0.00002xU14$$
$$+ (U23x(0.00002xU14) + U16x(0.00002xU14)$$
$$+ U20x(0.00017xU14) + U14x(-0.00093xU14)$$

C. Response Surface Equation for Case-3

$$OEC_1 = 0.9999978 + 0.0013689xU44 + 0.0011008xU45 + 0.0009340xU41$$
$$+ 0.0009128xU40 + 0.0009451xU43 + 0.0009129xU42$$
$$+ 0.00086820xU35 + 0.0007224xU34$$
$$+ U44x(-0.0001105xU44) + U44x(0.0000002xU45)$$
$$+ U45x(-0.0000540xU45) + U44x(0.0000002xU41)$$
$$+ U45x(0.0000002xU41) + U41x(-0.0000822xU41)$$
$$+ U44x(0.0000002xU40) + U45x(0.0000002xU40)$$
$$+ U41x(-0.0000007xU40) + U40x(-0.0000752xU40)$$
$$+ U44x(0.0000007xU43) + U45x(-0.0000002xU43)$$
$$+ U40x(-0.0000002xU43) + U43x(-0.0000822xU43)$$
$$+ U44x(0.0000002xU42) + U45x(0.0000002xU42)$$
$$+ U41x(-0.0000066xU42) + U43x(-0.0000002xU42)$$
$$+ U42x(-0.000075xU42) + U44x(0.0000002xU35)$$
$$+ U45x(0.0000002xU35) + U41x(0.0000002xU35)$$
$$+ U40x(0.0000002xU35) + U43x(-0.0000002xU35)$$
$$+ U42x(0.0000002xU35) + U35x(-0.0000399xU35)$$
$$+ U44x(0.0000002xU34) + U45x(0.000000xU34)$$
$$+ U41x(-0.000007xU34) + U40x(-0.0000007xU34)$$
$$+ U43x(-0.0000002xU34) + U42x(-0.0000007xU34)$$
$$+ U35x(0.0000002xU34) + U34x(-0.0000399xU34)$$

D. Response Surface Equation for Case-4

$$OEC_2 = 9.000019 - 0.0054024xU32 - 0.0053779xU33 + 0.0051143xU31$$
$$+ 0.0050998xU39 - 0.0050882xU38 + 0.0050305xU37$$
$$- 0.0049790xU36 - 0.0049779xU46 + U32x(-0.0000550xU32)$$
$$+ U32x(0.0000234xU33) + U33x(0.0000243xU33)$$
$$+ U32x(-0.0000950xU31) + U33x(0.0000271xU31)$$
$$+ U31x(0.0000268xU31) + U32x(0.0000275xU39)$$
$$+ U33x(-0.00000950xU39) + U31x(0.0000296xU39)$$
$$+ U39x(0.0000131xU39) + U32x(0.0000294xU38)$$
$$+ U33x(0.0000269xU38) + U31x(-0.0000500xU38)$$
$$+ U39x(0.0000244xU38) + U38x(0.0000241xU38)$$
$$+ U32x(0.0000241xU37) + U33x(0.0000216xU37)$$
$$+ U31x(0.0000247xU37) + U39x(-0.00000500xU37)$$
$$+ U38x(0.0000256xU37) + U37x(0.0000265xU37)$$
$$+ U32x(0.0000209xU36) + U33x(0.0000209xU36)$$
$$+ U31x(0.0000243xU36) + U39x(0.0000209xU36)$$
$$+ U38x(0.00002187xU36) + U37x(-0.0000100xU36)$$
$$+ U36x(0.0000215xU36) + U32x(0.0000215xU46)$$
$$+ U33x(0.0000262xU46) + U31x(0.0000238xU46)$$
$$+ U39x(0.0000262xU46) + U38x(0.0000215xU46)$$
$$+ U37x(0.0000134xU36) + U36x(0.0001338xU46)$$
$$+ U46x(0.00000100xU46)$$

114